

**Quantifying Strength Size Effects in Polycrystalline Silicon and Aluminum with  
On-chip Test Platforms**

Submitted in partial fulfillment of the requirements for

the degree of

Doctor of Philosophy

in

Mechanical Engineering

Mohamed E. Saleh

B. S. Aeronautical Engineering, Tripoli University

M. S. Mechanical Engineering, Carnegie Mellon University

Carnegie Mellon University  
Pittsburgh, PA

May, 2015

## ACKNOWLEDGMENTS

I would truly and sincerely like to express my deepest gratitude and appreciation to all those who helped me on my journey to receiving my PhD.

Firstly, I would like to thank my PhD advisors, Prof. Maarten de Boer and Prof. Jack Beuth, for giving me the opportunity to learn from them as well as for their guidance and support during my PhD study at CMU. I cannot express enough how much I appreciated their help and their insightful comments that helped me to increase my knowledge and sharpen my skills.

For serving as my thesis committee and for all of their advice, I'd like to thank Prof. Maarten de Boer (Chair), Prof. Jack Beuth, Prof. Steve Collins and Prof. Yoosuf Picard

For all of their help and for teaching me how to use the EBSD technique, I'd like to thank Prof. Yoosuf Picard and Prof. Elena Miranda. Likewise, I want to express my gratitude to Thomas Nuhfer and Adam Wise for their help with SEM.

I am thankful to NSF for supporting this project and to Sandia National Labs for fabricating my test structures.

I would like to thank Chris Hertz for his help with degree requirements, Michael Scampone for processing my conference reimbursements and Melissa Hyzy for facilitating and setting up ANSYS on my personal computer.

This work would not have been easy without the support from my friends, so I am eternally grateful to Sidharth Hazra for his help during the early stages of my PhD and Vitali Brand, Emrecan Soylemez, Ryan Pocratsky, Sameer Shroff, Ramesh Shrestha, Changho Oh, Prince Singh and Kuo-Kang Hung for all of their help and friendship.

I am forever thankful to my wife, Fautma Eshnuk, for all of her support and help throughout my years of study which helped me to succeed on my journey and achieve my goals. And last but not least, I am thankful to my two year old son who distracted me from the stress of my work and provided me with many laughs!

# Abstract

Mechanical strength of components increases as their size decreases. Optimum design of reliable systems at the micro- and nanoscales will account for such size-dependent strength. However, the dependencies of strength on size in brittle ceramic and ductile metal thin films are not well known because of limited data. Therefore, in this thesis, high throughput platforms were designed, fabricated and tested. The strength size effect for polycrystalline silicon (polysilicon) and polycrystalline aluminum thin films has been investigated by on-chip testing techniques.

Polysilicon structures over a size range of 100 increase in characteristic strength from 2.7 GPa to 4.2 GPa. A Weibull function alone was insufficient to predict the strength size effect for polysilicon. After taking into account the non-uniform stress distribution in the smallest specimens, both the characteristic strength and the full strength probability distribution function was well predicted. Also, a Monte Carlo technique was developed to predict strength size effects and to assess the minimum number of tests required for accurate characterization of strength distribution.

Aluminum thin film structures over a size range of 6.5 increase in average yield strength from 140 MPa to 300 MPa. Unlike macroscale specimens, these samples also exhibit significant scatter in strength. The ratio of the standard deviation in yield strength to the average yield strength is 0.06 for 1  $\mu\text{m}$  thick samples, and more than doubles to 0.13 for 0.6  $\mu\text{m}$  thick samples.

High throughput test platforms provide an important method to assess strength and strength distribution data at the micro- and nanoscales.

# Table of Contents

ACKNOWLEDGMENTS .....	II
Abstract.....	IV
List of Tables .....	IX
List of Figures.....	X
Chapter I: Introduction and Overview.....	1
1.1 Motivation .....	1
1.2 Deformation and Failure Mechanisms .....	2
1.2-1 Polysilicon Fracture Mechanics .....	2
1.2-2 Aluminum Deformation Mechanisms .....	5
1.3 Test Platforms .....	8
1.3-1 Test Platforms with Off-chip Actuators .....	9
1.3-2 Test Platforms with On-chip Actuators.....	13
1. 4 Test Set-up .....	16
1.4-1 Probe Station .....	16
1.4-2 Scanning Electron Microscopy .....	17
1.5 Contributions.....	17
1.6 Dissertation Organization.....	19

1.7 Journal Papers .....	20
1.8 Conference Presentations .....	21
Chapter 2: Polysilicon strength Size effect .....	23
2.1 Introduction .....	23
2.2 Theoretical Background .....	27
2.3- Experimental Approach .....	32
2.3-1 Test Platform and Tensile Bar Designs .....	32
2.3-2 Test Structure Analysis .....	35
2.4 Results and Discussion.....	40
2.4-1 Strength distribution .....	41
2.4-3 Analysis 2 -- Strength prediction based on Specimens 1 and 2 .....	44
2.5 Analysis of Specimen 5 .....	51
2.6-Summary and Conclusions .....	52
Chapter 3: In-situ platform for isothermal testing of thin film mechanical properties using thermal actuators.....	53
3.1 Introduction .....	54
3.2 Test platform design considerations .....	56
3.2-1 Thermal actuator.....	58
3.2-2 Load cell .....	60

3.2-3 Thermal resistor and heat sink configuration .....	62
3.2-4 Pre-inserted microgrippers .....	65
3.3 Experimental .....	66
3.3-1 Thin film tensile specimens tested .....	66
3.3-2 Mechanical Testing .....	67
3.3-3 Data Analysis.....	68
3.3-4 Transmission electron microscopy .....	69
3.4 Results and Discussion.....	70
3.5-Summary and conclusions .....	78
Chapter 4: Statistical Investigation of Size Effect of Yield Stress and Elongation for Free-standing Polycrystalline Al-0.5% Cu Thin Film .....	80
4.1 Introduction .....	80
4.2 Statistical Strength and Elongation Results .....	82
4.3 Summary .....	91
Chapter 5: Conclusions and Future Work .....	92
5.1 Summary and Conclusions.....	92
5.2 Future Work .....	93
Appendix A: Hazra's test platform [54].....	95
Appendix B : Displacement results .....	98

Appendix C: Weibull 2 parameter prediction .....	100
Appendix D: Specimen 5 experimental Results .....	102
Appendix E:Elastically connected design for the AI test platform .....	103
Appendix F: Finite element analysis of temperature of the aluminum test platform.....	105
Appendix-G: Uncertainty analysis for stress $\sigma$ , strain $\epsilon$ and modulus of elasticity $E$ ....	108
Appendix H: Stress vs strain curves for different specimens.....	115
Appendix I: Preliminary Creep Experiments .....	118
Appendix J: Monte Carlo Simulation.....	119
J.1 Model Derivation for Uniform Specimens.....	120
J.2 Model Derivation for DEN Specimens .....	129
J.3 Specimens Number Effect and the Convergence to Unique Curve .....	132
Appendix H Analytical Solution for Off Axis Loading of Tensile Bar .....	136
References .....	141

## List of Tables

Table 2.1 Summary of some of the work in polysilicon .....	25
Table 2.2: Analysis 1 - using only Specimen 1 to make scaling predictions with W3P $\sigma_u = 2.18$ GPa, $\sigma_o = 3.4$ GPa $\cdot \mu\text{m}^2/3.05$ and $m = 3.05$ .....	44
Table 2.3 Analysis 2 - using Specimens 1 and 2 to make scaling predictions $\sigma_u =$ 1.95 GPa, $\sigma_o = 2.47$ GPa. $\mu\text{m}^2/4.8$ and $m = 4.83$ .....	50
Table 3.1 Test Platform Design Parameters .....	58
Table 3.2 Summary of test results .....	71
Table 4.1: Summary of Specimens and Results .....	84
Table B1 W2P parameters for each specimen.....	100
Table B2 W3P parameters for each specimen.....	100
Table G1. Values of parameters used to estimate uncertainty in stress .....	109
Table B2. The contribution of each parameter to the stress variance .....	110

## List of Figures

Fig 1.1 Fractographic observations to identify fracture origin (from Boyce et al., 2010), The flaw originates at the location indicated by the arrow. ....	5
Fig 1.2 Grain thinning mechanism. (Lee et al. 2002).....	7
Fig 1.3 Image of the test system from Read et al, 1993 .....	9
Fig 1.4 Electrostatic gripping test technique, Tsuchiya et al., 1998.....	10
Fig. 1.5 Tensile tester by Greek et al. 1999 .....	11
Fig 1.6 Test system by Sharpe et al 1997 .....	11
Fig 1.7 Slack chain test method by Boyce 2009 .....	12
Fig 1.8 The membrane deflection experiment (Espinosa et al. 2003).....	13
Fig 1.9 Test system for nano scale materials (Zhu et al 2006).....	15
Fig 1.10 Schematic of test technique by Gravier et al. 2009 .....	16
Fig 1.11 Optical microscope used in our mechanical test (Hazra 2010).....	17
Fig. 2.1 Optical image of test platform. The salient features including the thermal actuator, shuttle, crosshead, displacement gage, and anchor pad are indicated. ....	33
Fig. 2.2 Optical images of Specimens 1–4. (1) $70\ \mu\text{m} \times 2\ \mu\text{m}$ , (2) $7\ \mu\text{m} \times 2\ \mu\text{m}$ , (3) 4/4 DEN, and (4) 4/1 DEN (DEN = double-edge notch, Specimens 3 and 4 are $10\ \mu\text{m}$ wide, have $4\ \mu\text{m}$ deep notches and a radius of curvature designated by the number after the slash). .....	34

Fig. 2.3. Determination of residual stress from the force displacement plot. There is a single starting point of residual stress at which the  $\Delta d_2$  arrow begins such that the vertical extension of the arrow end intersects the tensile bar load line/residual stress intersection. ....37

Fig. 2.4. Example measurement of test sample fracture in Specimen 2, and of the residual displacement  $\Delta d_2$  due to the elastic expansion of thermal actuator legs after fracture. ....38

Fig.2.5. SEM image of a fractured Specimen 4 (4/1 DEN). ....40

Fig. 2.6. Probability versus strength data for Specimens 1–4. ....41

Fig. 2.7. Determination of the three Weibull parameters from Specimen 1 using the maximum likelihood method. The solid red line indicates the MLE fit. The dashed black lines represent the 95% confidence interval. ....43

Fig. 2.8. Prediction (solid curves) of the strength distribution compared to the experimental results based on Analysis Method 1. Low values of Q result for Specimens 3 and 4. ....43

Fig. 2.9. Determination of Weibull parameters based on Specimens 1 and 2. ....46

Fig. 2.10. Fitting Specimens 1 and 2 then predicting Specimen 3 and 4 probability distribution functions (solid lines) without accounting for change in threshold strength. ....47

Fig. 2.11. Schematic view of local stress distribution in uniform and notched samples.....	48
Fig. 2.12. Curve fitting of all strength data with Analysis Method 2 assuming a single value for m from Specimens 1 and 2, and bycalculating values of ru due to the stress gradient in Specimens 3and 4. ....	50
Fig 3.1 SEM image of the test platform.....	57
Fig. 3.2 (a) Calculated TA force-displacement curves (solid lines) with elastic and elastic-plastic load lines (dashed) (b) calculated temperature of legs and central shuttle versus TA voltage.....	60
Fig. 3.3 Load cell including displacement and force gages.....	61
Fig. 3.4 Thermal conductivity versus temperature for different materials .....	63
Fig. 3.5 Simplified thermal circuit of thermal resistance, heat sink, tensile specimen configuration. $R_{TR}$ - thermal resistor resistance, $R_{HS}$ - heat sink resistance, $R_{TS}$ - tensile specimen resistance, $R_{AMB}$ - lumped resistance thru the ambient. ...	63
Fig. 3.6 The microgrippers (a) an SEM tilt view shows the load -carrying grippers and out-of-plane constraint grippers (b) gripper schematic cross-sections .....	66
Fig. 3.7 70 $\mu\text{m}$ long tensile specimen .....	67
Fig. 3.8 The inverse of stiffness vs. specimen length for different tensile bars .....	71

Fig. 3.9 Stress versus strain curves up to fracture (dashed lines indicate instability-induced displacements). Data are offset by a strain of 0.1% to make each curve distinguishable .....72

Fig. 3.10 Out-of-plane deflection versus TA voltage for  $LTS = 70 \mu m$  sample....74

Fig. 3.11 TEM composite image shows the regions of study.....76

Fig. 3.12 TEM images for  $LTS=50 \mu m$ ,  $tTS=0.63 \mu m$ . (a) Region 1, (b) Region 2 and.....77

Fig. 3.13 TEM images for  $LTS=50 \mu m$ ,  $tTS=1.03 \mu m$ . (a) Region 1, (b) Region 2 and.....77

Fig 4.1 Stress versus strain curves up to fracture for some of the thin films, (a)  $t = 0.63 \mu m$ , (b)  $t=1.03 \mu m$ . Data are offset to make each curve distinguishable.....83

Fig. 4.2 Yield stress ( $\sigma_y$ ) size effect in (a) thickness  $t$  and (b) length  $L$ . The data are slightly offset to distinguish the different thicknesses and lengths. (filled markers are  $t=0.63 \mu m$  specimens while unfilled markers indicate  $t=1.03 \mu m$ ) ....85

Fig 4.3 the ratio of standard deviation to average of yield stress vs. thickness.....86

Fig. 4.4 Elongation size effect in (a) thickness (b) length. The data are slightly offset to distinguish the different lengths or thickness. (filled markers are  $t=0.63 \mu m$  specimens while unfilled markers indicate  $t=1.03 \mu m$ ) .....87

Fig. 4.5 Two interrupted experiments where specimens show strain softening (a) 0.63  $\mu\text{m}$  thickness (b) 1.03  $\mu\text{m}$  specimen. The specimens show necking which correlates with the strain softening. ....90

Fig. 4.6 Fracture region for some specimens ( $t = 0.63 \mu\text{m}$ ) that show strain hardening till fracture.....90

Fig A1 Hazra’s design (a) schematic view (b) SEM of fabricated structure (Hazra 2010) .....95

Fig. A2 The axial displacement recorded at both displacement gauges for the same test structure (tests were performed without breaking tensile bar) Note that for the same voltage, the displacement is larger for the right gauge than the left gage.....96

Fig. A3 The cross-head displacement is monitored to quantify misalignment .....97

Fig A4 Lateral displacement and rotation of cross-head during loading .....97

Fig. C1. (a) Best W2P fits to each specimen. (b) Best W3P fits to each specimen by Maximum likelihood method.....100

Fig. C2. W2P Strength prediction of Specimens 2-4 using Specimen 1 data. ....101

Fig. D1 Strength distribution for all specimens .....102

Fig. E1 SEM image of the elastically connected design .....103

Fig. E2 Stress vs. strain curve for one of the specimens from the elastically connected design. Our measurement start from around 100 MPa due to large residual stress .....103

Fig. E3 Out of plane displacement for the specimen and thermal resistor at (a) 0V compared to ANSYS results (b) at different voltages .....	104
Fig. E4 3D-ANSYS multi-physics model to the test platform .....	104
Fig. F5 Test platform modeled in ANSYS .....	106
Fig. G1 Contributions of (i) load cell width, deflection and Young's modulus and (ii) tensile specimen width and thickness to the total uncertainty in stress .....	111
Fig G2 Contributions to total error in stress as function of load cell deflection ...	112
Fig G3 Uncertainty in Young's modulus as function of strain percentage .....	114
Fig H-1 Stress –strain curves for $t = 0.63 \mu m$ specimens.....	115
Fig H-2 Stress –strain curves for $t = 1.03 \mu m$ specimens.....	116
Fig I1 Creep experiment at $157^\circ C$ .....	118
Fig. J.1 The construction of RVEs (a) Uniform tensile bar loading (b) Representative volume elements (RVEs) (c) The choice of the length of RVEs ( $li$ ) .....	121
Fig J.2 Crack orientation in RVE.....	123
Fig J.3 Monte Carlo Approach.....	126
Fig. J.4 Fitting specimen 1 experimental results with 1000 data points from MC simulation.....	128
Fig J.5 Predicting Specimens 2 strength distribution by 1000 data points from MC simulation.....	128

Fig. J.6 DEN specimens (a) RVE (b) LFM modeling to the problem.....129

Fig J.6 strength distribution prediction for DEN specimens. (a) Specimen 3 (b) Specimens 4 (c) Specimen 5. The prediction is based on 1000 data points from MC .....131

Fig J.7 Monte Carlo simulation of hypothetical specimens with length of  $20\mu m$  (a) 10 virtual specimens (b) 30 virtual specimen (c) 350 virtual specimen. ....134

Fig. H1 Tensile bar deflection at different specified axial displacement .....137

Fig. H2 Bending moment at  $d=0.001\ \mu m$  .....138

Fig. H3 Bending moment at  $d=1\ \mu m$  .....138

Fig. H4 deflection and moment diagram at  $P=0.1\ mN$  for  $70\ \mu m$  TB .....140

# Chapter I: Introduction and Overview

## 1.1 Motivation

Micro- and nanoelectromechanical systems (MEMS/NEMS) have been implemented in many products that are used in our daily lives such as cars, phones and drug delivery units [1], [2]. The demand for smaller, smarter and more efficient products has driven the design, production and commercialization of many MEMS such as accelerometers [3], gyroscopes [4], microphones [5], and display devices [6]. New engineering fields such as micro- and nanorobotics have emerged where a significant effort is directed towards designing components in the order of microns or even nanometers [7]. The trend of making increasingly smaller products is expected to continue.

One of the most important mechanical properties is strength. MEMS structures are made at different sizes, spanning from a few microns to thousands of microns. Their strength has a strong dependence on size because smaller structures tend to have fewer flaws. Therefore, it is important to predict how strength changes with size for reliable and robust design of MEMS structures. In this work, the size effect in strength for two different materials, polysilicon and aluminum, is investigated.

Polysilicon is the most commonly used material in MEMS. Its widespread use derives from its excellent mechanical properties (low residual stress, low stress gradient, high and consistent Young's modulus [8], [9] and from its compatibility with integrated circuit microfabrication techniques [10]. However, polysilicon can be considered to be a technical ceramic and as such is a brittle material. Subjecting a ceramic material to tension is antithetical to structural engineers. Therefore, quantifying and understanding the high strength of polysilicon is important. The distribution of strength for a given polysilicon specimen has received much attention [11]–[19].

By testing a large number of samples, it recently has become clear that a lower bound value of strength for polysilicon processed by thin film techniques is ~2 GPa, [18], [19], as high as the strongest steels. However, the dependence of strength on size is not yet well understood.

Metal microscale components often consist of at most a few grains of size  $d$  through the thickness  $t$ . Although in metals small grains tend to increase strength due to the Hall-Petch effect, a large  $d/t$  ratio can reduce strength because dislocations that annihilate at a free surface cannot form pileups [20]. This can also reduce ductility due to the influence of a single weak grain [21]. Therefore, it also becomes imperative to test and understand the mechanical behavior of small metal structures for successful design of micro- and nanodevices.

Aluminum thin films exhibit higher yield stress than macroscale aluminum structures. However this comes at the expense of reduced elongation. Due to its low strength, microscale aluminum applications are limited to components that bear small loads [6]. To fully utilize aluminum in reliable MEMS products, quantification of its yield strength and ductility and their variabilities at small sizes is needed.

## **1.2 Deformation and Failure Mechanisms**

### **1.2-1 Polysilicon Fracture Mechanics**

The deformation and fracture behavior of brittle materials differs from that of ductile materials. Polysilicon tensile specimens exhibit linear elastic behavior up to the point of fracture. As just stated, it does fracture at relatively large stresses [17], [19], [22]. Usually, micro-cracks in the form of surface roughness or grain boundaries are present in the brittle material and the structure

fails when the stress intensity factor  $K$  of one of these micro-cracks reaches a critical value which is the fracture toughness  $K_{Ic}$  of the material.

The dispersion in strength is believed to be due to the distribution of processing flaws. The largest flaw in a given structure is not necessarily the same as the largest flaw in another structure of the same nominal size and shape. Due to the strength dispersion in brittle materials, mathematical techniques have been used to study the strength distribution. Weibull [23], [24] developed an equation from the weakest link theory and it has been extensively used to describe the strength distribution of brittle materials. Equation (1.1) shows Weibull three parameter function where  $P$  is the probability of a given specimen,  $\sigma_u$  is the threshold (or lower bound) strength,  $m$  is the Weibull exponent and  $\sigma_\theta$  is scale parameter.

$$P = 1 - \exp\left(-\left(\frac{\sigma - \sigma_u}{\sigma_\theta}\right)^m\right) \quad (1.1)$$

With the Weibull function, we need only to specify three of the material's parameters ( $\sigma_u$ ,  $\sigma_\theta$  and  $m$ ) to fully describe the strength distribution. First, the strength data is sorted in ascending order and the probability of the  $i^{\text{th}}$  specimen from a total of  $n$  specimens can be estimated using the rank equation

$$P = \frac{i - 0.5}{N} \quad (1.2)$$

Then by taking the natural log of equation (1.1) twice, we will get the equation

$$\ln\left(\ln\left(\frac{1}{1-P}\right)\right) = m \ln(\sigma - \sigma_u) - m \ln(\sigma_\theta) \quad , \quad (1.3)$$

which is linear in the form  $y = mx + c$ , where  $y \equiv \ln\left(\ln\left(\frac{1}{1-p}\right)\right)$  and  $x \equiv \ln(\sigma - \sigma_u)$ . The materials constants are estimated by plotting  $\ln\left(\ln\left(\frac{1}{1-p}\right)\right)$  against  $\ln(\sigma - \sigma_u)$ . More details about the derivation and applications of Weibull equation will be provided in Chapter II.

Another important aspect of brittle fracture is the identification of the source of the fracture and this is usually done by utilizing fractography observations. In brittle materials, features such as mirror, mist and hackle zones that are used to identify fracture origin [16]–[18]. The crack starts to propagate and expand smoothly, thus, the mirror region is obtained. The mirror region is perpendicular to the maximum stress direction. When the crack reaches to a critical size, it transforms to mist and hackle region which is much rougher.

Boyce and colleagues [17], [18] have studied the fracture of polysilicon tensile bars with length of 20  $\mu\text{m}$ , width of 2  $\mu\text{m}$  and thickness of 2.25  $\mu\text{m}$ . The samples studied were fabricated in the SUMMiT V<sup>TM</sup> process [25], as were the samples studied in this thesis. More than 300 fracture surfaces were imaged in the scanning electron microscope (SEM). They were able to identify the fracture origin of around 245 specimens. The grain size is large relative to the size of the fractured surface and flaw size has complicated the analysis, however, hackle lines helped elucidate fracture origin. These hackle lines appear to emanate away from the origin of failure as shown in Fig. 1.1. Boyce found that the fracture originated from the sidewall with preference for the bottom corners. No failures initiated in the middle of the bottom or the top surface, nor were any failures initiated within the interior of the specimen [19]. Thus the strength controlling flaws were limited to the sidewalls.

Atomic Force Microscopy (AFM) was performed to investigate the nature of the flaws on the sidewall area [19]. A narrow deep V shape grain boundaries grooves, which are most likely

generated by preferential etching of sidewall grain boundaries, were determined as the most probable source for failure to initiate.

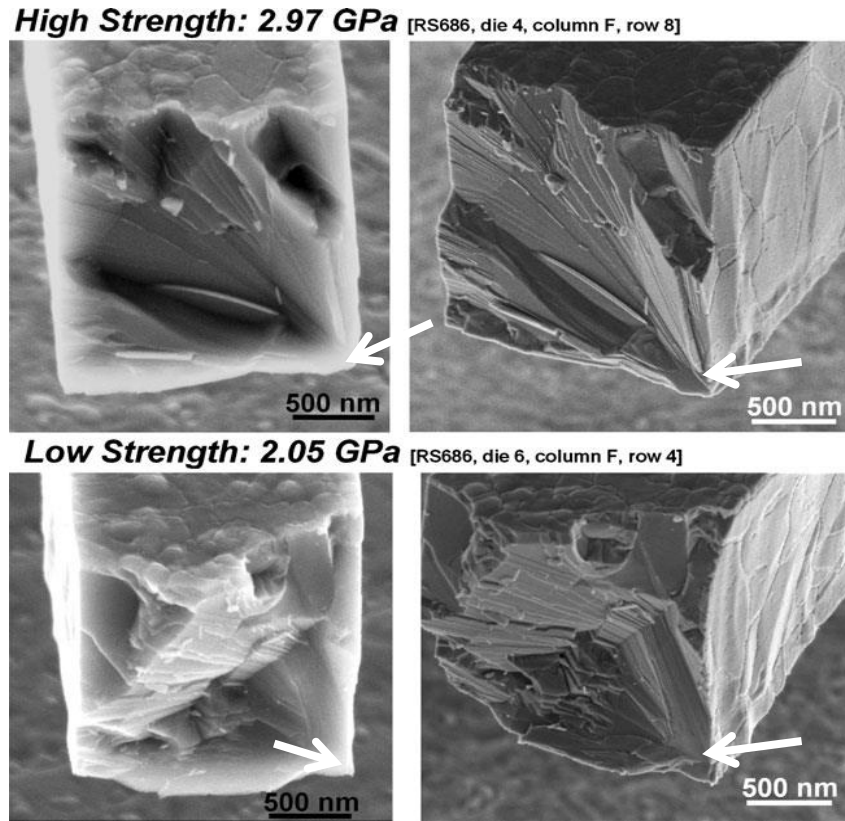


Fig 1.1 Fractographic observations to identify fracture origin (from Boyce et al., 2010), The flaw originates at the location indicated by the arrow.

## 1.2-2 Aluminum Deformation Mechanisms

Aluminum has a simple face centered cubic (FCC) structure. There are many mechanisms for the deformation and fracture of ductile FCC metals. However, some of these are not likely to be applicable to aluminum. For instance, aluminum has large stacking fault energy ( $250 \text{ MJ/m}^2$  [26]), thus, twinning and nucleation and forming of partial dislocations [27]–[29] are unlikely deformation mechanisms. These are therefore neglected in the following sections. Rather, the

possible deformation mechanisms for aluminum are based on dislocation mechanics such as dislocation nucleation, glide, multiplication and pileup.

### **1.2-2-1 Dislocations in metals**

Dislocations are line defects always present in a metal, though after annealing their density is as low as  $10^8/\text{cm}^2$ . When subject to shear stress, dislocations become mobile, and accommodate plastic strain. However, they can be blocked by each other or by hard particles. If sufficient stress is applied, they will multiply by the Frank-Read mechanism [30]. A grain boundary is the interfacial region between two crystalline grains of different orientations. Dislocations that pile up at the grain boundaries cause a large stress concentration. This may lead to nucleation and emission of dislocations at adjacent grains at relatively low applied stress [31].

### **1.2-2-2 Dislocation Pile-up (Hall-Petch Effect)**

Hall [32] and Petch [33] have demonstrated that the grain size play a role on the strength of materials. They have developed an equation that describes the change in strength with the change in grain size. Their model is based on dislocation pile-up at the boundaries. The change in yield stress with respect to grain boundaries can be expressed as

$$\sigma_y = \sigma_o + \frac{k}{\sqrt{d}} \quad (1.4)$$

where  $\sigma_y$  is the yield stress,  $\sigma_o$  and  $k$ : are constants and  $d$  is the grain size.

Venkatraman et al [34] have used a similar formula to account for the change in yield stress due to thickness and grain size. Their formula is based on experimental observations of the yield stress of aluminum thin film on silicon wafer. Their formula can be expressed as

$$\sigma_y = \frac{m_{thick}}{t} + \frac{m_{HP}}{\sqrt{d}} \quad (1.5)$$

where  $m_{thick}$  and  $m_{HP}$  are constants, and  $t$  is the thin film thickness.

### 1.2-2-3 Grain Thinning

Lee et al. [20] studied deformation mechanisms in thin film aluminum by transmission electron microscopy (TEM). They observed grain thinning due to the movement of dislocations from the grain interior to the grain boundary. In this mechanism, the dislocations move from the interior of the grain and some annihilate at the surface while the rest are trapped at grain boundaries. The loss of dislocations to the free surface leads to softening of the interior of grain and hardening of grain boundaries. Thus, plastic deformation becomes concentrated in the grain center and local thinning occurs. Fig 1.2 shows the suggested deformation mechanism. In this picture, it is assumed that the native oxide is thin and does not play an important role in blocking dislocations, in contrast to ref. [34].

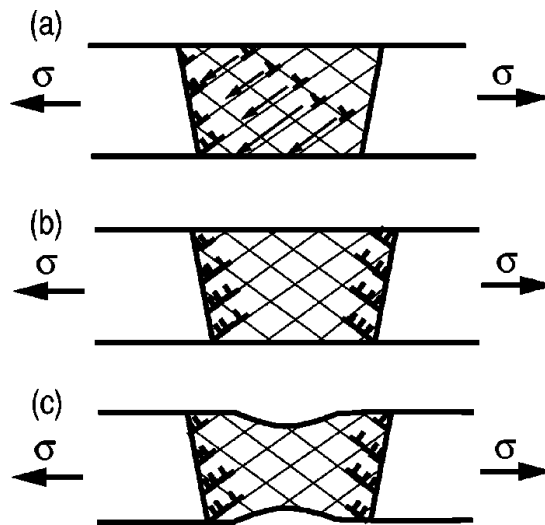


Fig 1.2 Grain thinning mechanism. (Lee et al. 2002)

### **1.2-2-4 Dislocation Starvation**

The motion of dislocations is usually followed by dislocation multiplication. However, according to the dislocation starvation model by Greer and Nix [35], [36], dislocation multiplication cannot happen in small volume structures because the dislocations have a higher probability of annihilating at nearby free surfaces than the probability for dislocation multiplication or dislocation pinning by other dislocations. Greer et al. [35] suggested that the dislocation needs a minimum travel distance (breeding distance)  $\delta$  to multiply. Therefore, if the structure has a dimension less than the breeding distance that would imply that dislocation multiplication is inhibited and dislocations leave before they multiply. Eventually the structure becomes dislocation free and the plastic deformation has to be accommodated by the nucleation and motion of newly generated dislocations.

### **1.3 Test Platforms**

Quantifying the mechanical behavior of micro and nanodevices require the successful design of a test platform that can reliably measure the required property. Many test approaches have been developed to test thin film mechanical properties. In this section we discuss some of these works.

Numerous test techniques have been developed to test the mechanical properties of microscale components. These can be divided into techniques where a non-uniform or a uniform stress field is applied on the specimen. Non-uniform stress techniques such as nanoindentation [37], bulge test [38], torsion [39] and bending [40] induce non-uniform stress states. They are complex in nature and require a detailed analysis which may include the consideration of geometrically necessary dislocations [41]. A uniform stress is simpler and can provide valuable information about the mechanisms that are responsible for plastic deformation. Some of these techniques are

micropillar compression [42], the slack chain test [18] and the membrane deflection experiment [43]. In the above mentioned test techniques, an external or off-chip actuation method is used to apply stress on the specimens. This can be a source of error if the specimen and the load source are not well aligned. Therefore, some investigators prefer on-chip actuation utilizing chevron-shaped thermal actuators (TAs) [44], [45]. In this review, we will focus on detailing some of the uniform stress techniques. The uniform stress test techniques can be divided into two groups: (i) test techniques where an external actuator is used to apply load (off chip actuation) and (ii) test techniques where the actuator is fabricated with the test specimen (on chip actuation).

### 1.3-1 Test Platforms with Off-chip Actuators

One of the earliest test techniques was developed by Read et al. [46]. Their test platform consists of a tensile specimen connected to a fixed platen on one side and to sliding platens from the other side. The sliding platen is connected to a series of load springs. The specimens are made of a Ti/Al/Ti stack with thicknesses of 0.1, 1.98, and 0.1  $\mu\text{m}$  respectively. Four parallel specimens of 250  $\mu\text{m}$  width and 1000  $\mu\text{m}$  length were tested. Failure strength of 200 MPa and elongation only up to 2% was observed in their work. The high strength values and low ductility was completely different than macro scale observations of 20 MPa strength and up to 50% elongation. Fig. 1.3 shows a schematic view of the test system.

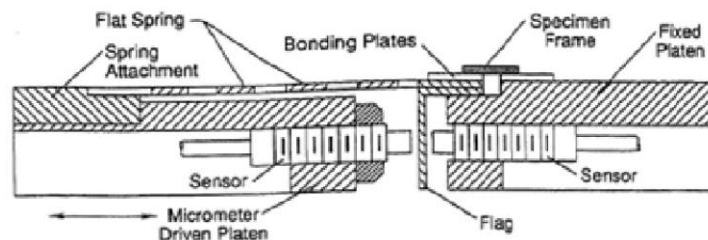


Fig 1.3 Image of the test system from Read et al, 1993

Tsuchiya et al. [11] developed a test system that was implemented in the scanning electron microscope. The test system, as shown in Fig 1.4, consisted of polysilicon specimens of 2  $\mu\text{m}$  thickness that are fixed to a substrate on one side and connected to a free standing large plate on the other side. During loading, the free standing plate is gripped by a probe using electrostatic force. Tsuchiya et al. [11] experimented on 6 different samples with lengths of 30, 100 and 300  $\mu\text{m}$  and widths of 2 and 5  $\mu\text{m}$ . About 17 specimens have been tested from each type. The mean strength increased from 2 GPa for the 300  $\mu\text{m}$  length scale sample to 2.7 GPa for the 30  $\mu\text{m}$  sample. The sample width had no effect on strength indicating that the specimens failed due to edge flaws. A two parameter Weibull analysis (assuming  $\sigma_{\theta} = 0$ ) performed on all the specimens yielded a Weibull modulus ranging between  $m=5.3$  to  $m=6.9$ .

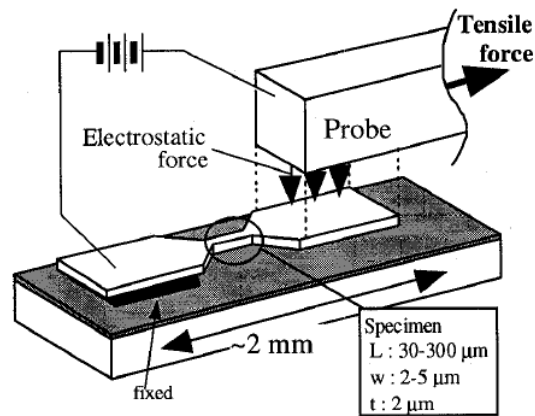


Fig 1.4 Electrostatic gripping test technique, Tsuchiya et al., 1998

Greek et al. [12], as shown in Fig 1.5, developed a tensile testing technique with polycrystalline silicon specimen attached to the substrate by a base plate from one end and to a ring from the other end. A cylindrical probe is inserted into the ring and pulled during testing. The diameter of the ring is chosen such that the inner rim of the ring interacts with the cylindrical probe to align

the force along the tensile specimen's longitudinal axis. The test system was used to measure Young's modulus and fracture strength of polysilicon.

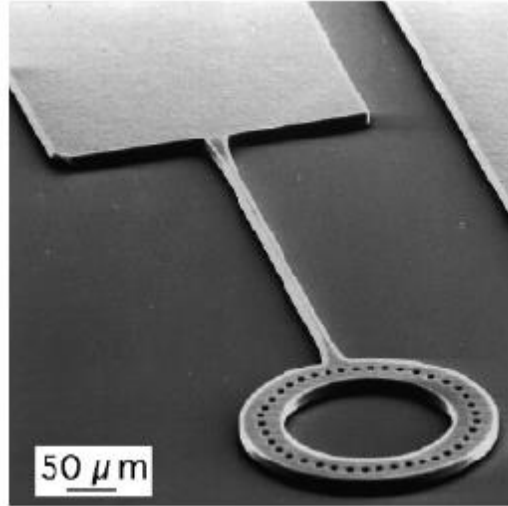


Fig. 1.5 Tensile tester by Greek et al. 1999

Sharpe and colleagues [14], [47] developed tensile tests where both the axial and lateral strains were measured by laser interferometry using markers deposited on the surface of the specimen. They used this technique to measure Young's modulus, strength and Poisson's ratio of polysilicon specimens with thicknesses of  $3.5\ \mu\text{m}$  and widths of  $600\ \mu\text{m}$ . The tensile bars were made from five different production runs from the MUMPs process. The Young's modulus, strength and Poisson's ratio were about 169 GPa, 1.2 MPa and 0.22 respectively. Fig 1.6 shows a schematic view of the test system and the measurement approach.

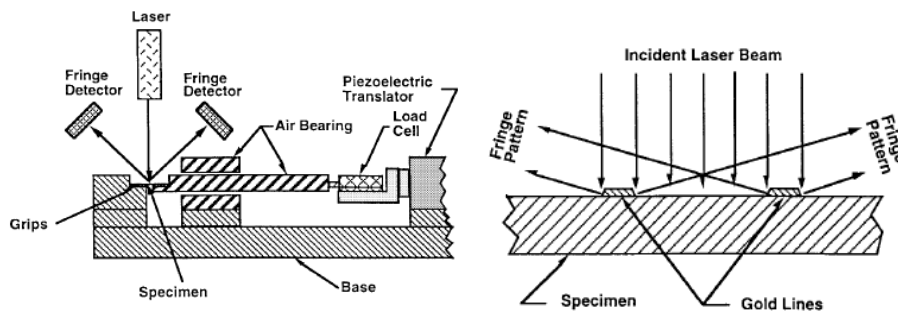


Fig 1.6 Test system by Sharpe et al 1997

Boyce [18] developed an elegant and efficient testing method that enabled him to test over 1000 polysilicon tensile bars within 16 hours. The “slack-chain” testing technique [18] is an improvement over an earlier testing method called “pull tab” [17]. Force is applied to the free end of the chain by using a cylindrical probe and the force is transmitted to only the tensile bar that is the closest to the applied force. The tensile bar fractures upon applying enough force and the force is then transmitted to the next one. Boyce used this method to show that the Weibull three-parameter function better describes the polysilicon strength distribution than the Weibull two-parameter function. Fig 1.7 shows the test structure and schematic view of how this test technique works. One drawback in this method is that the probe friction force is not well known.

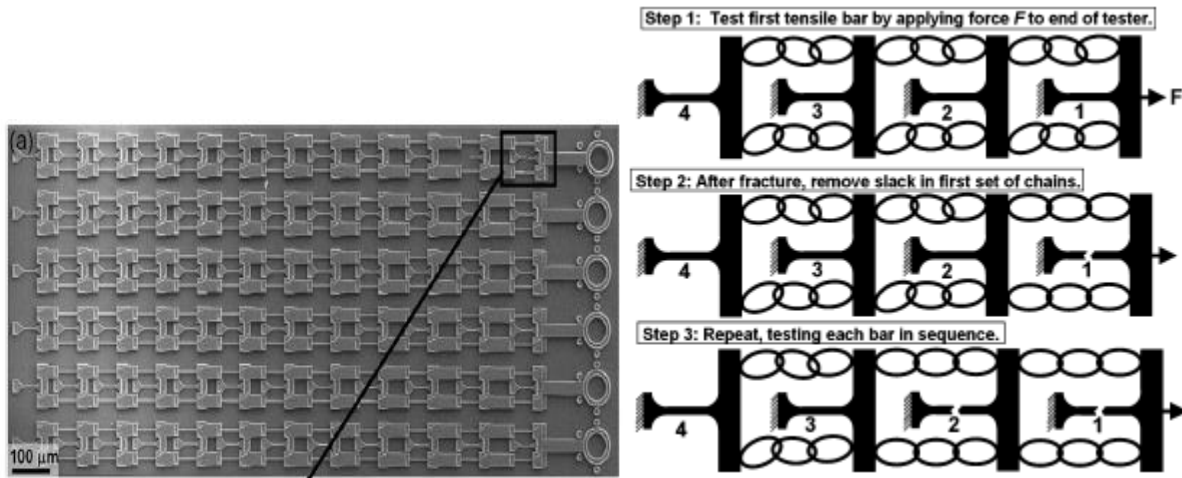


Fig 1.7 Slack chain test method by Boyce 2009

Espinosa et al. [48] developed the membrane deflection experiment as shown in Fig 1.8 . In this implementation, a fixed-fixed beam is loaded out of plane by a nanoindenter. The nanoindenter should be well aligned with the sample. Mirau interferometry is used to observe the deflection of the samples in real time; the deflection results are obtained from the interferometry while the force results are obtained from an atomic force microscope connected to the nanoindenter. The

specimens are long to approach state of uniaxial tension. Gold, copper and aluminum were tested using this test technique [49].

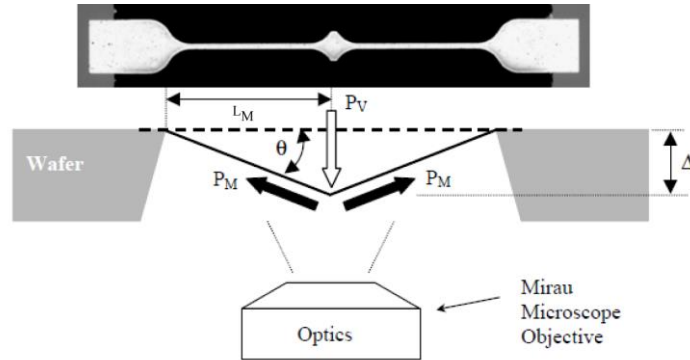


Fig 1.8 The membrane deflection experiment (Espinosa et al. 2003)

Uchic et al. [50], [51] developed the micropillar compression test. The micropillars were constructed by focused ion beam milling and a nanoindenter was used to compress these pillars. Sensors were attached to the nanoindenter to measure force and displacement. They were able to test and study size effect in single crystal Ni by using this technique.

The advantages of testing tensile specimens using off-chip actuation are simplicity and the wide variety of different materials that can be tested such as Al, Ni, Au, and Cu. However, the disadvantage of this approach is the difficulty in alignment of the actuator to the samples which might introduce uncertainty in the results depending on how effective the alignment process is.

### 1.3-2 Test Platforms with On-chip Actuators

One important advantage of on-chip actuation is the good alignment between the force and the longitudinal axis of the specimen. This aides tremendously in obtaining results whose accuracy

can be assessed with high confidence. The second major advantage is that because of the microfabrication process, hundreds to thousands of nominally identical samples can be produced. This enables assessment of the variability in mechanical properties. As we shall see, the variability in both polysilicon and aluminum thin films is significant and depends on size.

To implement on-chip actuation successfully, an actuator needs to be designed that provides sufficient force and displacement to fracture the specimen. The main type of actuator used in MEMS for on-chip testing of thin films is a chevron thermal actuator [44], [45]. It is a robust and reliable on-chip actuator that can apply large force and displacement. A current is applied through V-shaped beams resulting in a joule heating and expansion of the beams, which in turn leads to a rectilinear movement of the connected parts. The disadvantage of a thermal actuator is the large heat flow and temperature the specimen experiences during testing which considerably alters the mechanical properties of some materials. This inherent problem limits the applicability of thermal actuators to materials with properties that have a negligible temperature dependence.

Zhu et al. [52], as shown in Fig 1.9, developed a test system with heat sink beams emanating from the shuttle and connected to the substrate. The beams heat sinks are short for effective heat dissipation. The disadvantages of this design are the small displacement range and the force loss to the fixed beams which make the test system only applicable to nanoscale applications.

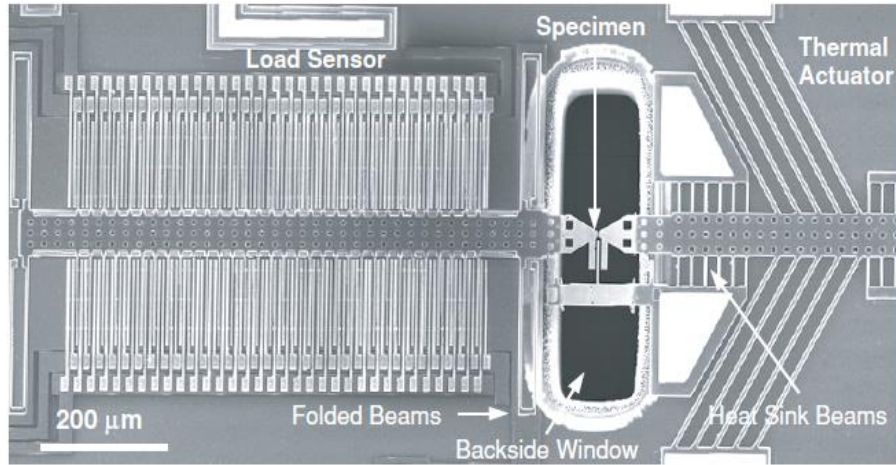


Fig 1.9 Test system for nano scale materials (Zhu et al 2006)

Gravier et al. [53] developed an on-chip test system that does not include a thermal actuator, rather the residual stress in silicon nitride is utilized for actuation. The test technique as shown in Fig 1.10 simply consists of a tensile specimen deposited on top of silicon nitride, which has a large tensile residual stress. The specimen is loaded upon the release of the structure. This technique enables the assessment of elongation to failure data for many samples [21], and an approximate failure probability versus elongation to failure plot has been constructed for various tensile specimen sizes. However, only one value of stress and one value of strain are extracted from each structure, and therefore the full stress strain curve cannot be determined for a given sample.

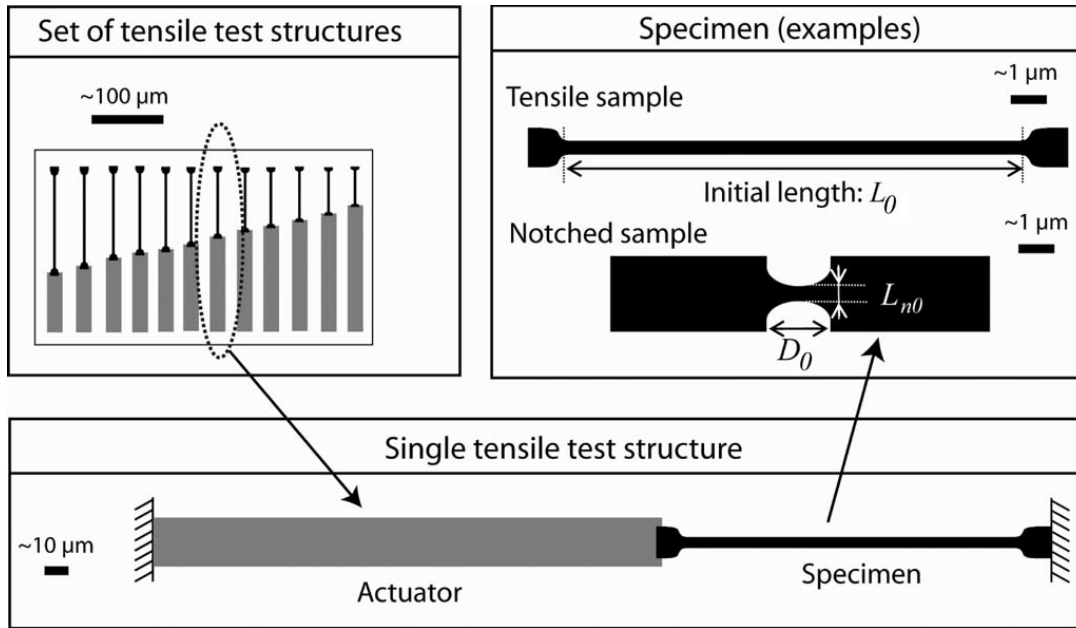


Fig 1.10 Schematic of test technique by Gravier et al. 2009

The on-chip testing methods that have been developed so far still suffer from some drawbacks such as the limited displacement range or the limited measurement data. So a new test system needs to be designed such that the whole stress vs strain curve is probed and the heat transferred to the specimen is limited.

## 1. 4 Test Set-up

### 1.4-1 Probe Station

The probe station used in this thesis is the same as that used by Hazra [54]. It consists of a light optical microscope equipped with a long-working distance interferometer, as shown in Fig1.11. The interferometric apparatus was obtained from EM Optomechanical Inc., NM, model 622-X. The microscope is equipped with a Sony XCD SX910 camera, mounted above the objective lens. The camera is connected to the computer through a firewire connection which enables

image acquisition. The mechanical tests are performed with custom MEMScript software developed at Sandia National Labs .

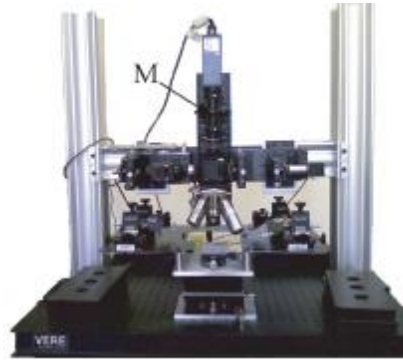


Fig 1.11 Optical microscope used in our mechanical test (Hazra 2010)

## **1.4-2 Scanning Electron Microscopy**

A scanning electron microscope was used to obtain qualitative and quantitative information such as a specimen's dimensions. The basic principle of the SEM is that it employs an electron beam directed toward the specimen to study its surface. A field emission gun (FEG) source is used to generate electrons and the electrons are accelerated to energy between 1 keV to 30 keV and directed toward the specimen. When the electron beam hits the specimen, secondary electrons scatter inelastically from the surface and these electrons are gathered by the detector to create the image. In our work, FEI Quanta 600 FEG SEM was used to study the specimens.

## **1.5 Contributions**

The major contributions of this thesis are listed next. Regarding the polysilicon specimens, the largest specimens were simple tensile bars, while the smallest specimens were notched. All the aluminum specimens were tensile bars.

### **Polysilicon thin films:**

- An existing test platform was evaluated. It was found that for smaller shorter specimens, bending occurred which biased results.
- A new test platform with excellent in-plane sample alignment for all specimen sizes was been developed for polysilicon testing. The new platform was modeled, designed, fabricated and tested with a specimen size range of 100.
- Test results indicated that polysilicon strength increased as specimen size decreased over a size range of 100 from 2.7 GPa to 4.2 GPa
- Prediction of strength size effects based on strength data from a single large tensile bar does not work very well. The strength data sets from two different size tensile bars are better at identifying threshold strength and yield a better prediction of the not only the characteristic strength, but also the strength distribution, of small specimens.
- Threshold strength is commonly taken to be a material property reflecting the largest flaw resulting from processing. For notched tensile bars, it is not a material property because for the same size flaw the apparent strength depends on the stress distribution across the notch region.
- Test results indicated that an upper bound to the strength of polysilicon is reached, as demonstrated by the observation that the strength distribution is the same between the two smallest specimen sizes. While all materials have an upper bound strength on the order of  $E/10$ , the maximum measured strength is well below this limit. The upper bound strength is not predicted by Weibull statistics.
- A new Monte Carlo simulation was developed to characterize and predict strength distribution of polysilicon.

- The Monte Carlo simulation fits the strength data of the largest specimen well and it predicts the strength distribution of the uniformly loaded specimens accurately. It does an adequate job at predicting the notched specimens stress distribution.

### **Aluminum thin films:**

- A new test platform for in-situ on-chip testing of aluminum was designed. The test platform incorporated high force, large displacement range thermal actuators and pre inserted microgrippers to relieve residual stress in the aluminum specimens.
- Heat can leak from thermal actuators into the aluminum test sample. The strength of this material is known to be temperature-dependent. This issue was resolved by introducing a thermal resistor and heat sinks that shunt heat to the substrate. Using finite element method, the temperature gradient along aluminum tensile bars is found to be less than 3 °C in air.
- Uncertainty analysis that the stress is measured within 5% accuracy and the modulus of elasticity  $E$  can be measured within 21% accuracy.
- Aluminum thin film structures over a size range of 6.5 increase in average yield strength from 140 MPa to 300 MPa. Unlike macroscale specimens, these samples also exhibit significant scatter in strength. The ratio of the standard deviation in yield strength to the average yield strength is 0.06 for 1  $\mu\text{m}$  thick samples, and more than doubles to 0.13 for 0.6  $\mu\text{m}$  thick samples.

## **1.6 Dissertation Organization**

This dissertation can has been divided into two main themes: Chapter 2 is concerned with the polysilicon size effect while Chapters 3 and 4 are concerned with aluminum test specimens and the aluminum strength size effect.

Chapter 2 discusses in details the work on polysilicon specimens. It begins by showing how the Weibull function is derived and used to estimate the strength size effect. It then analyzes the test platform that was used. Specifically, it is shown how to account for polysilicon residual stress so that the strength is properly quantified. Then, the Weibull function is used to predict strength and the prediction is compared with experimental data. The traditional approach of using a single threshold strength value is discussed from a linear fracture mechanics point of view and a new approach utilizing a weight function that depends on stress gradient in notched samples is used to modify the threshold strength and produce a better estimate to size effect.

Chapter 3 discusses the design of a test platform for aluminum thin film specimens. First we present the platform. The details of the thermal actuator characteristics, the load cell, the thermal isolation scheme and the pre-inserted grippers are described. Then we report preliminary results of stress versus strain curves. The chapter ends with a detailed error analysis of the test platform.

Chapter 4 is devoted to the study of the yield strength and elongation for the aluminum specimens for various specimen sizes. A simple mathematical model for the change in yield stress with size fits the data of the longest specimens well.

Finally, a conclusion and guidance for future work are presented in Chapter 5.

## **1.7 Journal Papers**

The following journal papers resulting from this thesis, and their current status is listed next.

1. Mohamed E. Saleh, Jack L. Beuth, and Maarten P. de Boer, “Validated Prediction of the Strength Size Effect in Polycrystalline Silicon Using the Three-Parameter Weibull Function”. *J. Am. Ceram. Soc.*, 1–9 (2014) (published)

2. Mohamed E. Saleh, Jack L. Beuth, Yoosuf N. Picard, Maarten P. de Boer, “ In-situ Platform for Isothermal Testing of Thin Film Mechanical Properties using Thermal Actuators” JMEMS (submitted March 20, 2015)
3. Vitali Brand, Mohamed E. Saleh, Maarten P. de Boer “Effects of Electrical Current and Temperature on Contamination-induced Degradation in Ohmic Switch Contacts” Trib. Letters, 85, 48-55 (2015) (published)
4. Mohamed E. Saleh, Jack L. Beuth, Yoosuf N. Picard, Maarten de Boer “Statistical Investigation of Size Effect of Yield Stress and Elongation for Free-standing Polycrystalline Al-0.5% Cu Thin Film” Scripta. Mat. (in progress)

## 1.8 Conference Presentations

The work in this thesis was presented at the following conferences:

1. “*The role of threshold strength on predicting polysilicon strength size effect,*” **M. Saleh**, M. P. de Boer and J.L. Beuth, MRS Fall Symposium JJ: Materials Fundamentals of Fatigue and Fracture, Boston, MA, Dec. 3, 2013.
2. “*An In-situ Test Platform Design for Testing Thin Film Mechanical Properties*”, **M. Saleh**, J.L. Beuth. Y. N. Picard and M. P. de Boer, Society of Experimental Mechanics Conference, Greenville, SC, June 5, 2014.
3. “*Novel in-situ testing technique for studying the mechanical properties of thin films*”, **M. E. Saleh**, J. L. Beuth and M. P. de Boer, Bennett Conference, Pittsburgh, PA April 25, 2014.

4. "*Investigation of strength-size effects in aluminum thin films*," **M. E Saleh**, J. L. Beuth, Y. N. Picard and M. P. de Boer, Bennett Conference, Pittsburgh, PA, March 20, 2015.

## Chapter 2: Polysilicon strength Size effect

As discussed in the Introduction of this thesis, it has recently been shown [17], [19] that a three-parameter Weibull function with a large threshold strength of  $\approx 2$  GPa is needed to accurately describe the failure strength statistics of a micromachined polycrystalline silicon specimen. In this chapter, we explore how to apply this function to predict strength size effects over a size range of 100. A two-parameter function is unsatisfactory in predicting the size effect. If a three-parameter Weibull fit to only the largest specimen is used, the prediction also does not satisfactorily agree with strength data in smaller specimens. The prediction is greatly improved if the two largest specimens, a factor of 10 different in size, are used for fitting. It is further demonstrated that the threshold strength depends on geometry in notched samples due to their large stress gradients [55].<sup>1</sup>

### 2.1 Introduction

Surface micromachined devices including accelerometers [56], [57], gyroscopes [58], and microphones [59] are key enablers in many products and applications used today in daily life. They are commonly fabricated from polycrystalline silicon (polysilicon), which is brittle, with measured fracture toughness  $K_{Ic}$  of  $0.82\text{--}1.2 \text{ Pa}\sqrt{m}$  [60]. As such, polysilicon can be considered to be a technical ceramic. Such materials possess a propensity toward brittle failure, which is of critical concern for micromachined products.

Weibull introduced a probability function to describe the strength distribution of brittle materials based on the weakest link concept [23], [24]. Investigators have used a two-parameter Weibull

---

<sup>1</sup> Most of the material in this chapter is reprinted from ref [55] with permission to be requested from the Journal of the American Ceramics Society.

(W2P) probability distribution function (PDF)  $P(\sigma)$  to *characterize* polysilicon strength  $\sigma$  at different size scales [11], [13], [15], [17]. Specimens display a size effect depending on surface area, [11], [17] in which specimens with larger surface area are weaker. Extensive SEM and TEM images have confirmed that specimens fail due to flaws at the surface, specifically at etched sidewalls [17], and exhibit the mirror, mist, hackle signatures typical of brittle materials [61]. Investigators attribute this to sidewall roughness [12], [13], [15], [16] or more specifically to crack-like flaws at grain boundaries that intersect sidewalls [19]. Typically about 30 specimens of each size were tested, and the W2P fits resulted in a Weibull modulus  $m$  of in the range of 10–20 [11]–[13], [15], [16]. Investigators have also applied W2P fits to *predict* the strength of brittle thin films at different size scales [12], [16], [19], [62]–[66]. While the predictions are good, W2P intrinsically assumes a minimum or threshold strength  $\sigma_u = 0$ . This would imply that there is a nonzero probability that any given specimen will fail at any nonzero applied load.

Recently, by testing large numbers of specimens, it has become clear that a three-parameter Weibull (W3P) distribution better describes the failure probability of polysilicon than does W2P. It was found that the W3P fit describes the failure of 1008 nominally identical specimens significantly better than does the W2P fit [18]. Using a sequential test method, Boyce found  $\sigma_u = 1.45$  GPa [18]. This result was corroborated using an entirely different *in-situ* test approach [19]. For 231 in-situ specimens, a value of  $\sigma_u = 2.08$  GPa was determined, while for 671 specimens tested by the sequential test method, a value of  $\sigma_u = 1.78$  GPa was determined. The specimens were cofabricated adjacent to each other on the same chips, thereby ruling out processing differences as a possible artifact [19]. The applicability of W3P to anisotropically

etched single crystal silicon has also been established [67]. Table 2.1 shows a summary of some of the work in polysilicon

Table 2.1 Summary of some of the work in polysilicon

Author/year	Geometry ( $\mu\text{m}$ )	No. of samples	Avg. No. of tests per sample	Avg. Strength enhancement (GPa)	Weibull modulus	Controlling flaws location
Tsuchiya/1998	t=2. w=2, 5. L=30, 100, 300	16	17	2-2.7	3.7-5.6	Surface
Ding/2001	t=2.4. w= 20, 40, 80, 100. L=100, 300 660	8	5	1.24-1.53	10.4-11.7	Not identified
Boyce/2007	t=1, 1.5, 2.25, 2.5 w=2. L=30, 150, 750, 3750	21	7	1.3-1.75 Poly2 1.65-2 Poly12 2.1-2.5 Poly3 2.4-3 Poly4	19.3-30	Surface
Greek/1997	t= 2, 10. w=10. L=1000	2	28	0.6-0.8	7-11	Surface
Bagdahn/2003	t= 3.5. w=20,50. L=250 Notch and hole with radius=2.5	6	30	1.27-2.83	6.2-6.9	Surface
Reedy	t=2.25. w=2. L=20, 70. Notch radius=0.6	3	616	2.5-4.1	3.03-5.78	Surface

The polysilicon results clearly demonstrate that  $\sigma_u > 0$  and that  $\sigma_u$  is large at  $\approx 2$  GPa [18], [19]. However, the tests covered only a relatively small range of specimen size—a factor of 3. A Weibull failure PDF is expected only if the distribution function  $g(a)$  of the effective flaw size ( $a$ ) fits a power law, that is,  $g(a) \sim a^{-n}$  [68]. Other requirements include [69] an absence of R-curve behavior, a single flaw distribution mode, *only* surface or *only* volume flaws, an absence of interactions between flaws and an absence of internal residual stress fields (e.g., due to thermal contraction interacting with elastically anisotropic grains[70] ).

Polysilicon microstructure exhibits only minor intrinsic toughening mechanisms due to local grain orientation changes and grain-boundary toughening [71]. Hence, there is negligible R-

curve behavior. As noted above, there is much evidence that only surface flaws control its strength. Specimens can be mass produced using modern microfabrication techniques, resulting in highly uniform processing. They can be tested by an in-situ apparatus without any handling or contact by other objects, minimizing the possibility of test artifacts such as unintended scratches or contamination. Strength scaling predictions can be validated by testing a wide range of specimen sizes [72]. A range of specimen sizes is easily accomplished using photolithographic methods. Hence, an excellent platform exists to probe polysilicon strength scaling effects.

A significantly smaller  $m$  results if W3P rather than W2P fits are used. This, in turn, results in a stronger strength scaling relationship. Therefore, it is important to assess the effectiveness of W3P in predicting strength scaling effects. In a first attempt to test polysilicon strength scaling using W3P, Reedy et al [19] studied the size effect in three different specimens, two of which were standard uniaxial tensile specimens with lengths of 20 and 70  $\mu\text{m}$  and width of 2  $\mu\text{m}$ . The third was a 10- $\mu\text{m}$ -wide double-edge-notched (DEN) specimen with a notch length of 3  $\mu\text{m}$  and notch radius of 0.6  $\mu\text{m}$ . In each case, the thickness was 2.25  $\mu\text{m}$ . While the larger two specimens could be related satisfactorily using W3P scaling fits (Fig. 9 of Ref. [19] indicates agreement within  $\sim 5\%$ ), the DEN specimen could not (Fig. 14 of Ref. [19] was underpredicted by  $\sim 30\%$ ).

Besides assessing W3P in predicting strength size effect, it would also be highly desirable to reduce the number of required tests. In this work, we test four different specimens over a size range of 100. We then examine several fitting methods to determine how best to predict strength scaling effects. We demonstrate that size effects are well predicted with 100 specimens from the largest two specimens, which are a factor of 10 different in size. Satisfactory predictions of both the characteristic strength and the full PDF for specimens another factor of 10 smaller are achieved.

This study is organized as follows. In Section 2.2, we review W2P and W3P Weibull scaling theory. In Section 2.3, we introduce and analyze a new in-situ test structure that enables accurate strength measurements for specimens a factor of 100 different in size. In Section 2.4, we report experimental results including a residual stress correction. In Section 2.5, the results are analyzed and it is found that only by accounting for the effect of stress gradient on  $\sigma_u$  in DEN specimens, good predictions are achieved.

## 2.2 Theoretical Background

According to the weakest link theory [23], [24], the probability of survival of  $n$  links in series can be expressed as

$$(1 - P) = (1 - P_i)^n. \quad (2.1)$$

Here  $P$  is the probability of failure of the entire structure,  $P_i$  is the probability of failure of the  $i^{\text{th}}$  link,  $(1 - P_i)$  is the probability of survival of the  $i^{\text{th}}$  link, and  $(1 - P)$  is the probability of survival of the chain.

The failure probability of the  $i^{\text{th}}$  link is assumed to follow a power law according to

$$P_i = k \cdot \sigma^m, \quad (2.2)$$

where  $k$  and  $m$  are constants and  $\sigma$  is the applied stress. Without loss of generality, it can be shown that the size and orientation of a flaw can equivalently be described by a single variable [68], [72], the effective flaw length,  $a$ , oriented normal to the applied uniaxial stress. Equation (2.2) then corresponds to assuming a power law in the effective flaw frequency distribution,  $g(a)$  [68]. The constant  $k$  can be chosen such that

$$k = V_i / \sigma_o^m, \quad (2.3)$$

where  $V_i$  is the volume of the  $i^{\text{th}}$  link, and  $\sigma_o$  will be defined below. Substituting Eqs. (2.3) and (2.2) into Eq. (2.1),

$$P = 1 - \left(1 - V_i \left(\frac{\sigma}{\sigma_o}\right)^m\right)^n. \quad (2.4)$$

For a continuum material, rupture can take place anywhere in the specimen. If a large number of links  $n$  is assumed, then using  $\exp(c) = \lim_{n \rightarrow \infty} \left(1 + \frac{c}{n}\right)^n$ , the Weibull function can be derived as

$$P = \lim_{n \rightarrow \infty} \left[1 - \left(1 - \frac{n}{n} V_i \left(\frac{\sigma}{\sigma_o}\right)^m\right)^n\right] = 1 - \exp\left(-V \left(\frac{\sigma}{\sigma_o}\right)^m\right). \quad (2.5a)$$

Here,  $m$  is the Weibull modulus and  $V$  is the total sample volume.  $m$  is considered to be a constant that reflects the flaw distribution (large  $m$  is associated with a narrow range of flaw sizes probed in strength tests of specimens of a uniform size). Also,  $\sigma_o$  ( $\text{GPa} \cdot \text{m}^{3/m}$ ) is a scale parameter, which is taken to be independent of the size or the shape of the structure, and  $V$  is the total volume of the structure.

So far, flaws are assumed to originate somewhere inside the volume. However, fracture initiates at surface flaws for polysilicon. In this case the volume in equation (2.5a) is replaced by the surface area,  $A$ . Then,

$$P = 1 - \exp\left(-A \left(\frac{\sigma}{\sigma_o}\right)^m\right), \quad (2.5b)$$

where  $\sigma_o$  now has units of  $\text{GPa} \cdot \text{m}^{2/m}$ . If there is a minimum or threshold strength value ( $\sigma_u$ ) below which the structure does not fail, the stress  $\sigma$  is replaced by  $\sigma - \sigma_u$

$$P = 1 - \exp\left(-A \left(\frac{\sigma - \sigma_u}{\sigma_o}\right)^m\right). \quad (2.6)$$

A second scale parameter, defined as

$$\sigma_{\theta} = \sigma_o(1/A^{1/m}) \quad , \quad (2.7)$$

has units of GPa. While  $\sigma_o$  has a unique value,  $\sigma_{\theta}$  depends on specimen size. Substituting back into Eq. (2.6), the W3P function is found as

$$P = 1 - \exp\left(-\left(\frac{\sigma - \sigma_u}{\sigma_{\theta}}\right)^m\right). \quad (2.8a)$$

The quantity  $(\sigma_{\theta} + \sigma_u)$  is called the characteristic strength. For  $\sigma = \sigma_{\theta} + \sigma_u$ ,  $P = 0.632$ . If  $\sigma_u = 0$ , then Eq. (2.8a) reduces to the widely-used W2P function.

For a given data set, Weibull parameters can be evaluated by taking the natural log of Eq. (2.8a) twice. The resulting linear equation,

$$\ln\left[\ln\left(\frac{1}{1-P}\right)\right] = m \cdot \ln(\sigma - \sigma_u) - m \cdot \ln(\sigma_{\theta}), \quad (2.8b)$$

can be fit to experimental strength data, as shown in Section 2.4. For  $N$  specimens, measured strength values are ranked  $r=1$  to  $N$  in ascending order and probability is assigned according to

$$P = (r - 0.5) / N. \quad (2.9)$$

For a small number of measured specimens ( $N \lesssim 40$ ), W2P fits the data satisfactorily [11], [12], [15], [17], [63], [64], [66]. As  $N$  increases to 233 [19] or 1008 [18], the quality of the linearized two-parameter fit diminishes and the data is better fit using three parameters [18], [19]. Hence, increasing values of  $N$  improve the estimate of the  $\sigma_u$  value.

In this work, we are interested in predicting the characteristic strength and strength distribution of different specimen sizes from a small  $N$  and a minimum set of specimen sizes. One

customary approach [16], [19], [62], [64], [66] is to estimate Weibull parameters from data of a single specimen size. The data is then fit to Eq. (2.8).

For two different size tensile bars at the same failure probability,

$$1 - \exp\left(-A_1 \left(\frac{\sigma_1 - \sigma_{u1}}{\sigma_{o1}}\right)^{m_1}\right) = 1 - \exp\left(-A_2 \left(\frac{\sigma_2 - \sigma_{u2}}{\sigma_{o2}}\right)^{m_2}\right) \quad . \quad (2.10)$$

Here  $\sigma_1$  and  $\sigma_2$  are the stresses applied to the two different size specimens for that failure probability. This equation reduces to

$$\frac{(\sigma_1 - \sigma_{u1})^{m_1}}{(\sigma_2 - \sigma_{u2})^{m_2}} = \frac{\sigma_{o1}^{m_1} A_2}{\sigma_{o2}^{m_2} A_1} \quad (2.11)$$

Equation (2.11) is general and can be used to compare results of two different size specimens from different micro-fabrication process and between different brittle materials type. But, usually specimens are compared from the same fabrication process and from the same materials. Therefore,  $\sigma_o$  is the same ( $\sigma_{o1} = \sigma_{o2} = \sigma_o$ ). For a single flaw population mode, the Weibull exponent will also be the same ( $m_1 = m_2 = m$ ). Finally the threshold strength, which is the estimated value of strength due the largest flaw, should be the same in uniformly stressed specimens ( $\sigma_{u1} = \sigma_{u2} = \sigma_u$ ). Hence, Eq. (2.11) reduces to the W3P scaling equation,

$$\frac{\sigma_1 - \sigma_u}{\sigma_2 - \sigma_u} = \left(\frac{A_2}{A_1}\right)^{1/m} \quad (2.12a)$$

Substituting  $\sigma_u + \sigma_{\theta j}$  for  $\sigma_j$ ,

$$\frac{\sigma_{\theta 1}}{\sigma_{\theta 2}} = \left(\frac{A_2}{A_1}\right)^{1/m} \quad (2.12b)$$

where  $\sigma_u + \sigma_{\theta j}$  is the characteristic strength of a specimen of area  $A_j$ . The scaling relationship is the same for W3P and W2P. In a W3P fit,  $\sigma_u$  is subtracted from the strength data. The range of  $\ln(\sigma - \sigma_u)$  in Eq. 2.8(b) becomes larger, which decreases  $m$ . Hence, proportionally, a larger strength scaling effect is expected if  $\sigma_u > 0$ .

In tensile bars of constant width, stresses are distributed uniformly along the gage section provided that the specimen is well aligned. Hence, polysilicon failure could occur anywhere along the sidewall area and the strength is expected to scale with the sidewall area according to Eq. (2.12b). If the stress distribution along the sidewall area is not constant as in the case of notched tensile bars, the generalized form of Eq. (2.6) is

$$P = 1 - \exp\left(- \int_{Area} \left(\frac{\sigma_{notch} - \sigma_{u,notch}}{\sigma_o}\right)^m dA\right) \quad (2.13)$$

Here,  $\sigma_{notch}$  is the stress along the sidewall, and  $\sigma_{u,notch}$  is the threshold strength for a notched specimen. Equation (2.13) is used with a finite element model of the notched specimens and numerical integration is performed to determine the probability at different applied loads. The value for  $\sigma_o (= \sigma_{\theta} A^{1/m})$  is determined from experiments as seen in Section 2.4 below. Also, an equivalent area of the notched specimens can be defined as the area of a tensile bar that has the same probability of failure as a notched specimen. Therefore, the equivalent area for each notched specimen can be determined by applying Eq. (2.13). Then, using the stress in the notch region, Eq. (2.12) is applied to determine the equivalent *uniformly stressed* area. In the present work, all specimens have the same thickness  $t$  and therefore, the controlling factor is the sidewall length. Thus, the results are presented in terms of effective length,  $L_{eff}$ , rather than equivalent area,  $t \cdot L_{eff}$ .

## 2.3- Experimental Approach

A very useful *in-situ* test platform to test the mechanical properties of polysilicon was designed by Hazra [54]. The test platform introduced a gripper mechanism for gripping the tensile specimen which completely relieves the residual stresses from the specimens. We had originally intended to use Hazra's design for our work, so several tests were performed using this design. However, a misalignment issue was discovered during our tests and this issue was more critical for the smaller scale tensile bars tested in this project. Therefore, a new test platform was developed and used in our studies. The misalignment issue with Hazra's design for the small specimens is discussed in Appendix A. In this section we describe and analyze our new test platform.

### 2.3-1 Test Platform and Tensile Bar Designs

As presented in Fig. 2.1, the new test platform consists of a microtensile bar connected to the substrate through an anchor pad on one side. On the other side it is connected to a crosshead which is in turn connected to a thermal actuator (TA) through a shuttle. The TA expands forcefully due to Joule heating when current passes through its legs until the tensile bar fractures. A displacement gage is connected to both sides of the crosshead and the tensile bar displacement is optically monitored (objective numerical aperture=0.55, camera magnification=50 X). The change in displacement is determined to ~5 nm accuracy by detecting the relative phase of reference and object gratings. As detailed below, a linear finite element model of the test structure is used to calculate tensile bar strain from the displacement data. A value of Young's modulus  $E=164$  GPa [9] is assumed to calculate stress from the strain. The heat sink serves to shunt heat to the substrate to minimize the tensile bar temperature excursion. The fracture

strength of polysilicon is insensitive to temperatures up to at least 200 °C [17]. For this test platform geometry and for applied voltages used in the tests, it was estimated by finite element analysis (FEA) that the specimens reach a maximum temperature of 200 °C.

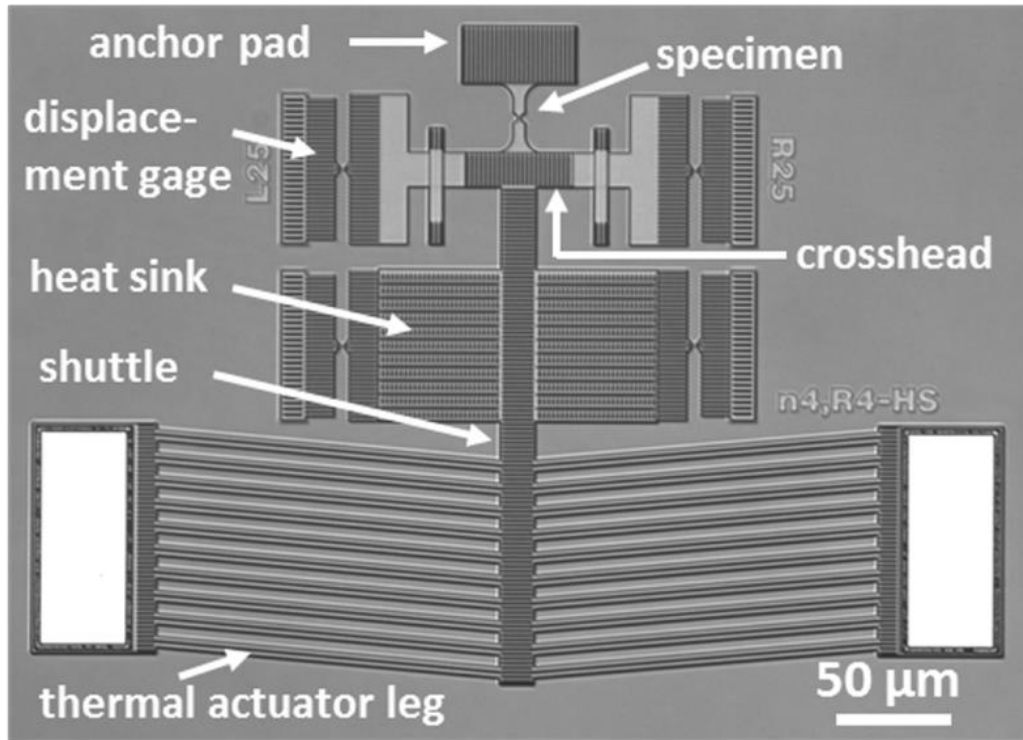


Fig. 2.1 Optical image of test platform. The salient features including the thermal actuator, shuttle, crosshead, displacement gage, and anchor pad are indicated.

The tensile specimen geometries, as indicated in Fig. 2.2, include two uniformly stressed tensile bars and two double edge-notched (DEN) tensile bars. The uniform tensile bars have gage lengths of 70 and 7 μm and their width is nominally 2 μm. Shorter gage sections begin to be influenced by stress contours penetrating from the fillets. Therefore, double edge notched (DEN) tensile bars were designed. They are 10 μm wide and have 4 μm deep notches on each side. Their notch radii are 4 μm and 1 μm for the 4/4 and 4/1 DEN specimens, respectively. The thickness of all tensile bars is 2.25 μm -- only the in-plane dimensions are used to vary the

specimen geometry. The actual widths are less due to a linewidth loss of  $\sim 0.1 \mu\text{m}$  per edge due to etching ( $0.2 \mu\text{m}$  total). The specimens in Fig. 2.2 are henceforth referred to as Specimens 1-4 (Sp 1-4 in figure legends), respectively. The geometries chosen increase the range of  $L_{eff}$  to 100X compared 3.5X [19]. Details of the thermal actuator leg geometry are given in ref. [73].

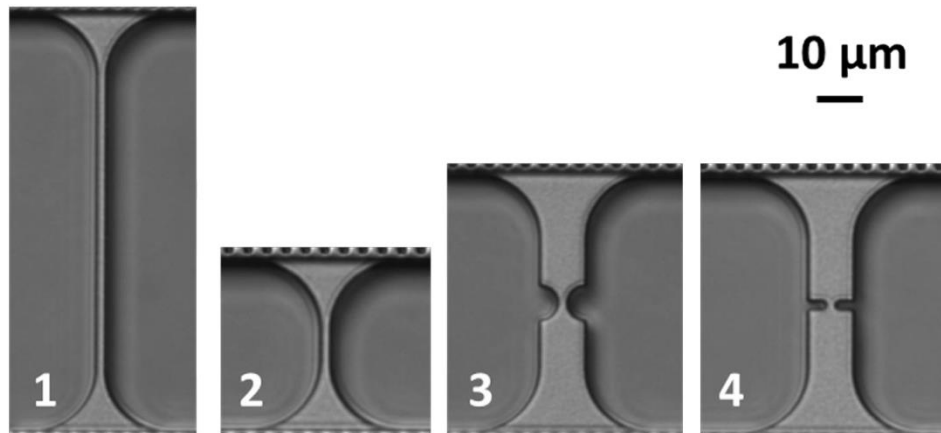


Fig. 2.2 Optical images of Specimens 1–4. (1)  $70 \mu\text{m} \times 2 \mu\text{m}$ , (2)  $7 \mu\text{m} \times 2 \mu\text{m}$ , (3) 4/4 DEN, and (4) 4/1 DEN (DEN = double-edge notch, Specimens 3 and 4 are  $10 \mu\text{m}$  wide, have  $4 \mu\text{m}$  deep notches and a radius of curvature designated by the number after the slash).

The test platform design is a variation on our previous work [54], [73], [74]. The main difference is that the previous design incorporated prehensile grippers between the shuttle and the crosshead. Male grips were first inserted into female grips by expanding the TA legs. Then, the voltage was reduced, the grips engaged and fracture occurred. That approach had the advantage of eliminating the need to account for residual stress in the analysis. However, it was found in preliminary work that the shorter stiffer Specimens 2-4 were not well aligned, giving rise to in-plane bending and non-uniform stress. This issue was noticed because displacement readings were significantly different depending on whether the gage on the left or the right of Fig. 2.1 was used. The new design directly connects the shuttle to the crosshead. Alignment is

always maintained but this configuration imparts residual stress into the specimen, which must be taken into account.

The test platforms were fabricated using the Sandia National Labs SUMMiT V micromachining process [25]. Five polysilicon layers are manufactured, four of which are freestanding after releasing them from sacrificial oxide material in hydrofluoric acid in the last process step. The test specimens are in the third layer, designated as MMPOLY3, while the thermal actuator legs consist of three layers – MMPOLY12, MMPOLY3 and MMPOLY4 – that are connected by sacrificial oxide cuts. The same process was previously used to fabricate similar samples in refs. [18] and [19]. Cross section images (Fig. 4 in ref. [19]) of fractured tensile bars indicate nearly vertical sidewalls (i.e. no apparent taper). Atomic force microscope scans (Fig. 10 of ref. [19]) of the sidewalls using a 3-4 nm radius of curvature tip indicate columnar grains of  $\sim 0.2$  to  $0.6 \mu\text{m}$  diameter,  $\sim 20$  nm root mean square surface roughness and grooves as deep as 40 nm which are thought to be generated by preferential etching of sidewall grain boundaries. Extensive fractography revealed that cracks originate at sidewalls [18], [19].

## **2.3-2 Test Structure Analysis**

We first outline the procedure for quantifying residual stress in the TA legs. Then, we discuss procedure for extracting fracture strength from the displacement measurements.

### **2.3-2-1 Residual Stress**

After fabrication, the thermal actuator legs are under a small compressive residual stress ( $\approx 10$  to 20 MPa). The residual stress is taken to be uniform within the specimen, unlike the non-uniform residual stresses between anisotropic grains mentioned in the Introduction. Because they are

force amplifiers, expansion of the thermal actuator legs during the release process induces a significant stress in the tensile bar, which acts to constrain their expansion.

The stress imparted to the test specimens must be quantified for accurate determination of strength data. To this end, two finite element analysis (FEA) models were created. One model is for the TA legs and the other is for the specimen. In the TA model, a uniform residual stress was applied in the legs and they were allowed to expand freely. Then a force was applied to the shuttle, and displacement was extracted. By doing so, force-displacement curves were constructed for TA legs with different values of residual stress as shown by the solid lines in Fig. 2.3. For the test specimen model, a force was applied to the crosshead end and the displacement was extracted, as indicated by the dashed lines in Fig. 2.3. (The shuttle between the TA legs and the crosshead is constructed of three layers of polysilicon and is effectively rigid compared to the test specimens). The thermal actuator legs and the tensile bar are in static equilibrium. The force after release, but before test, lies at the point of intersection of the TA and tensile bar load lines, as designated for Specimen 2 by the circle in Fig. 2.3. The specimen displacement due to TA residual stress alone is designated by  $d_a$ . When the TA fractures, it will no longer exert force, and its displacement will increase. This is represented by  $\Delta d$  in Fig. 2.3, and can be obtained by measurement.

As shown in Fig. 2.4, a voltage is applied until the tensile bar fractures, at which point there is a large excursion in the displacement because the tensile bar no longer acts as a constraint. Further voltage increments are applied because the voltage needed to fracture specimens in *all* tests must be exceeded. Then the voltage is reduced to 0 V and  $\Delta d$  is obtained. In Fig. 2.4,  $\Delta d_2$  indicates the free expansion of Specimen 2. This dimension was also indicated on Fig. 2.3. There is a unique starting point of residual stress at which the  $\Delta d_2$  arrow begins (at 15 MPa in Fig. 2.3)

such that the vertical extension at the arrow end intersects the pre-measurement static equilibrium indicated by the circle. This determines the residual stress. Values ranging from 14 to 18 MPa were found across all test specimens. This is in reasonable agreement with a previously published value for the SUMMiT V process [8].

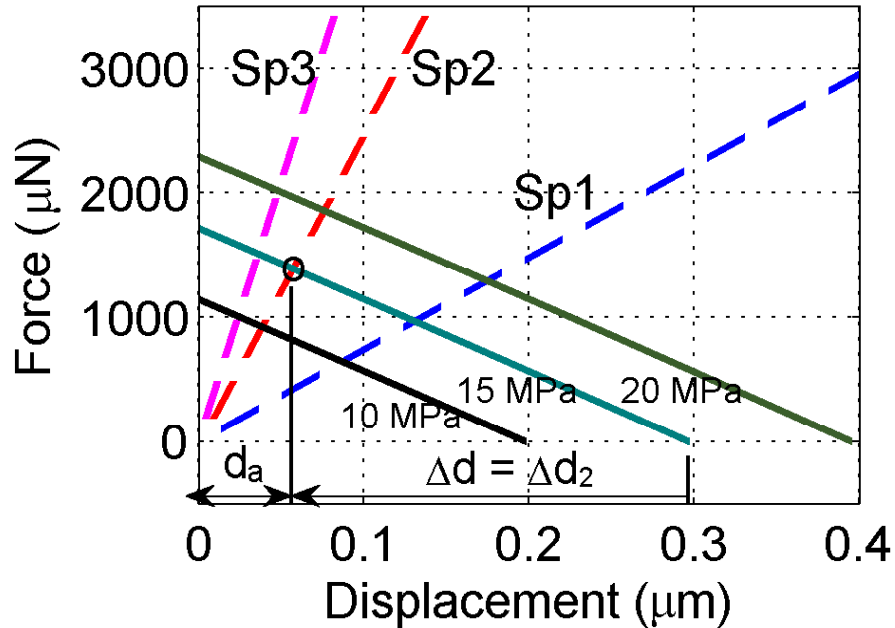


Fig. 2.3. Determination of residual stress from the force displacement plot. There is a single starting point of residual stress at which the  $\Delta d_2$  arrow begins such that the vertical extension of the arrow end intersects the tensile bar load line/residual stress intersection.

A concern with this method is that the TA legs could experience permanent deformation due to heating while they were actuated, and therefore that the  $\Delta d$  value will be larger than that due to elastic extension alone. To check this, the same actuator was raised to larger voltages of 6 and 7 volts. No difference was noted in  $\Delta d$  even at 7 V.

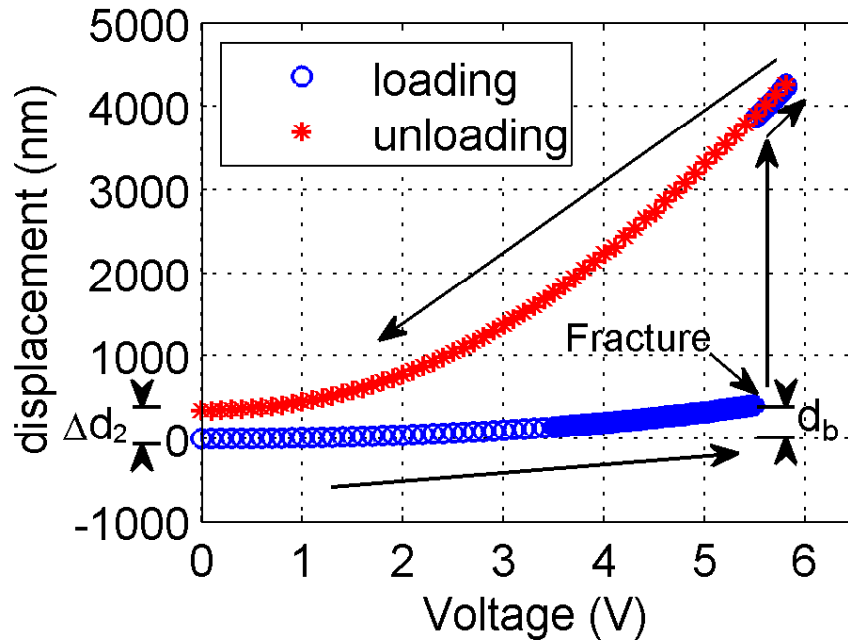


Fig. 2.4. Example measurement of test sample fracture in Specimen 2, and of the residual displacement  $\Delta d_2$  due to the elastic expansion of thermal actuator legs after fracture.

A correction to the above analysis relates to specimen linewidth loss. The tensile bar linewidth is not the same as the nominal linewidth in the original design due to processing steps such as photolithography and etching. This reduces the calculated slope of the specimen load line. There also are known variations in linewidth loss across a wafer due to process non-uniformities. However, test platforms adjacent to each other on the chip will have very almost the same linewidth loss. Therefore, these effects were accounted for by comparing results in adjacent test platforms, one containing Specimen 1 and the other Specimen 2. Specifically, for two adjacent Specimens 1 and 2,  $\Delta d_1$  (reflecting  $\Delta d$  for Specimen 1) and  $\Delta d_2$  data were measured. The slopes of lines Sp 1 and Sp 2 in Fig. 2.3 were determined for different linewidth losses. When a particular value of linewidth loss was used, a unique residual stress value was found. This value was typically  $0.10 \mu\text{m}/\text{edge}$ , in good agreement with previous SEM measurements. Hence, in

addition to yielding more accurate results, the method also serves as a way to determine linewidth loss by a mechanical means.

Finally, due to its residual compression, the tensile bar will actually have a small displacement at zero force. This will shift the tensile bar load line slightly to the right in Fig. 2.3. This shift, however, is small. For Specimen 1, it is 9 nm if the residual compression is 20 MPa, which can be compared with 180 nm induced by the TA legs. It is less for the other specimens.

### **2.3-2-2 Finite element analysis of the notch region**

As seen in Fig. 2.4, voltage was increased while monitoring the change in displacement until fracture. At low voltages (0-3.5 V), the increments were large (0.10 V) because the displacements are small. Above 3.5 V, the increments were reduced to 0.02 V to maintain high displacement resolution.

The displacement to fracture,  $d_f$ , is the sum of the calculated displacement due to residual stress ( $d_a$ , Fig 2.3) and the change in displacement until fracture ( $d_b$ , Fig 2.4),

$$d_f = d_a + d_b . \quad (2.14)$$

The displacement to fracture is itself the sum of the gage section and fillet region extensions. A two-dimensional linear FEA was performed to determine the gage section displacement component. A compliance calibration factor ( $c_f$ ) was extracted from the analysis for Specimens 1 and 2. It is the ratio of the gage section displacement to the total displacement of the tensile bar including the fillets. Hence, the strength of the tensile bar is calculated by applying Hooke's law as

$$\sigma_f = c_f \frac{d_f}{L} E \quad (\text{Specimens 1 and 2}) , \quad (2.15a)$$

where  $L$  is the length of the gauge section and  $E$  is Young's modulus.

FEA was also performed on Specimens 3 and 4. The stress to displacement ratio ( $s_{dr}$ ), i.e., the ratio of the stress at the notch root to the applied displacement was extracted. The fracture displacement from experiments was converted to fracture stress according to

$$\sigma_f = s_{dr} \cdot d_f \quad (\text{Specimens 3 and 4}) \quad . \quad (2.15b)$$

## 2.4 Results and Discussion

Between  $N=43$  and 75 specimens were tested of each type for a total number of 237 strength tests (Appendix B contains the displacement results for different specimen). After each fracture, the specimen was inspected optically. All tensile specimens fractured in the gage section, while all DEN samples fractured in the notch region. An example of a fractured Specimen 4 is shown in Fig. 2.5. We first present the probability versus strength results. Then we examine Weibull scaling procedures in order to compare predictions to results.

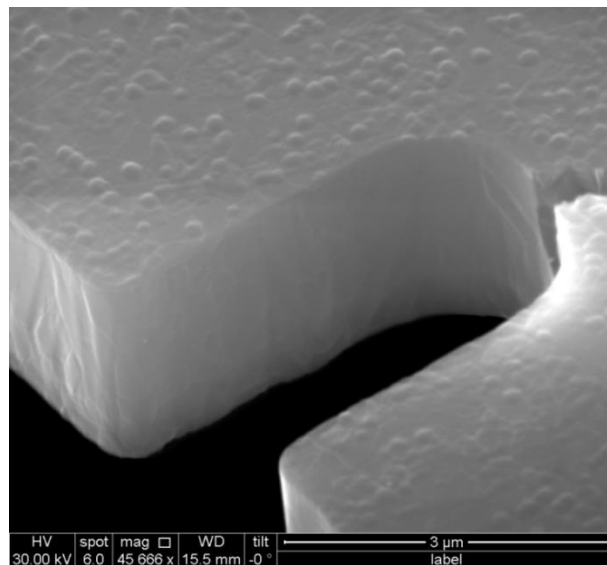


Fig.2.5. SEM image of a fractured Specimen 4 (4/1 DEN).

## 2.4-1 Strength distribution

The data points in Fig 2.6 show the strength distribution for each tensile bar after accounting for the residual stress as described in Section 2.3-2, and indicates a significant size effect. For a given strength value, the main uncertainty is due to the displacement value. The displacement measurement error (measured 20,000 times over a 1000 minute time frame) was analyzed and found to be  $\pm 5$  nm (one sigma). It is due to focus variations, which are caused by thermal expansion of aluminum rails that support the microscope objective. This is ultimately due to room temperature variations of  $\pm 2$  °C. An autofocus routine corrects for the thermal expansion, however the noise floor is due to the vertical stage step size limit. The displacement uncertainty itself is the same for all specimens, but smaller specimens have greater stiffness. The corresponding uncertainties for each measured strength value were calculated to be  $\pm 0.0025$ ,  $\pm 0.025$ ,  $\pm 0.05$  and  $\pm 0.1$  GPa for Specimens 1-4 GPa, respectively. This is small compared to the differences in the strength populations; hence they are clearly distinct.

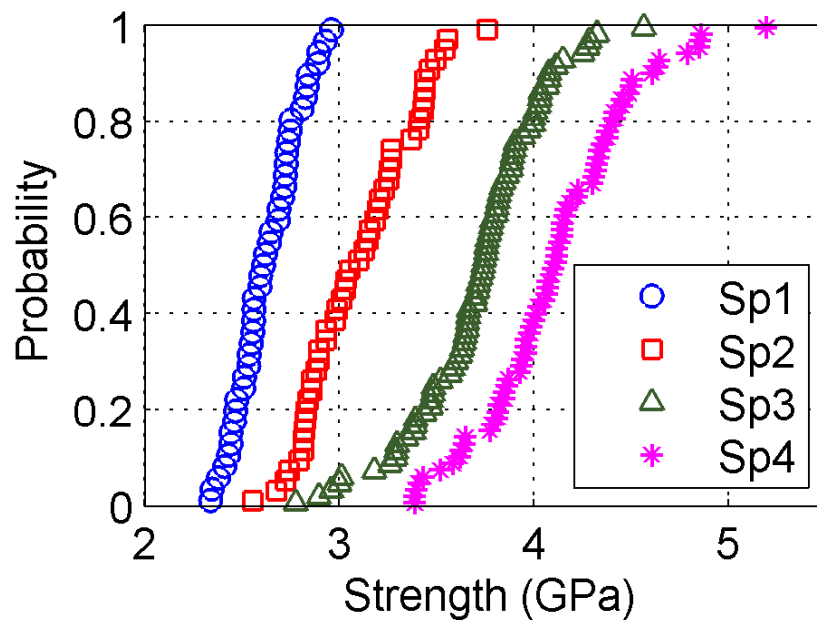


Fig. 2.6. Probability versus strength data for Specimens 1–4.

## 2.4-2 Analysis 1 - Strength prediction based on Specimen 1

The data for each specimen was fit both to W2P and W3P functions (see Appendix C, Fig. C1). For W3P, the maximum likelihood method [75]–[77] was used to obtain the Weibull parameters. Although W3P fits were better, the difference was not large, as expected given that  $n$  was well below 100 for each specimen. Our focus here is to assess the fits with respect to how well each predicts the strength size effect. Using Specimen 1 and Eq. 2.12(b) and Eq. 2.13, a W2P fit to predict the Specimen 2-4 data was performed, but was clearly inadequate (see Fig. C2 in Appendix C). We therefore examined the effectiveness of W3P scaling procedures.

Fig 2.7 shows the W3P fit for Specimen 1, plotted in linearized form as in Eq. 2.8(b). Values of  $\sigma_u=2.18$  GPa and  $m=3.05$  were found, in good agreement with the values reported of  $\sigma_u=2.08$  GPa and  $m=3.03$  in ref. [19], where  $N=233$  tensile bars were tested. The scale parameter value  $\sigma_o=3.4$  GPa $\cdot\mu\text{m}^{2/3.05}$  was estimated from Eq. (2.7) (as seen in Table 2.2,  $\sigma_{\theta 1}=0.52$  GPa, while the area for Specimen 1 is  $A=2\times 70\ \mu\text{m} \times 2.25\ \mu\text{m}$ ). The scale parameter was used with the stress distribution along the notch radius and Eq. (2.10) to estimate the stress distribution and the equivalent length ( $L_{\text{eff}}$ ) for Specimens 2-4. Values are listed in the  $L_{\text{eff}}$  column of Table 2.2.  $L_{\text{eff}}$  was determined iteratively, using Eq. (2.12). As seen in Fig. 2.8, Specimen 1 predicts the strength distribution of Specimen 2 well, but it does a poor job at predicting the distribution for Specimens 3 and 4. If we are only interested in estimating the characteristic strength ( $\sigma_{\theta}+\sigma_u$ ), then the maximum difference between the experiment and prediction is 7%. While this is in on par with the value of 9% that reported in [16], the overall fit is unsatisfactory.

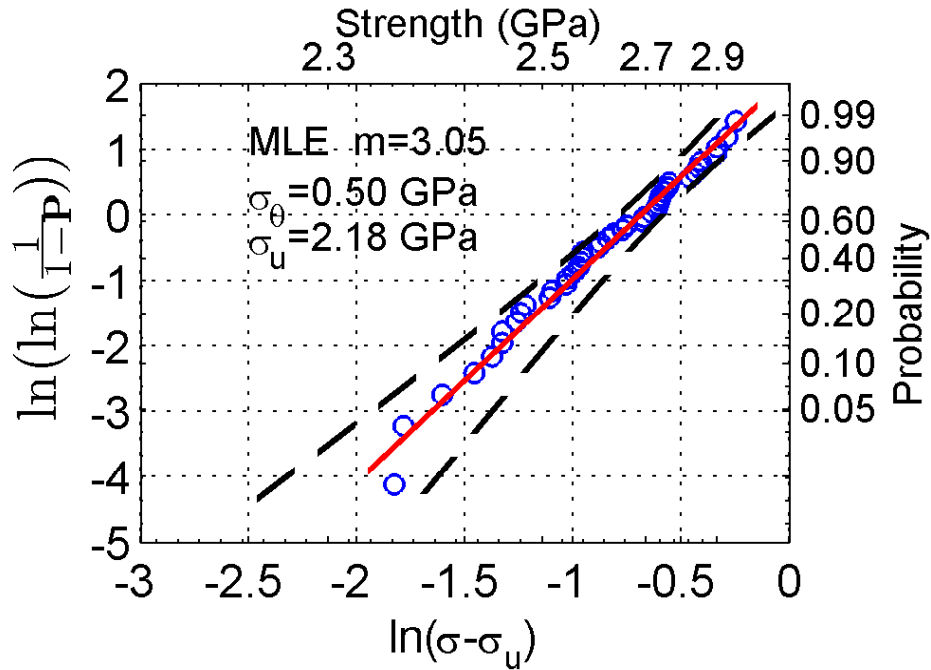


Fig. 2.7. Determination of the three Weibull parameters from Specimen 1 using the maximum likelihood method. The solid red line indicates the MLE fit. The dashed black lines represent the 95% confidence interval.

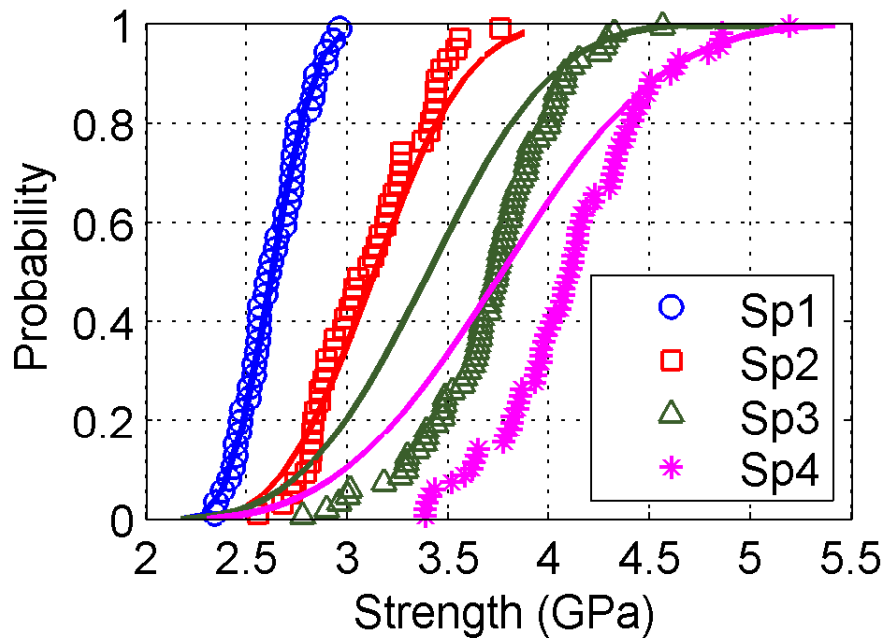


Fig. 2.8. Prediction (solid curves) of the strength distribution compared to the experimental results based on Analysis Method 1. Low values of  $Q$  result for Specimens 3 and 4.

The goodness of fit,  $Q$ , was calculated to assess the quality of the fits quantitatively. Accordingly,

$$Q = 1 - \frac{\sum_{j=1}^N (\sigma_j - \hat{\sigma}_j)^2}{\sum_{j=1}^N (\sigma_j - \bar{\sigma})^2}, \quad (2.16)$$

where  $\sigma_j$  and  $\hat{\sigma}_j$  are the strength and the predicted strength of the  $j^{\text{th}}$  sample of a given specimen, respectively, and  $\bar{\sigma}$  is the mean strength. A good fit is indicated by  $0.95 < Q < 1$  [78]. It is seen in Table 2.2 that  $Q > 0.95$  for Specimen 1, but is near or below 0 for Specimens 3 and 4.

The results for Analysis 1 are summarized in Table 2.2, which includes columns for  $L_{\text{eff}}$ , the compliance calibration factor ( $c_f$ , tensile bars) and the stress displacement ratio ( $s_{dr}$ , DEN specimens). The characteristic strengths  $\sigma_\theta + \sigma_u$  are also listed.

Table 2.2: Analysis 1 - using only Specimen 1 to make scaling predictions with W3P  $\sigma_u = 2.18$  GPa,  $\sigma_o = 3.4$  GPa  $\bullet \mu\text{m}^{2/3.05}$  and  $m = 3.05$

Specimen ( $N$ )	$\sigma_u$ (GPa)	$\sigma_\theta + \sigma_u$ (GPa)	$c_f$ or $s_{dr}^*$	$L_{\text{eff}}$ ( $\mu\text{m}$ )	% diff in $\sigma_\theta + \sigma_u$ (exp. vs. pred)	$Q$
1 (43)	2.18	2.69	0.83	140		0.99
2 (45)	2.18	3.19	0.33	14	2.5	0.73
3 (75)	2.18	3.81	0.012*	6.5	6.9	0.03
4 (74)	2.18	4.19	0.017*	2.9	5.1	-0.2

### 2.4-3 Analysis 2 -- Strength prediction based on Specimens 1 and 2

One possible reason that Specimen 1 does not predict the strength of Specimens 3 and 4 well is that the polysilicon etch may behave differently in the notch regions than in sidewalls. However, visual SEM examination revealed no clear differences, as seen in Fig. 2.5. Also, even when large roughness changes are measured, only relatively small average strength changes are seen

( $\approx 0.02$  GPa per nm of root mean square (rms) roughness from both refs. [67] and [79]). Given the small change in roughness here (likely less than a few nm rms), it is unlikely that the strength change is due to roughness changes.

A more likely explanation relates to the observation that Specimen 1's strength does not exceed 3 GPa, while Specimen 4's strength extends to 5 GPa. Hence, the Analysis 1 prediction assumes that the Weibull parameters apply far above the strength region from which they were extracted. Even if  $N=1,000$  data points were taken for Specimen 1, it can be shown from the Weibull fit that the strongest would be only  $\approx 3.1$  GPa with  $P=0.9995$ . However, Specimen 2 strength extends to 3.8 GPa. Perhaps by combining the data from these specimens and optimizing the parameter fit across both specimens, better  $\sigma_u$  and  $m$  values can be obtained for strength predictions. This idea is related to the work of Danzer et al. [72], who recommended testing  $\approx 30$  samples of many different sizes in order to detect multimodal flaw populations. In the present data set, Specimens 1 ( $\sigma_u=2.18$  GPa and  $m=3.05$ ) and 2 ( $\sigma_u=2.47$  GPa and  $m=2.46$ ) are each reasonably well described by W3P with a single value of  $m$ , implying a unimodal flaw distribution. The differences in the  $\sigma_u$  and  $m$  values can be attributed to the high sensitivity of these parameters when  $N$  is small.

It can be further rationalized that  $\sigma_u$  and  $m$  are the same for Specimens 1 and 2. Both are uniformly stressed tensile bars, so  $\sigma_u$  should be equivalent. From 2.55 to 2.96 GPa the strength data overlap for Specimens 1 and 2 (as can be seen by drawing vertical lines at these values in Fig. 2.6), indicating that much of the same flaw population is sampled. For Specimens 1 and 2, this represents probabilities from  $0.36 < P_1 < 1$  and  $0 < P_2 < 0.36$  (where the  $P$  subscript refers to the specimen), respectively (as can be seen by drawing horizontal lines intersecting the vertical lines

for the respective specimen). The strength overlap is hence over 36% of the  $P_2$  range, and both populations appear to be unimodal. The procedure to determine the best combined fit for  $\sigma_u$  and  $m$  to Specimens 1 and 2 was as follows. First, a value of  $\sigma_u$  was chosen. Then, a least squares fit was performed for each specimen according to Eq. 2.8(b). This process was repeated for different values of  $\sigma_u$  until a value was found in which  $m$  was the same for Specimens 1 and 2. As shown in Fig. 2.9, the fits are qualitatively good for both specimens. The resulting parameters are  $\sigma_u=1.95$  GPa,  $\sigma_o=2.47$  GPa $\cdot\mu\text{m}^{2/4.8}$ , and  $m=4.83$ .

Kolmogorov–Smirnov (KS) test [80], [81] and Cramer-von Mises (CvM) [82] goodness of fit test leads to values of 0.35 and 0.29 from KS and 0.38 and 0.23 from CvM for specimens 1 and 2 respectively, which indicate that the null hypothesis that the assumed fit to the experimental data cannot be rejected at the 5% significance level

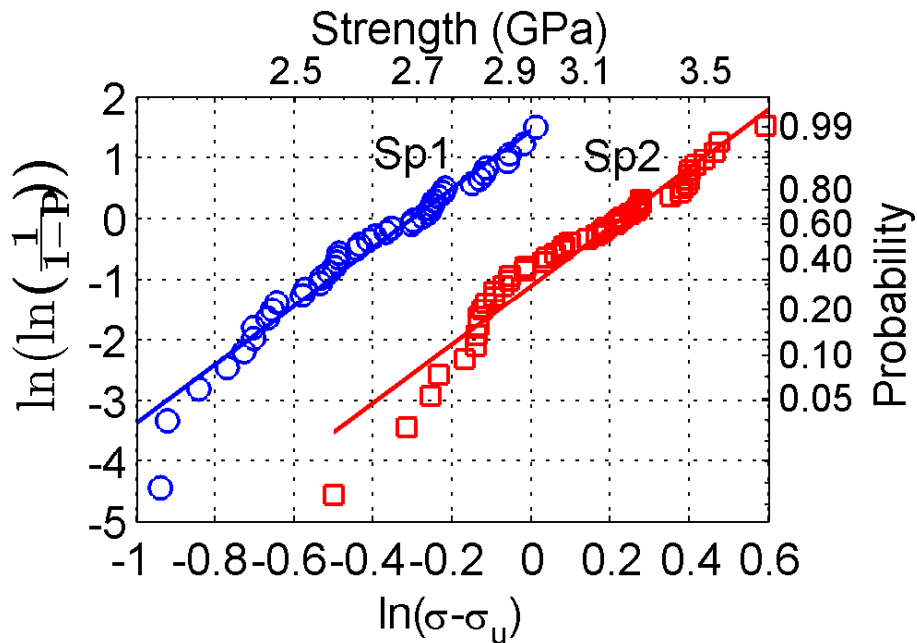


Fig. 2.9. Determination of Weibull parameters based on Specimens 1 and 2.

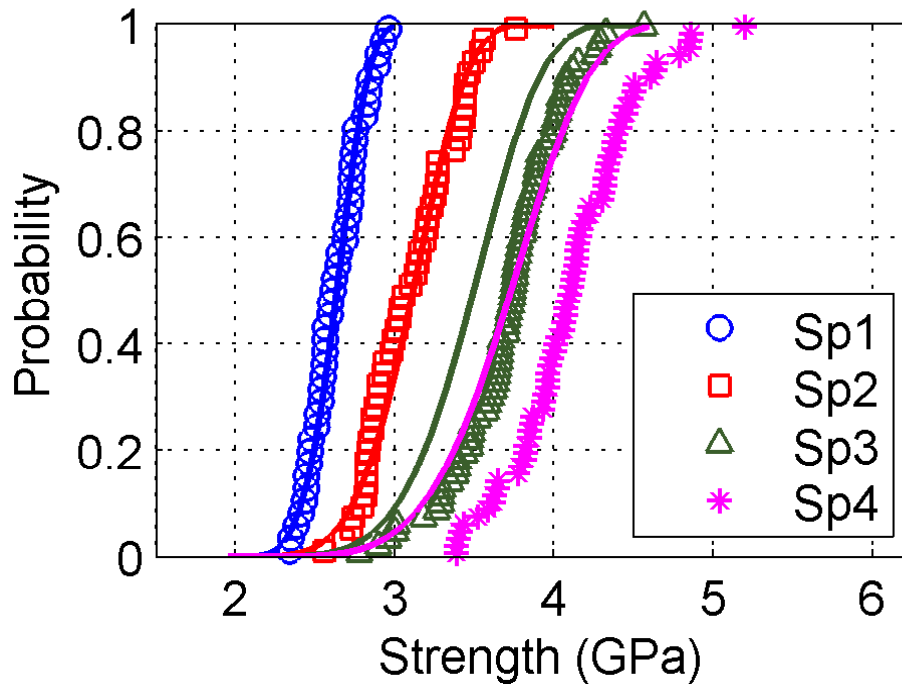


Fig. 2.10. Fitting Specimens 1 and 2 then predicting Specimen 3 and 4 probability distribution functions (solid lines) without accounting for change in threshold strength.

The probability curve prediction for Specimens 3 and 4 was now improved, as seen in Fig. 2.10. The values of  $Q=0.97$ ,  $0.96$ ,  $0.53$  and  $-0.16$  were found for Specimens 1-4, respectively. This remains unsatisfactory. The underlying reason is that the concept of strength in a non-uniform stress field requires more detailed consideration. There is a stress gradient across the width of the DEN specimens. A general theoretical formulation of the effects of stress gradient on strength and Weibull analysis has been presented by other authors [83]–[85]. With an assumed distribution of flaw sizes and orientations, it is found that in the presence of a stress gradient the failure probability is lower than for the case of constant stress. Here, we provide a simple analysis by calculating the effect stress gradient effect on  $\sigma_u$  and compare it with the data. Let us associate the largest effective critical flaw length,  $a_c$ , with  $\sigma_u$  from Specimens 1 and 2, and estimate its length by linear elastic fracture mechanics. Accordingly,

$$a_c = \frac{1}{\pi} \left( \frac{K_{Ic}}{1.122\sigma_u} \right)^2, \quad (2.17)$$

where  $K_{Ic} = 1.2 \text{ MPa}\cdot\sqrt{m}$  is the critical stress intensity factor for polysilicon [60]. Based on Eq. (2.17) the largest effective critical flaw length that the microfabrication process produces is  $a_c=96 \text{ nm}$ .

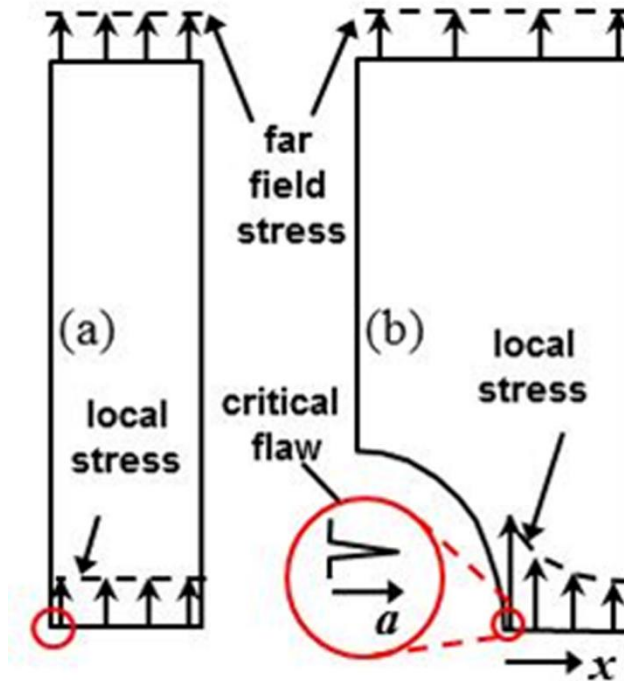


Fig. 2.11. Schematic view of local stress distribution in uniform and notched samples

The maximum flaw size should be the same for the DEN specimens but the stress decreases across the notch width as seen in Fig. 2.11. Therefore,  $\sigma_u$  depends on geometrical details for Specimens 3 and 4. To determine  $\sigma_u$ , the stress along the notch root was extracted by FEA. Assuming that the maximum flaw is present at the notch root, an iterative method was performed to estimate the threshold strength utilizing a weight function[86], [87]. The stress intensity factor can be expressed as

$$K_I = \int_0^a h(x, a) \sigma(x) dx \quad , \quad (2.18)$$

where  $h(x, a)$  is the weight function. The weight function is determined from a reference stress intensity factor. For an edge crack, it is [86], [87]

$$h(x, a) = \frac{2}{\sqrt{\left(\pi a \left[1 - \left(\frac{x}{a}\right)^2\right]\right)}} \left[1.3 - 0.3 \left(\frac{x}{a}\right)^{\frac{5}{4}}\right] \quad . \quad (2.19)$$

Glinka and Shen also fit the weight function to a simpler form which can be expressed as [87]

$$h(x, a) = \frac{2}{\sqrt{2\pi(a-x)}} \left[1 + 0.5693 \left(1 - \frac{x}{a}\right) + 0.279375 \left(1 - \frac{x}{a}\right)^2\right] \quad . \quad (2.20)$$

Using numerical integration, the threshold strength values were  $\sigma_u=2.17$ , and 2.30 GPa for Specimens 3 and 4, respectively, as indicated in Table 2.3. The Weibull modulus  $m=4.83$  is taken to be the same for all specimens. The probability fits are seen in Fig. 2.12. The  $Q$  values are now 0.97, 0.96, 0.99 and 0.96, hence all are good fits. The  $L_{eff}$  values in Table 2.3 for Specimens 3 and 4 are smaller than those in Table 2.3. This reflects the larger  $\sigma_u$  values for those specimens.

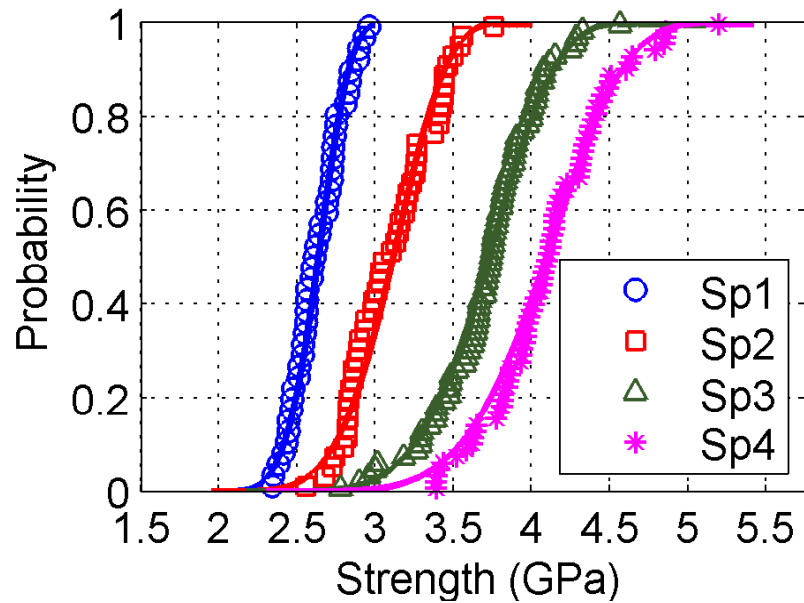


Fig. 2.12. Curve fitting of all strength data with Analysis Method 2 assuming a single value for  $m$  from Specimens 1 and 2, and by calculating values of  $r_u$  due to the stress gradient in Specimens 3 and 4.

Table 2.3 Analysis 2 - using Specimens 1 and 2 to make scaling predictions  $\sigma_u = 1.95$  GPa,  $\sigma_o = 2.47$  GPa.  $\mu\text{m}^{2/4.8}$  and  $m = 4.83$

Specimen ( $n$ , # tested)	$\sigma_u$ (GPa)	$\sigma_\theta + \sigma_u$ (GPa)	$cf / sdr^*$	$L_{\text{eff}}$ ( $\mu\text{m}$ )	% diff in $\sigma_\theta + \sigma_u$ (exp. vs. pred)	$Q$
1 (43)	1.95	2.69	0.83	140		0.97
2 (45)	1.95	3.19	0.33	14		0.96
3 (75)	2.17	3.81	0.012*	2.5	0.78	0.99
4 (74)	2.30	4.19	0.017*	1.4	0.83	0.96

While encouraging, further work is needed to understand the nature of the good agreement in Fig. 2.12 in detail. In particular, a power law function for the frequency distribution density of effective crack lengths  $g(a)$  does not necessarily predict a Weibull PDF in the presence of a

stress gradient, at least for the W2P case [83]. The good agreement in Fig. 2.12 also depends on assigning  $K_{Ic}=1.2 \text{ MPa}\cdot\sqrt{m}$ , a value that is at the upper range of careful measurements [60]. This choice can be justified in part because the flaws are due to sidewall grooves that are not through-cracks, but are more elliptical in nature. Also, the grooves are usually not aligned perpendicular to the load axis. Both of these considerations would reduce  $K$ , or effectively increase  $K_{Ic}$ . Finally, the native oxide on the surface may also increase the effective  $K_{Ic}$  value [88].

## 2.5 Analysis of Specimen 5

An even smaller Specimen 5 with a notch length of 4  $\mu\text{m}$  and notch radius of 0.5  $\mu\text{m}$  was also fabricated and tested. The experimental results (Appendix D, Fig D1) showed that the strength of Specimen 5 is similar to Specimen 4. Apparently there is an upper limit to the strength distribution and a high density of some small flaw size exists. Hence it appears that testing even smaller specimens will not increase the strength and will yield the same stress distribution. The Weibull distribution predicts an increase in strength as size decreases, but as shown in Section 2.2, this depends on a power law function for the flaw size distribution  $g(a)\sim a^{-n}$ . From this data it can be hypothesized that a new type of flaw has been introduced for small  $a$  with a higher density than that predicted by the power law function.

Another hypothesis is that an insufficient number of Sp 4 and Sp 5 specimens were tested to see the size effect. This hypothesis motivated the development of new Monte Carlo simulation to assess the effect of number of specimens on the strength distribution (Appendix J).

## 2.6-Summary and Conclusions

A new *in-situ* test platform has been developed to investigate the strength size effects in polysilicon. Compared to our previous platform [73], [74], it enables good alignment for all specimen sizes. A tradeoff is that residual stress is induced in the specimens. It was shown how the residual stress can be evaluated. It was also shown that with two different tensile specimens (here Specimens 1 and 2), the effective linewidth loss can be determined.

A W2P fit to Specimen 1 (the largest) predicted the characteristic strength of Specimens 2-4 unsatisfactorily. Two analyses were conducted to assess the ability of the W3P fits to predict strength size effects. In Analysis 1 using only Specimen 1, predictions remained unsatisfactory, as can be seen in Fig. 8 and by the goodness of fit values in Table 2.2 for DEN Specimens 3 and 4. This was attributed to the observation that the overlap in strength range of Specimen 1 with Specimens 3 and 4 is small. In Analysis 2, using both Specimens 1 and 2, the predictions improved, but were still unsatisfactory especially for Specimen 4, as seen in Fig. 2.10. With the recognition of a specimen-dependent  $\sigma_u$  due to stress gradient in the DEN specimens, a good prediction of Specimens 3 and 4 was obtained, as seen in Fig. 2.12.

## **Chapter 3: In-situ platform for isothermal testing of thin film mechanical properties using thermal actuators**

In Chapter 2, a specimen with a direct mechanical connection to the substrate was designed, analyzed and tested. Because the mechanical properties of ceramics such as polysilicon are only weakly dependent on temperature, and because near perfect alignment could be achieved with that design, the platform enabled good strength measurements. However, the melting temperature of Al is  $T_m=933$  K, much lower than silicon ( $T_m=1687$  K). The Peierls barrier is also much lower in FCC metals than in covalently bonded silicon. Therefore, Al mechanical properties such as strength are much more likely to be sensitive to temperature than is silicon. However, chevron actuators remain attractive because of the high force they generate. Therefore, we explored different methods to reduce the heat flow from the thermal actuator to the specimen.

Hence, in this chapter a new in-situ tensile test platform has been developed to study the mechanical properties of thin film metal specimens. The fully on-chip test platform loads a specimen using a thermal actuator. Thermal actuators conveniently provide high forces and excellent alignment, but generate large heat that can flow to specimens and raise their temperature. In the new design, heat flow to the specimen is negligible. This attribute was achieved by introducing a thermal resistor that limits heat flow to the specimen and a heat sink that shunts remaining heat. Residual stress in the specimen was eliminated by including newly designed pre-inserted microgrippers. An error analysis indicates that Young's modulus can be evaluated with  $\pm 21\%$  accuracy, while strength accuracy is  $\pm 5\%$  (both one standard deviation). The test platform was used to study strength-related mechanical properties of Al-0.5 wt% Cu

micro tensile bars with two different thicknesses. Initial tests indicate that 0.63- $\mu\text{m}$  thick tensile bars exhibit higher strength, a larger strain hardening coefficient and less elongation than 1.03- $\mu\text{m}$  thick tensile bars. Transmission electron microscopy indicated that the lower ductility was due to plastic strain localization.

### **3.1 Introduction**

Chevron TAs have emerged as robust and reliable on-chip actuators for applying large force and displacement. A current is applied through V shaped beams, resulting in Joule heating and expansion of the beams. This leads to rectilinear movement of the connected parts. The disadvantage of this technique is the large heat flow and high temperatures that the specimen may experience during testing, which can considerably alter the mechanical properties of some materials. This inherent problem with TAs limits their applicability to materials with properties that have a strong temperature dependence.

Several authors have tried to resolve the temperature issue for TAs. It was suggested to use a low thermal conductivity dielectric spacer, where a cut is made at required isolation points and a dielectric spacer is then deposited [45]. However, this approach requires additional fabrication steps and provides only limited thermal isolation. Others have used heat sink beams that emanate from the shuttle and are connected to the substrate [52]. The beam heat sinks should be short for effective heat dissipation. The disadvantage of this design is the small displacement range and the high force loss due to the fixed-fixed beams. Abbas et al. [89] used a test system consisting of a triple cascade of TAs capable of providing tens of mN force and tens of microns displacement while keeping temperature gradient low. The temperature difference across the sample was in the range of  $\Delta T = 30$  °C. However, their test system occupies a relatively large

area (more than  $2000\ \mu\text{m} \times 2000\ \mu\text{m}$ ), which make it less practical for testing large numbers of specimens in a given area.

Another problem that often arises for these testing techniques is the stress induced in the specimens, either because the specimen is connected to the substrate on both sides [43] or because the specimen is co-fabricated with the TA, which can induce large post-release stresses in the specimen [22]. This in turn can cause plastic deformation after releasing the chip.

In this work, a new in-situ test platform has been developed that provides (i) a small temperature difference across the specimen ( $<4\ ^\circ\text{C}$ ), (ii) a relatively large actuation force and displacement (2 to 8 mN and 10 to 20  $\mu\text{m}$ , respectively), (iii) actuator self-alignment, and (iv) fully stress-relieved specimens before loading. To devise this fully on-chip test platform, extensive considerations of thermal and structural issues have been tackled. A thermal resistor (TR)/heat sink combination was introduced to minimize the temperature gradient across the specimen. The thermal resistor minimizes heat flow, and a heat sink subsequently shunts virtually all the remaining heat away from the specimen. Moreover, the test platform eliminates the residual stress problem in the specimens by using pre-inserted microgrippers. Detailed information regarding the design, fabrication and validation of the test platform is included in the following sections.

Also, another test platform was developed where the specimen is connected directly to the TA, but due to the high residual stress induced to the specimen after release, this test platform was not pursued in this thesis. This test platform is shown in Appendix E

### 3.2 Test platform design considerations

The test platform was designed in the Sandia SUMMiT V<sup>TM</sup> microfabrication process [90]. The process consists of five polysilicon layers of which four are freestanding polycrystalline silicon (polysilicon) mechanical layers. The layers are denoted Poly0 to Poly4, where Poly0 is used for electrical interconnection and substrate attachment while Poly1-Poly4 are free standing mechanical layers. The Poly1 and Poly2 layers are usually connected to each other. Therefore, in practice the mechanical layers consist of three polysilicon layers, which are Poly1, Poly2 and Poly4. These layers are connected by sacrificial oxide (SO) cuts. The process contains the option of depositing Al-0.5% Cu metal on top of the Poly4 layer, thereby directly mounting the thin film to the test platform. (The Al-0.5% Cu film will be referred to as an Al film hereafter because the low Cu concentration does not play an important role in the film's mechanical properties [91]). The platform was also fabricated using the SUMMiT V<sup>TM</sup> process. However, special processing was done to span the Al film across two Poly4 regions. Namely, a fifth layer of sacrificial oxide (SO5) was deposited on top of Poly4. Then, the SO5 layer was polished back until it was at the same height as the Poly4. The Al film was directly deposited on top of this so that there was no vertical step from the polysilicon to the oxide. This sequence is described in more detail in ref. [91]. The samples were subsequently released [92] and rendered free standing by critical point drying.

The test platform as shown in Fig. 3.1 consists of a TA connected to a load cell that contains displacement and force gages. The load cell is connected to a thermal resistor, which is a long thin beam. The thermal resistor is made from one layer of polysilicon to increase its resistance to heat flow while promoting heat flow to the substrate. The thermal resistor is connected to a pre-

inserted microgripper, which allows the metal thin film to be freestanding while fully relieving its residual stress. One part of the gripping mechanism is connected to the thermal resistor while the other part is connected to the thin film, which is in turn connected to the substrate through an anchor pad. Table 3.1 summarizes the design parameters, which are discussed in detail next.

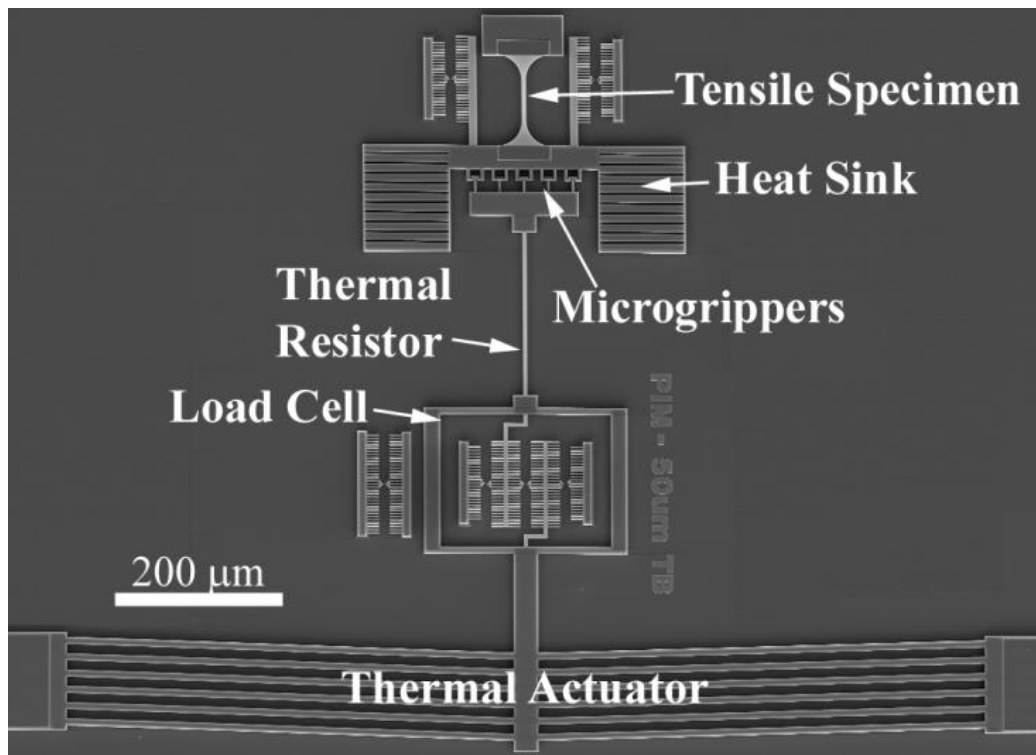


Fig 3.1 SEM image of the test platform

Table 3.1 Test Platform Design Parameters

Design Component	Parameter	Design Value
Thermal Actuator	Leg length	550 $\mu\text{m}$
	Offset angle	5°
	*Polysilicon layers	Poly 12, 3, 4
	Leg cross-sectional area (each)	75 $\mu\text{m}^2$
Load Cell	Spring length, $L_{LC}$	90 $\mu\text{m}$
	Spring width, $w_{LC}$	5 $\mu\text{m}$
	Spring thickness, $t_{LC}$	7 $\mu\text{m}$
	Stiffness, $k_{LC}$	1148 $\mu\text{N}/\mu\text{m}$
	Polysilicon layers	Poly 12, 3 & 4
Thermal Resistor/heat sink	Length of thermal resistor	200 $\mu\text{m}$
	Area of thermal resistor	11.25 $\mu\text{m}^2$
	Thermal resistor resistance, $R_{TR}$	63100 K/W
	Heat sink resistance, $R_{HS}$	6400 K/W
	Tensile specimen, $R_{TS}$	277300 K/W
Tensile specimen	Length, $L_{TS}$	50, 70, 200 $\mu\text{m}$
	**Width, $w_{TS}$	5 $\mu\text{m}$
	**Thickness, $t_{TS}$	0.7 $\mu\text{m}$

\*The TA legs are connected by SacOx3 and SacOx 4 cuts

\*\* Experimental values were  $w_{TS}$  =4.4  $\mu\text{m}$ , and  $t_{TS}$  =0.63  $\mu\text{m}$ , 1.03  $\mu\text{m}$

### 3.2-1 Thermal actuator

The two major parameters considered in the design of the thermal actuator (TA) were (i) the force output and (ii) the maximum displacement. The force output should be large enough to probe the thin film strength, while the maximum displacement should be large enough to map the full plastic strain response of thin film. Optimization of the TA dimensions was carried out using a previously-developed MATLAB-ANSYS coupled model, which has been described in detail [93]. Briefly, the model consists of two solvers: electro-thermal analysis performed in MATLAB and thermal-structural analysis performed in ANSYS. A MATLAB finite difference formulation is used to determine the TA leg temperature profile, and the data is imported into ANSYS for finite element solution of the structural force and displacement. In-plane buckling of the TA legs

due to eccentric compressive load, which decreases the force output, is also included in the model.

The final TA design consists of six leg pairs. Each leg has a length of  $550\ \mu\text{m}$  and makes an angle of  $5^\circ$  from the horizontal. Bulk nanograined aluminum tensile bars with 30% elongation before fracture have been reported [94], while thin film aluminum tensile bars exhibited up to 4% [20] and even 30% elongation when a large number of samples were tested [21]. The TA was conservatively designed to provide 30% elongation for  $50\ \mu\text{m}$  long tensile bars of  $5\ \mu\text{m}$  width. The corresponding leg temperature was  $600\ ^\circ\text{C}$  at an applied voltage of 11.5 V. Fig. 3.2(a) shows the force-displacement curve for the TA at different voltages. The load line for a  $50\text{-}\mu\text{m}$  long tensile specimen is also displayed (this line includes the stiffness of the load spring). The tensile specimen is assumed to have a width of  $5\ \mu\text{m}$  and thickness of  $0.7\ \mu\text{m}$ . Two load lines for the  $50\text{-}\mu\text{m}$  long tensile specimen are shown. The horizontal load line corresponds to yield at 200 MPa with perfect plasticity. This was taken to be our baseline design. The second load line shown corresponds to brittle fracture, as has been observed in 200 and 50 nm thick Al films [49], [95]. The actuator is capable of producing a displacement of up to  $18\ \mu\text{m}$  and maximum force of about  $9000\ \mu\text{N}$ , which was believed to be sufficient to fracture the tensile specimens. Fig. 2(b) indicates the maximum leg and shuttle temperature at each voltage. The shuttle temperature can reach about  $250\ ^\circ\text{C}$ , and therefore heat can leak to the specimen. This issue will be addressed in Section 3.2-3. The TA design parameter values are summarized in Table 3.1.

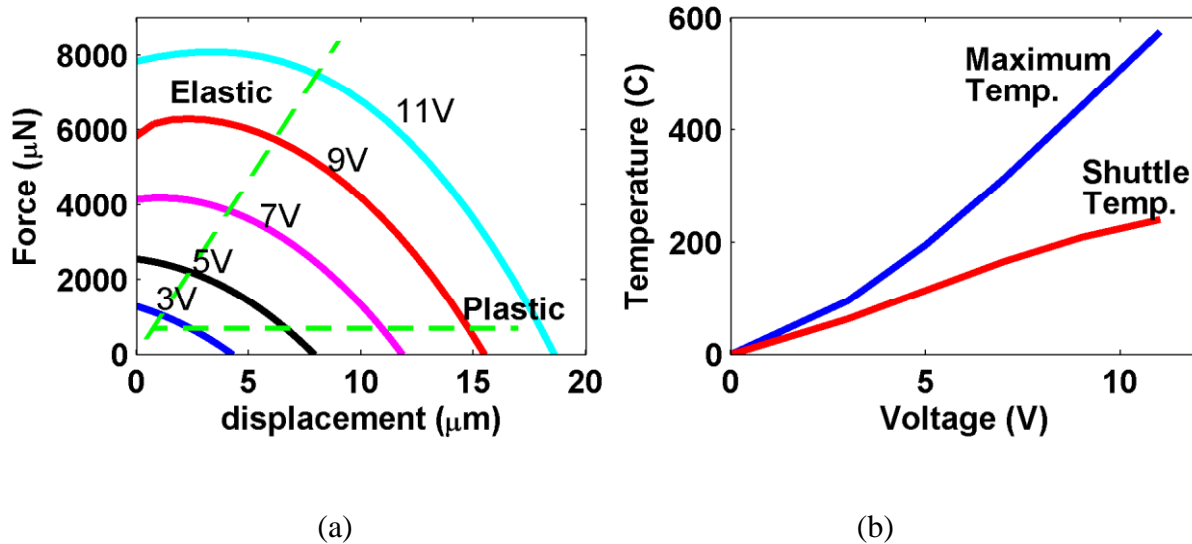


Fig. 3.2 (a) Calculated TA force-displacement curves (solid lines) with elastic and elastic-plastic load lines (dashed) (b) calculated temperature of legs and central shuttle versus TA voltage

### 3.2-2 Load cell

The load cell, as shown in Fig. 3.3, consists of a load spring (comprised of four fixed-guided beams) and two displacement gages. One gage is connected to the crosshead through the thermal resistor, and measures the combined displacement of the tensile specimen and components in series with it. Determination of the specimen displacement is detailed in Section 3.3-2. The other gage spans the load spring; force  $F$  is determined by multiplying its reading by the calculated load spring constant. To eliminate the effect of sample drift, each grating is referenced to a grating connected to the substrate, as seen on the far left and far right side of the gage structure.

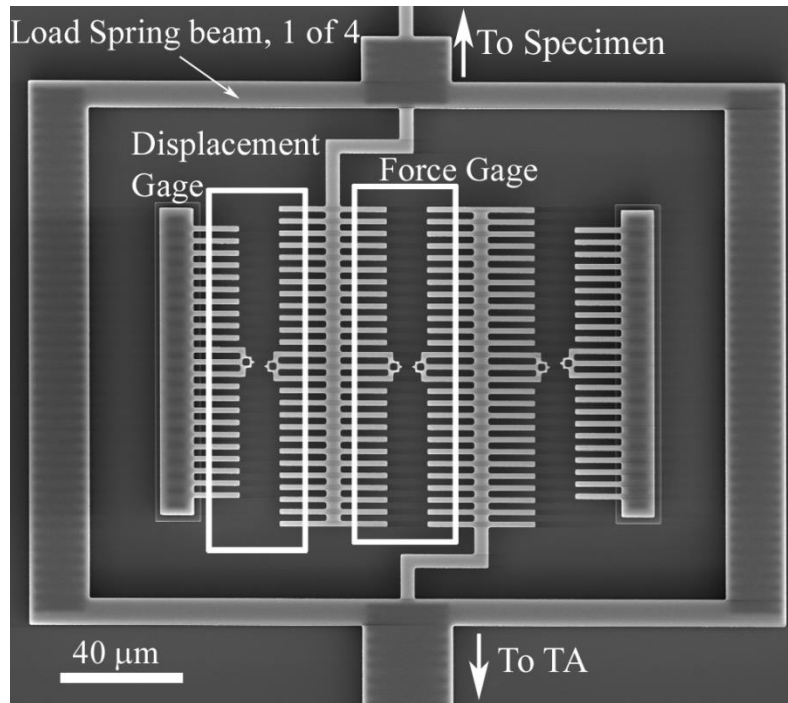


Fig. 3.3 Load cell including displacement and force gages.

The important consideration in designing the load spring is to make it sufficiently compliant for good force resolution, but stiff enough that high force is still transferred to the tensile specimen. The tensile specimen elastic stiffness is  $k_{TS} = E_{TS} A_{TS} / L_{TS}$ , where  $E_{TS}$ ,  $A_{TS}$  and  $L_{TS}$  are the tensile specimen Young's modulus, cross sectional area and length, respectively. Assuming  $E = 70$  GPa,  $A_{TS} = 5 \cdot 0.7 \mu\text{m}^2$ , and  $L_{TS} = 50 \mu\text{m}$ ,  $k_{TS} = 4900 \mu\text{N}/\mu\text{m}$ . The load cell was chosen to have a smaller stiffness of  $k_{LC} = 1148 \mu\text{N}/\mu\text{m}$ , as shown in Table 3.1. This choice was made in order to obtain good force resolution in the elastic regime of the specimen, while still being able to gain information over a significant portion of the plastic strain range.

### 3.2-3 Thermal resistor and heat sink configuration

Mechanical properties of metals, such as yield stress, residual stress, creep, and fatigue, depend strongly on temperature. Therefore, attaining a nearly isothermal specimen test is critical. The end of the tensile specimen connected to the substrate will be at ambient temperature. Hence, the other end should be as close to ambient temperature as possible. Some of the heat generated in the TA will transfer through the surrounding gaseous air medium to the substrate so that it does not reach the specimen. However, the thermal conductivity of air is approximately three decades lower than the thermal conductivity of polysilicon, as shown in Fig. 3.4. Therefore the polysilicon acts nearly as a perfect conductor and appreciable heat may reach the specimen. To minimize this effect, we designed a thermal resistor that connects between the load cell and the grippers. The relatively long thin thermal resistor beam, made from a single layer of polysilicon, minimizes heat flow and increases heat escape through the surrounding air to the substrate. We attached a large heat sink to the crosshead to shunt the remaining heat to the substrate. Fig. 3.5 shows a simplified thermal resistor circuit, where the subscripts TR, HS and TS and AMB stand for thermal resistor, heat sink, tensile specimen and ambient respectively.  $R_{AMB}$  represents the important lumped thermal resistance from  $R_{TR}$  through the ambient to the substrate. The temperatures  $T_1$  and  $T_2$  are that of the TA shuttle and the specimen crosshead, respectively.

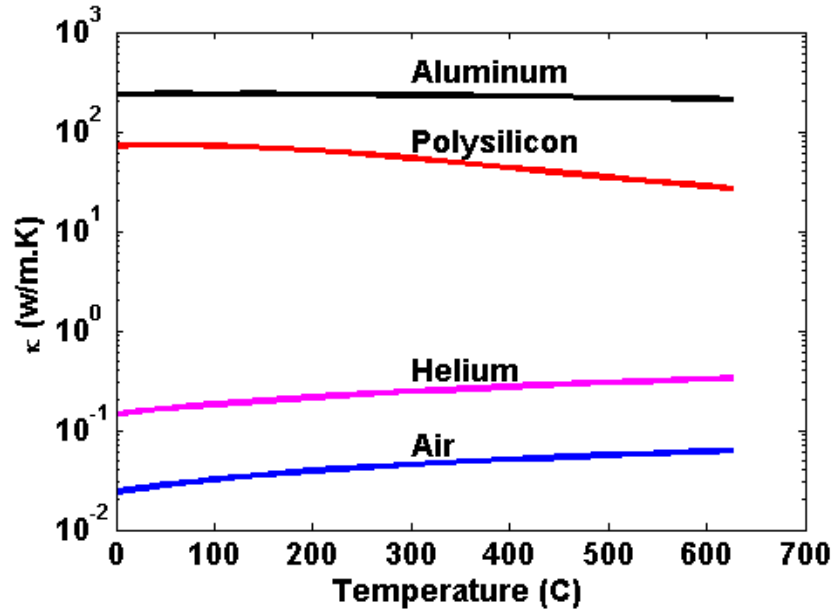


Fig. 3.4 Thermal conductivity versus temperature for different materials

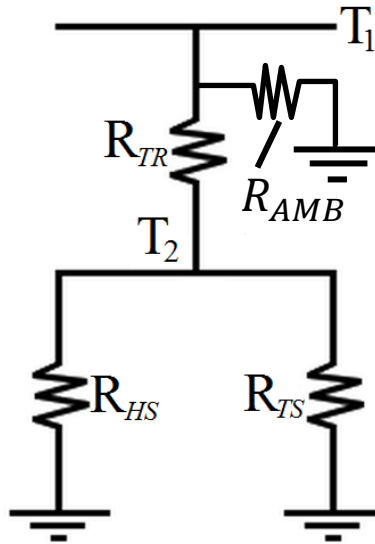


Fig. 3.5 Simplified thermal circuit of thermal resistance, heat sink, tensile specimen configuration.  $R_{TR}$  - thermal resistor resistance,  $R_{HS}$  - heat sink resistance,  $R_{TS}$  - tensile specimen resistance,  $R_{AMB}$  - lumped resistance thru the ambient.

From Fourier's Law for one-dimensional thermal conduction, the thermal resistance can be expressed as

$$R = \frac{l}{\kappa A} \quad , \quad (3.1)$$

where  $l$  is length,  $\kappa$  is thermal conductivity and  $A$  is the cross-sectional area.

Estimates for the thermal resistances are  $R_{TR}=63100$  K/W,  $R_{HS}=6400$  K/W, and  $R_{TS}=277300$  K/W, as also listed in Table 3.1. The resistor  $R_{HS}$  can be made arbitrarily low by making its area large. A small gap of  $2 \mu\text{m}$  between the heat sink and substrate, as defined by the SO1 layer thickness in the SUMMiT V<sup>TM</sup> process, minimizes  $R_{HS}$  (note that the gap now acts as the length in equation (3.1)). With an area of  $12,000 \mu\text{m}^2$ ,  $R_{HS}$  is just 2.3% of  $R_{TS}$ , and therefore the major portion of the heat flow is through the heat sink rather than the tensile specimen. Assuming that the substrate is at  $25 \text{ }^\circ\text{C}$  and  $T_1=250 \text{ }^\circ\text{C}$  (the maximum possible with 11 V applied to the TA), a first order calculation ignoring  $R_{AMB}$  shows that  $T_2$ , which is located at the tensile specimen cross-head, is  $21 \text{ }^\circ\text{C}$  higher than the surrounding temperature.

One approach to reduce  $T_2$  further would be to conduct the testing in He, which will decrease  $R_{AMB}$  and hence increase heat loss to the substrate before it reaches the crosshead. As seen in Fig.3.4,  $\kappa_{He}$  is approximately 10 times higher than  $\kappa_{air}$ . However, even in air, the above first order result significantly overestimates  $T_2$  because it neglects  $R_{AMB}$ . To get an accurate estimate of  $T_2$ , a three-dimensional multi-physics model of the test platform was developed in ANSYS. A voltage is applied across the TA legs in the model and temperature results are extracted. The model is detailed in Appendix F. With  $T_1=250 \text{ }^\circ\text{C}$  (corresponding to TA voltage of 11 V), the temperature difference along the tensile specimen is determined from the model is  $4 \text{ }^\circ\text{C}$ , thus

approaching an isothermal test condition. In fact, the temperature difference across the tensile specimen is likely even smaller because the microgrippers provide an extra thermal resistance in the form of contact resistance, which contributes an extra resistance in series with the thermal resistor  $R_{TR}$  (Fig. 3.5). Its value is not well known and was not included in the finite element model. As will be seen below, the TA voltage was well below 11 V in the experiments, which further reduced the temperature difference along the sample.

### **3.2-4 Pre-inserted microgrippers**

The grippers, as shown in Fig. 3.6, consist of two components: (i) load-carrying grippers and (ii) constraining grippers. As seen in Fig. 3.6(a), there are three load-carrying grippers and two constraining grippers. Each is made from three polysilicon layers that are connected through sacrificial oxide layer cuts, as indicated in the cross-section schematic of Fig. 3.6(b) marked as AA. One end is connected to the thermal resistor while the other is connected to the crosshead. The load-carrying grippers initially are freestanding. As actuator displacement increases to  $\sim 1 \mu\text{m}$ , they make contact and apply tensile load.

The constraining grippers are also seen in Fig. 3.6(a). The fabrication process may induce residual stress gradients in the metal thin film, which will cause the film to bend up or down after release. If the bending were severe, then the load-carrying grippers would not engage. Therefore, the constraining gripper part connected to the crosshead surrounds the part connected to the thermal resistor, as indicated in the cross-section schematic of Fig. 3.6(b) marked as BB. The constraining grippers also inhibit slippage and optimize engagement of the load-carrying grippers during testing.

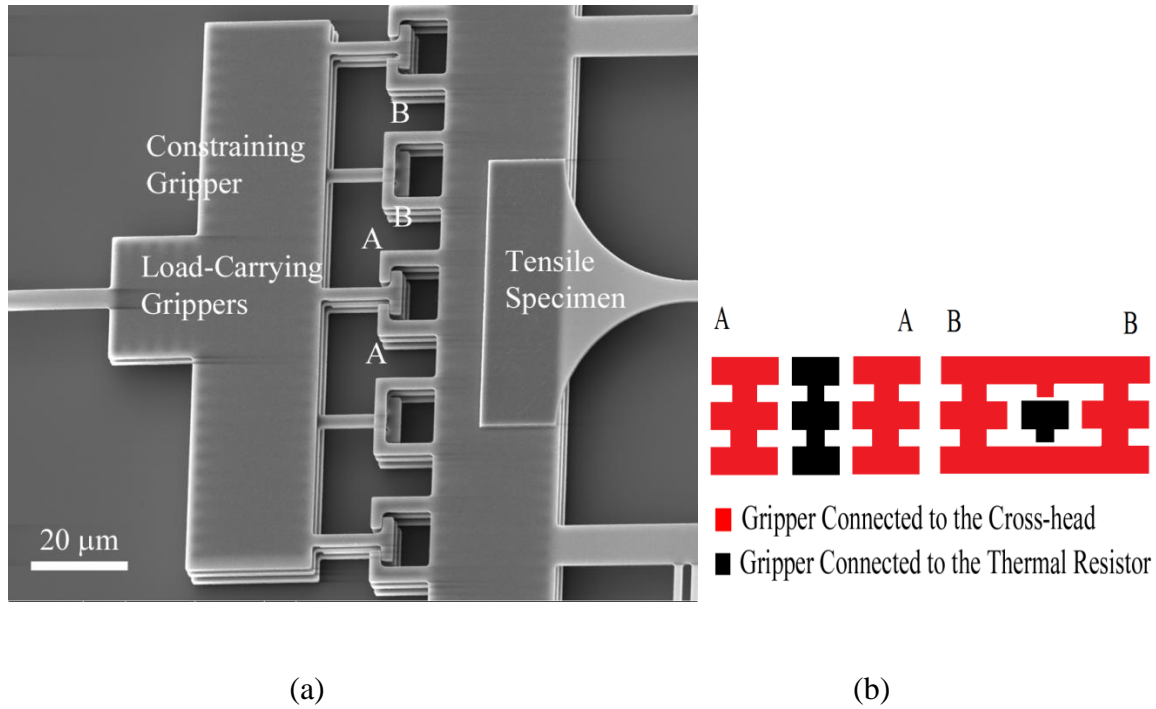


Fig. 3.6 The microgrippers (a) an SEM tilt view shows the load -carrying grippers and out-of-plane constraint grippers (b) gripper schematic cross-sections

### 3.3 Experimental

#### 3.3-1 Thin film tensile specimens tested

To assess the effectiveness of the new test platform, we tested several Al thin film tensile bars with variations in length  $L_{TS}$  and thickness  $t_{TS}$ . The design width of the samples was  $7 \mu\text{m}$ , but after wet etch their width was  $w_{TS}=4.4 \mu\text{m}$ . The lengths were  $L_{TS}=50, 70$  and  $200 \mu\text{m}$ . The standard aluminum film thickness in the SUMMiT V is  $0.7 \mu\text{m}$  and a thicker film of  $1.1 \mu\text{m}$  was also processed. The films were sputter-deposited at  $175 \text{ }^\circ\text{C}$  for 42 and 66 s to attain the two film thicknesses, and after etch the photoresist was removed by plasma ashing at  $250 \text{ }^\circ\text{C}$  for  $\sim 3$  min. The thickness values of  $0.63 \mu\text{m}$  and  $1.03 \mu\text{m}$  include  $0.07 \mu\text{m}$  removed by the sacrificial oxide

release etch [92]. These thicknesses were measured by running a profilometer over the end of freestanding cantilevers that were pressed down to the substrate by its normal force, and the estimated thickness uncertainty is  $\pm 0.03 \mu\text{m}$  (one standard deviation). Fig. 3.7 shows an  $L_{TS}=70 \mu\text{m}$  specimen with  $t_{TS}=1.03 \mu\text{m}$ . As measured by the ASTM standard [96], the grain sizes were  $3.6 \mu\text{m}$  and  $4.8 \mu\text{m}$  for the  $t_{TS}=0.63$  and  $1.03 \mu\text{m}$  films, respectively. From electron-backscatter diffraction (EBSD) measurements using a FEI Quanta 600 scanning electron microscope and Oxford Instruments EBSD system, Al films were predominantly oriented with the  $\langle 111 \rangle$  direction aligned normal to the substrate and randomly along the loading direction.

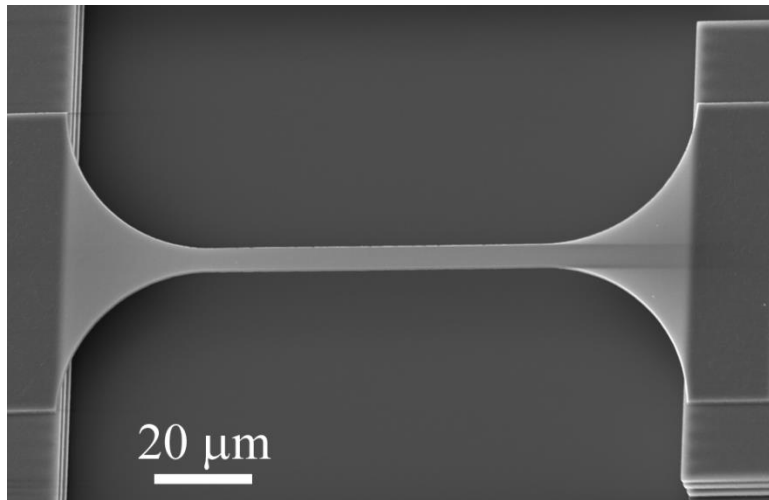


Fig. 3.7  $70 \mu\text{m}$  long tensile specimen

### 3.3-2 Mechanical Testing

The experimentation was performed in laboratory air at  $25 \text{ }^\circ\text{C}$  on an optometric probe station equipped with a long-working distance interferometer [97]. The entire test set up rests on a Minus-K 250 BM-1 vibration isolation base. Automated measurement scripts were written using MEMScript software developed at Sandia National Labs, which utilizes the image processing

algorithms within National Instruments' Vision Acquisition application. Voltage was applied across the TA in steps of 0.02 V using Signatone SE-T probes. The grippers engaged, and force and displacement were optically monitored in load cell gages using a 50 X objective lens (NA=0.55). The load spring gage displacements were calculated by detecting the phase difference between reference and object gratings in real time. Given that TA displacement is not linear with voltage, the strain rate was not controlled. However, the average strain rate was on the order of  $2 \cdot 10^{-4}$ /s. In-plane displacement change resolution was  $\pm 7$  nm (one sigma), yielding a force resolution of approximately  $\pm 8$   $\mu$ N (one sigma).

### 3.3-3 Data Analysis

The displacement data  $\delta_T$  collected at the load spring is the sum of contributions due to (i) the tensile bar gauge section and (ii) the complementary components, which are comprised of the thermal resistor, the grippers and the fillet regions. They form a combined spring system. A graphical approach was applied to estimate  $E_{TS}$  and the displacement of the tensile specimen gauge section. The combined system can be modeled as two springs in series with a total stiffness  $k_T$ . Thus,

$$\frac{1}{k_T} = \frac{1}{k_c} + \frac{1}{k_{TS}} \quad (3.2)$$

where  $k_{TS}$  is the stiffness of tensile specimen. The stiffness of the complementary components  $k_c$  is assumed to be the same in each design. The stiffness of the tensile specimen in the elastic region can be expressed as

$$k_{TS} = E_{TS} \frac{A_{TS}}{L_{TS}} \quad (3.3)$$

Substituting equation (3.3) into (3.2)

$$\frac{1}{k_T} = \frac{1}{k_c} + \frac{1}{E_{TS}A_{TS}} L_{TS} \quad (3.4)$$

To determine  $E_{TS}$  and  $k_c$ , a plot of  $1/k_T$  versus  $L_{TS}$  is constructed. Then, a linear curve fit is performed where the slope of the fitted line is  $(1/E_{TS}A_{TS})$  and the  $y$ -intercept is  $1/k_c$ . Then, the tensile specimen displacement can be obtained as

$$\delta_{TS} = \delta_T - \frac{F}{k_c} \quad , \quad (3.5)$$

where  $\delta_{TS}$  is the specimen displacement and  $F=k_{LC}\delta_T$ . We observe that  $k_{TS}$  changes due to plastic strain, but  $k_c$  does not. Therefore, equation (3.4) is used in the elastic realm of the tensile specimen to determine  $E_{TS}$  and  $k_c$ . Then equation (3.5) is used for the elastic and plastic zones to determine  $\delta_{TS}$  where  $F/k_c=\delta_c$  is the displacement of the complementary components.

### 3.3-4 Transmission electron microscopy

After mechanical testing, some samples were lifted out directly from the test platform using the focused ion beam (FIB) technique [98]. A FEI Nova Nanolab FIB was used to ion mill the specimens free from the platform. A 20 keV Ga<sup>+</sup> ion beam was used for imaging and milling the specimen without any ion beam exposure to the tensile bar or fracture region. The samples were extracted using an Omniprobe Nanomanipulator inside the FIB and mounted on to conventional copper grids. They were imaged in an FEI Tecnai F20 transmission electron microscope (TEM) at 200 keV. Two imaging modes were utilized: convention bright-field (BF) TEM imaging and scanning TEM (STEM) using a high angle annular dark field (HAADF) detector for dark-field imaging. Both BF-TEM and STEM-HAADF imaging modes allow direct observation of

dislocations in the metal layers. All TEM images were recorded in regions free of any ion milling and associated damage.

### 3.4 Results and Discussion

Preliminary tension tests were performed on samples with lengths of  $L_{TS}=50, 70$  and  $200 \mu\text{m}$  for Al-0.5 wt. % Cu films with  $t_{TS}=0.63$  and  $1.03 \mu\text{m}$ . Force and displacement were recorded during the test. The engineering stress and strain were determined from the simple relations  $\sigma = F/A_{TS}$  and  $\varepsilon = \delta_{TS}/L_{TS}$  where  $\sigma$  and  $\varepsilon$  are the engineering stress, respectively. Table 3.2 summarizes the test results, which are described next. The total stiffnesses  $k_T$  of the three tensile specimens were determined by fitting the linear part of the load spring force-displacement curve. Then the inverses of the stiffness values were plotted versus  $L_{TS}$ , as shown in Fig. 3.8. The slope of the curve fit was used to determine  $E = 85$  and  $89 \text{ GPa}$  for the  $0.63$  and  $1.03 \mu\text{m}$  thick tensile specimens respectively. Extrapolating the lines to a length  $L=0$ , the average of intercept value is  $1/k_c=5.7 \cdot 10^{-5} \mu\text{m}/\mu\text{N}$ , or  $k_c=1.75 \cdot 10^4 \mu\text{N}/\mu\text{m}$ .

Stress-strain curves were extracted directly from the  $F$  versus  $\delta_{TS}$  data and are shown in Fig. 3.9 for the  $L_{TS}=200, 70$  and  $50 \mu\text{m}$  specimens. The maximum voltages applied to the  $0.63$  and  $1.03 \mu\text{m}$  thick samples were  $3.2$  and  $5 \text{ V}$ , respectively. From these voltages, maximum shuttle temperatures of  $68 \text{ }^\circ\text{C}$  and  $114 \text{ }^\circ\text{C}$  are calculated. Given the thermal resistor/shunt design, the temperature gradient is expected to be  $2 \text{ }^\circ\text{C}$  and  $3 \text{ }^\circ\text{C}$  for these tests, respectively. Curvature can be noted at small strains in some of the  $\sigma$  versus  $\varepsilon$  data. This is believed to be due to a gradual gripper engagement process. The same curvature was of course also seen in the force displacement curves that were used to estimate the  $E_{TS}$  values reported above. Therefore, the  $k_T$

values were estimated only once the data was linear, corresponding to full engagement of the grippers.

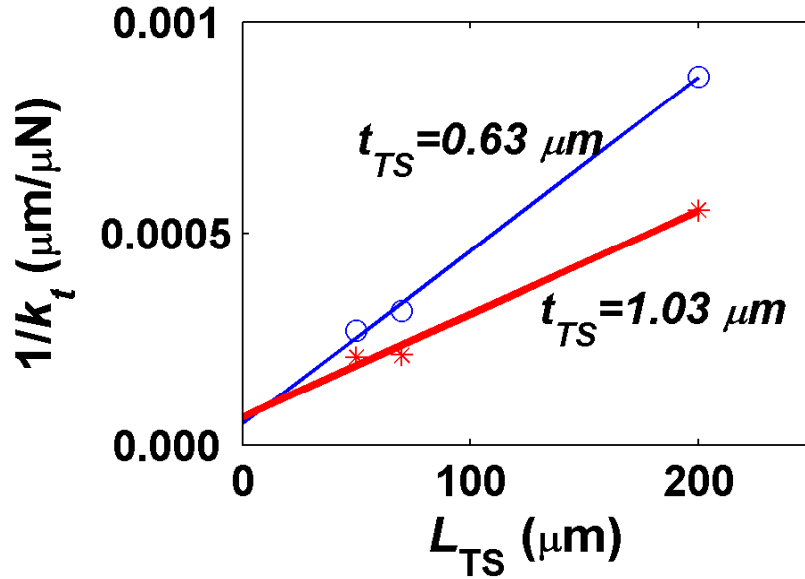


Fig. 3.8 The inverse of stiffness vs. specimen length for different tensile bars

Table 3.2 Summary of test results

Property or Attribute	$t=0.63 \mu\text{m}$	$t=1.03 \mu\text{m}$
$E_{TS}$ (GPa)	$85 \pm 15.6$	$89 \pm 15.6$
$\sigma_y$ (MPa) ( $L=200, 70, 50 \mu\text{m}$ )	225, 305, 358	153, 215, 230
$\epsilon_f$ (%) ( $L=200, 70, 50 \mu\text{m}$ )	1.35, 1.3, 1.4	1.9, 1.5, 4.6
$n$	0.46	0.27
Max $\Delta T$	2 °C	3 °C
Max bending/tensile stress ratio	$\leq 1.5 \%$	$\leq 1.5 \%$

The expected value for  $E_{TS}$  is 74.4 GPa [91]. A detailed error analysis of  $\sigma$ ,  $\epsilon$  and  $E_{TS}$  is reported in Appendix G. The uncertainty in  $E_{TS}$  of  $\pm 15.6$  GPa (one standard deviation) is attributed

mainly to the uncertainties in  $\delta_T$  and  $t_{TS}$  (as reported in Table G1). The error due to  $\delta_T$  dominates at low strain (up to 0.08%), while the error due to uncertainty  $t_{TS}$  dominates in the strain range  $\varepsilon = 0.08\text{-}0.3\%$ . Figs. G1 and G2 in Appendix G reveal these trends. The uncertainty in  $E_{TS} = \pm 15.6$  GPa is due to the combination of the uncertainties detailed in Appendix G and the steep slope in the linear region of the stress-strain curve.

With respect to plastic deformation, it should be noted that the  $L_{TS} = 200 \mu\text{m}$ ,  $t_{TS} = 0.63 \mu\text{m}$  tensile bar in Fig. 3.9a exhibits an apparent strong strain softening characteristic. That is, there is a large drop in the load just beyond  $\sigma_y$ . This is due to an instability in the load frame. That is, the load cell stores significant strain energy that will be released if the tensile bar cannot sustain the force that it exerts. The load frame is neither fixed load nor fixed grip. A fixed grip system would likely exhibit a less severe softening.

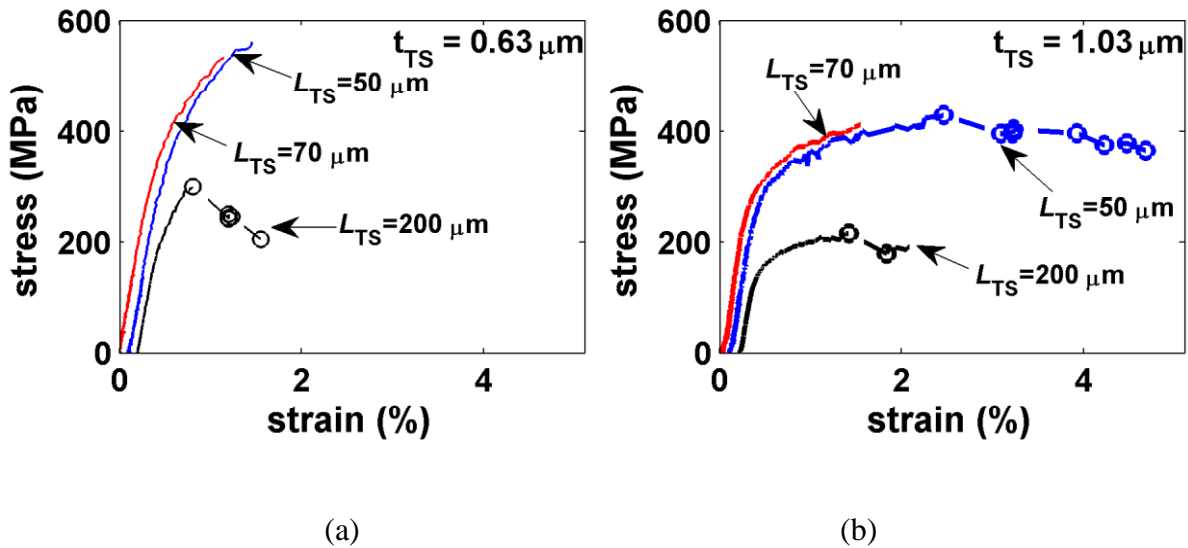


Fig. 3.9 Stress versus strain curves up to fracture (dashed lines indicate instability-induced displacements). Data are offset by a strain of 0.1% to make each curve distinguishable

The yield stress  $\sigma_y$  is taken as the value of strength that deviates from linearity by three times the noise in the measurement (this will give a significantly lower estimate than the typical 0.2% offset, but is used because most microscale applications will not tolerate plastic deformation). For the  $t_{TS}=0.63 \mu\text{m}$  thick specimens, the values of  $\sigma_y$  are 225, 305 and 358 MPa for  $L_{TS}=200$ , 70 and 50  $\mu\text{m}$  tensile bars, respectively. For the 1.03  $\mu\text{m}$  thick specimens, the values of  $\sigma_y$  are 153, 215 and 230 MPa for  $L_{TS}=200$ , 70 and 50  $\mu\text{m}$  tensile bars, respectively. As shown in Appendix B, the error in the  $\sigma_y$  values is not more than 5%. Therefore, the differences are significant. It is apparent that shorter  $L_{TS}$  and lesser  $t_{TS}$  both increase  $\sigma_y$ .

For  $t_{TS}=0.63 \mu\text{m}$ , the elongation was  $\varepsilon_f=1.35\%$  ( $L_{TS}=200 \mu\text{m}$ ),  $\varepsilon_f=1.3\%$  ( $L_{TS}=70 \mu\text{m}$ ), and  $\varepsilon_f=1.4\%$  ( $L_{TS}=50 \mu\text{m}$ ). For the  $t_{TS}=1.03 \mu\text{m}$ ,  $\varepsilon_f=1.9\%$  ( $L_{TS}=200 \mu\text{m}$ ),  $\varepsilon_f=1.5\%$  ( $L_{TS}=70 \mu\text{m}$ ), and  $\varepsilon_f=4.6\%$  ( $L_{TS}=50 \mu\text{m}$ ). The  $t_{TS}=0.63 \mu\text{m}$  specimens exhibit significant strain hardening, with a strain hardening exponent  $n=0.46$  for  $\sigma>\sigma_y$  while the  $t_{TS}=1.03 \mu\text{m}$  specimens exhibit less strain hardening with  $n=0.27$  for  $\sigma>\sigma_y$  up to the plastic instability.

One important test artifact relates to the magnitude of the bending moment applied to the tensile specimens. Their placement on top of the polysilicon layers will lead to some off-axis loading. To quantify this effect, the out-of-plane deflection curves of tensile specimens were measured at different TA voltages using phase-shifting interferometry. Fig. 3.10 shows the out-of plane displacement of the 70- $\mu\text{m}$  long tensile specimen at different voltages. At 0 V, the constraining grippers act to reduce the out-of-plane deflection and prevent disengagement. Then, the tensile specimen curves upward by about 0.5  $\mu\text{m}$ . As the voltage is increased, the tensile specimen starts to bend downward to about -0.5  $\mu\text{m}$  at 3 V. The maximum curvature occurs at  $x\approx 100 \mu\text{m}$ . There, the bending to axial stress ratio is found to be 0.015, a relatively small value.

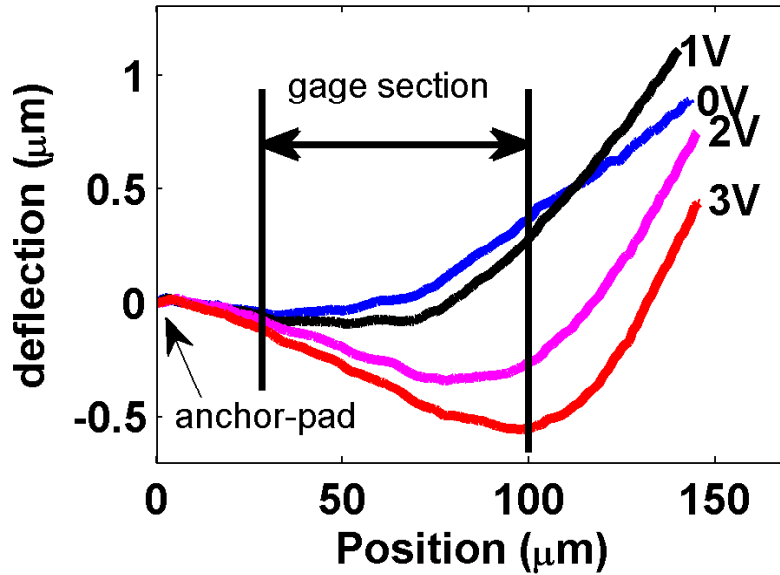


Fig. 3.10 Out-of-plane deflection versus TA voltage for  $L_{TS} = 70 \mu m$  sample.

High  $\sigma_y$  and low  $\varepsilon_f$  in free-standing aluminum thin specimens at room temperature were also observed by Lee et al. [20], Haque et al. [95], and Espinosa et al. [49]. Lee et al. [20] studied 2- $\mu m$  thick sputtered Al specimens (500- $\mu m$  long and 50- $\mu m$  wide) at different annealing temperatures and found that  $\sigma_y$  decreased from 125 MPa for as-deposited specimens ( $d=1.1 \mu m$ ) to 92 MPa for specimens annealed at 450 °C ( $d=2.3 \mu m$ ). In contrast,  $\varepsilon_f$  increased from 0.7% for as-deposited specimens to about 4% for specimens annealed at 450 °C. Strain softening immediately after yield was observed except for the specimen annealed at 450 °C, which experienced strain hardening to a small degree. They attributed the greater elongation and softening in the larger grained films to a local grain thinning effect, in which dislocations in the grain centers were more likely to intersect the free surface than the grain boundaries.

Espinosa et al. [49] tested evaporated aluminum specimens with widths of 5, 10 and 20  $\mu\text{m}$  and thicknesses of 0.2 and 1  $\mu\text{m}$ . No clear strength size effect was observed with respect to specimen width, but a significant size effect occurred with thickness. They measured  $\sigma_y \approx 375$  MPa and  $\epsilon_f \approx 0.4\%$  for 0.2  $\mu\text{m}$  thick specimens and  $\sigma_y \approx 150$  MPa for 1  $\mu\text{m}$  thick specimens and  $\epsilon_f$  of 2.5%-7%. They defined  $\sigma_y$  as the value of stress when the slope deviates from linearity.

While the above comparisons are of interest, single values of strength and ductility may not exist at this scale because of a strong dependence on individual grains. That is, in bulk specimens, weak grains may yield first, but surrounding grains of different orientation will prevent strain softening. Indeed, for thin film samples tested in HF acid (i.e., no native oxide was present), a Weibull-like distribution of ductility has been observed [21]. Quantifying the strength range for different length and thickness specimens *in air* is an important topic for future work.

To gain initial insight into our  $\epsilon_f$  values, we conducted transmission electron microscopy (TEM) of the samples strained to fracture in order to investigate the difference in how strain was accommodated. The  $L_{TS}=50$   $\mu\text{m}/t_{TS}=1.03$   $\mu\text{m}$  with large ( $\epsilon_f=4.6\%$ ) and the  $L_{TS}=50$   $\mu\text{m}/t_{TS}=0.63$   $\mu\text{m}$  with small ( $\epsilon_f=1.4\%$ ) ductility from Fig. 3.9 were directly lifted out using FIB. Three regions were identified according to their proximity to the fracture zone. As shown in Fig. 3.11, Region 1 is in the immediate vicinity of the fracture zone, Region 2 is about 10  $\mu\text{m}$  away, while Region 3 is about 17  $\mu\text{m}$  away.

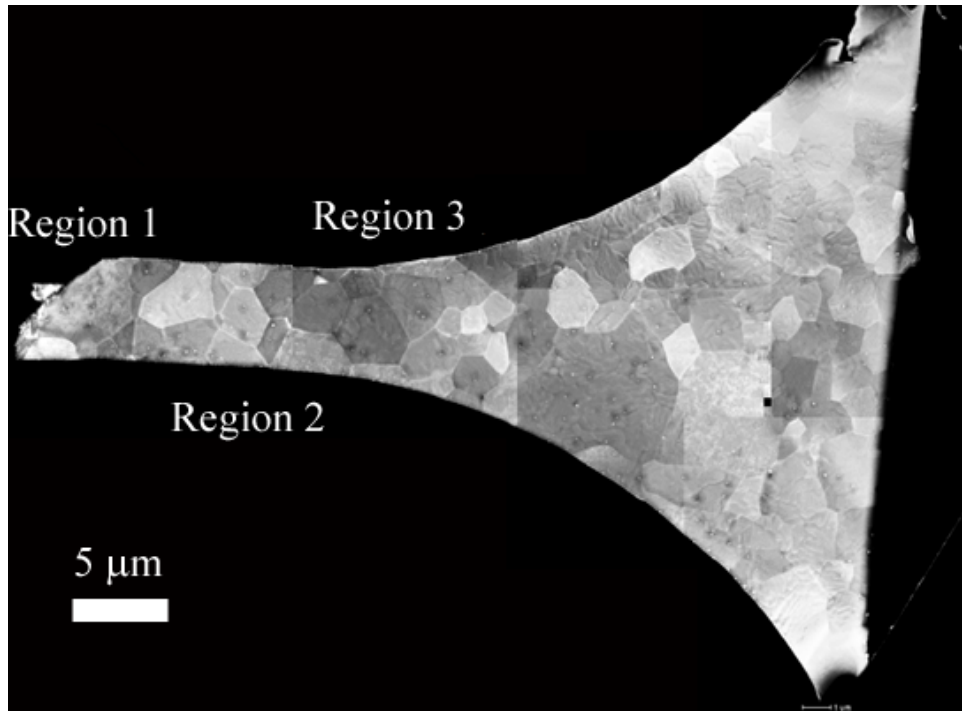


Fig. 3.11 TEM composite image shows the regions of study

BF-TEM and STEM-HAADF analysis was utilized to image the microstructure and investigate dislocation distribution. For the 0.63  $\mu\text{m}$  tensile bar, we observe a large dislocation density in Region 1 ( $\sim 100 \times 10^8 \text{ cm}^{-2}$ ). The dislocation density diminishes significantly in Regions 2 and 3 ( $\sim 10 \times 10^8 \text{ cm}^{-2}$ ), as shown in Fig. 3.12. This indicates that local plasticity is responsible for the limited ductility. In contrast, the dislocation density is high in Regions 1, 2 and 3 of the 1.03  $\mu\text{m}$  tensile specimen as shown in Fig. 3.13 (dislocation density was  $> 140 \times 10^8 \text{ cm}^{-2}$  in Region 1 and  $\sim 40 \times 10^8 \text{ cm}^{-2}$  in Regions 2 and 3). This indicates that the plastic deformation occurs more uniformly throughout the tensile specimen, which therefore increases the elongation.

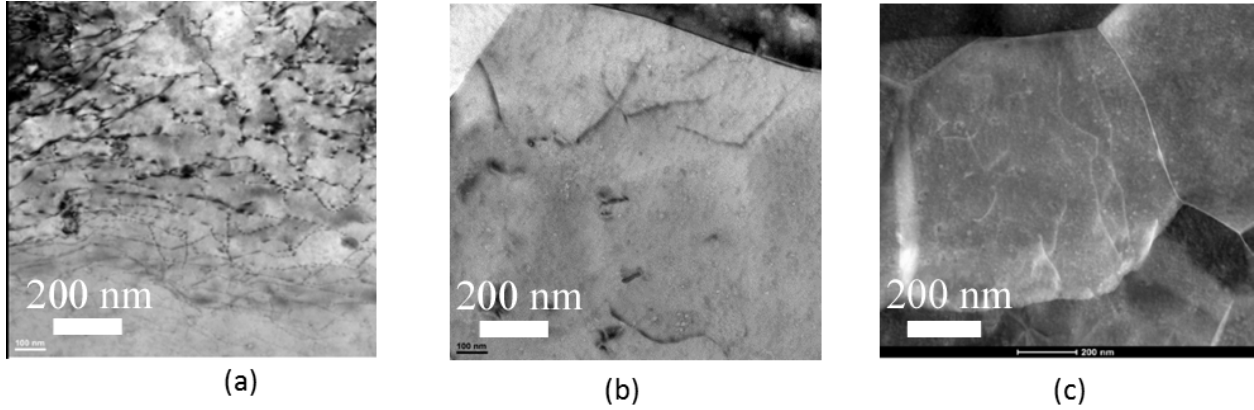


Fig. 3.12 TEM images for  $L_{TS}=50 \mu\text{m}$ ,  $t_{TS}=0.63 \mu\text{m}$ . (a) Region 1, (b) Region 2 and (c) Region 3.

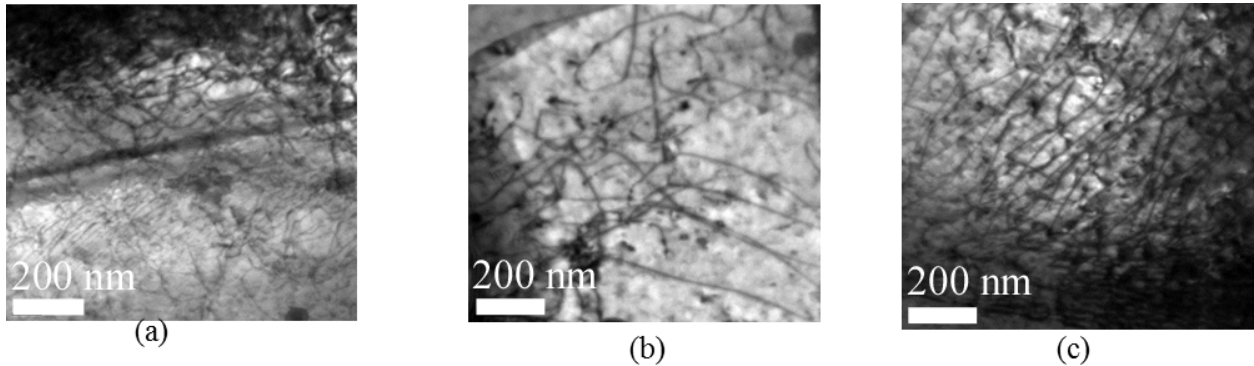


Fig. 3.13 TEM images for  $L_{TS}=50 \mu\text{m}$ ,  $t_{TS}=1.03 \mu\text{m}$ . (a) Region 1, (b) Region 2 and (c) Region 3.

In related work, Colombier et al. [21] observe a wide range of elongation to failure in thin Al films, and attribute this to local stress concentrations such as grain boundary grooves, or a cluster of grains with weak orientations. Our films do not realize the Considère criterion for imperfection-free necking ( $\epsilon_f=n$ ). Colombier [21] found that for films lacking a native oxide the criterion is met only for the strongest and shortest specimens, indicating that weak grains limit  $\epsilon_f$  for most samples. Here, only a few grains span the  $4.4 \mu\text{m}$  tensile bar width. The fracture angle is  $51^\circ$  from the loading direction Fig. 3.11, close to  $54.7^\circ$  as expected from the plane strain

condition [99], [100]. At that angle, only two grains span the fracture region in Fig. 3.11. Surrounding grains are not available to take up the applied stress. Therefore we surmise that weak grains also limit the elongation of our native oxide coated-films.

### **3.5-Summary and conclusions**

A new on-chip test platform has been designed, fabricated, analyzed and used to test mechanical properties of metal thin films. The on-chip test platform features good alignment of the thermal actuator to the specimen, a nearly isothermal specimen temperature and full relief of residual stress through the implementation of pre-inserted microgrippers. The design provides ample force (up to 8 mN) and large displacement (up to 18  $\mu\text{m}$ ) to test the full stress-strain curve of microscale specimens.

The test platform was used to study Al thin film specimens with two different thicknesses (0.63 and 1.03  $\mu\text{m}$ ) and three different lengths (200, 70 and 50  $\mu\text{m}$ ). A detailed analysis (Appendix G) indicates that  $E$  can be evaluated with an accuracy of  $\pm 21\%$ , and  $\sigma_y$  with a better accuracy of  $\pm 5\%$  (one sigma). The thinner tensile bars exhibited high strength, a high strain hardening coefficient and low ductility compared to the thicker specimens. However even in the thicker specimens,  $\epsilon_f$  did not exceed 5%. This is much lower than bulk values, but in good qualitative agreement with several other thin film studies. TEM indicated that a specimen with low ductility experienced local plastic deformation, while a specimen with higher ductility exhibited more uniform plastic deformation throughout the sample.

Our main purpose in this chapter has been to demonstrate a new test platform and evaluate its potential for studying freestanding metal thin film mechanical properties. The design is amenable

to in-situ testing of thin film fatigue, creep and strength size effects. Testing can also be done in-situ inside an environmental chamber [101] while controlling environmental factors such as temperature or ambient.

## **Chapter 4: Statistical Investigation of Size Effect of Yield Stress and Elongation for Free-standing Polycrystalline Al-0.5% Cu Thin Film**

The effect of size on yield stress and elongation for Al-0.5% Cu thin films is investigated experimentally. The controlled dimensions for the specimens are thickness (1.03 and 0.63  $\mu\text{m}$ ) and length (200, 70 and 50  $\mu\text{m}$ ). Thinner and shorter specimens exhibit a larger average yield stress but also a much larger scatter in yield stress. Specimens of larger thickness and shorter length have a larger average elongation but similarly a larger scatter in elongation. The increase in average yield stress with decreasing thickness is linked to the decrease in dislocation length, hence, the increase in yield stress required to bow dislocation. The decreases in average yield stress with length may be attributed to the higher probability of having weaker grain.

### **4.1 Introduction**

Metal films exhibit a considerable increase in their yield stress as their thickness decreases [20], [49], [95], [102]–[107]. However, they also display more brittle behavior and a lesser elongation to failure. The size effects in polycrystalline metal thin films have been investigated by many methods including stress-temperature curves [108], [109], bulge [110], [111], uniaxial tension of thin film on a deformable substrate [104], [107], [112] or uniaxial tension of a free-standing thin films [20], [43], [49], [95], [102], [103], [105], [106].

Although wafer curvature, bulge test and uniaxial tension of thin film on wafer substrate provide important information about the strength size effect, some drawbacks that limit their applicability to inferring information on the strength of free standing films, which are of interest in MEMS applications. For instance, wafer curvature requires thermal cyclic loading which can alter the mechanical properties of thin film by increasing the grain size. It also uses a whole wafer which

may not reflect the strength of a structure with small width and length. Uniaxial tension testing of a thin film on a deformable substrate leads to delay of onset of necking and increase ductility due to the present of the substrate [113].

Recognizing such limitations, researchers have performed testing on free standing thin films. Espinosa et al. [49] studied the strength size effect with respect to thickness and width for free-standing aluminum specimens. Their aluminum thin films had thicknesses of 0.2 and 1  $\mu\text{m}$  and widths of 5, 10 and 20  $\mu\text{m}$ . No size effect was observed with respect to width, however the thin films fractured at different elongations. A large size effect was found with respect to thickness where the 0.2  $\mu\text{m}$  thick specimen fractured in a brittle manner at larger stress and lower elongation. The thin films deformed uniformly until fracture and no necking was observed. Haque et al. [95] tested aluminum specimens with a thickness of 50, 100, 150 and 480 nm and grain sizes of 22, 50, 65 and 212 nm respectively. The 100 nm thick specimen fractured in a brittle manner while the 50 nm thick specimen behaved in a nonlinear elastic way with limited plastic deformation. Also, the strength size effect with respect to length was studied in single crystal copper [114].

In most of the previous work, only a limited number of tests were performed at each size (only one specimen was reported at each thickness in most cases). This is important to note because even though average stress increases, scatter in strength tends to increase as structures decrease in size.

One of the few works where the scatter in strength is reported is the work by Yu et al. [107]. They studied thin copper films on a Kapton substrate. The copper thin films had thicknesses between 0.1 and 3  $\mu\text{m}$ . They indeed found that while the average yield stress increases as the

thickness decreases, the scatter in yield stress also increases. For instance, the yield stress for 1  $\mu\text{m}$  thick specimens were scattered roughly between 400 and 500 MPa, but the yield stress for 0.2  $\mu\text{m}$  thick specimens was scattered between 500 and 900 MPa.

Coulombier et al. [21] studied the scatter in ductility for aluminum thin films where the ductility is the strain at which necking starts. They found that shorter specimens have larger ductility than longer specimens. No information on the scatter of yield stress is reported in their paper due to the nature of their experimental setup [53], which limits their measurement to only one stress and strain value per specimen. The scatter in yield stress has been recognized in single crystal micropillar compression [115]–[117].

In this work, the scatter in yield stress and elongation for the aluminum specimens is quantified. The elongation is defined here as the strain at which failure occurs. In measurements, voltage was applied across the TA legs in steps of 0.01 V, inducing expansion and resulting in shuttle displacement. The grippers engage, and force along with displacement were optically monitored in load cell gages using a 50 X objective lens and transferred to engineering stress and strain by using the cross sectional area and length of the specimen.

## **4.2 Statistical Strength and Elongation Results**

As indicated in the first two columns of Table 4.1, six different tensile specimens were tested. The tensile specimens have lengths  $L$  of 50, 70 and 200  $\mu\text{m}$ . The nominal design thicknesses were 0.7 and 1.1  $\mu\text{m}$  but the actual thicknesses were somewhat less because the release process, which removes the sacrificial oxide film, etches the Al film to a small degree [92]. The actual thicknesses were measured by profilometry to be  $t=0.63$  and  $t=1.03$   $\mu\text{m}$ . Similarly, the width of the specimens was measured by SEM to be  $w=4.4$   $\mu\text{m}$ . As measured by ASTM standard E112

[96], the grain sizes were  $d=3.6 \mu\text{m}$  and  $d=4.8 \mu\text{m}$  for the  $t=0.63 \mu\text{m}$  and  $t=1.03 \mu\text{m}$  films, respectively.

A number  $N=9$  specimens of each size were tested, making for a total of 54. Fig. 4.1 shows an example stress vs. strain curves that were obtained. The stress vs. strain curves for all specimens is included in Appendix H. In general, the  $t=0.63 \mu\text{m}$  specimens strain hardened, as seen in Fig. 4.1a. In a few cases (4 of 27), they exhibited strain softening. The  $t=1.03 \mu\text{m}$  specimens strain hardened and then transitioned to relatively constant stress condition until fracture as shown in Fig. 4.1b for  $L=200 \mu\text{m}$ , or they transitioned to a strain softening regime as shown in Fig. 4.1b for  $L=50$  and  $70 \mu\text{m}$ .

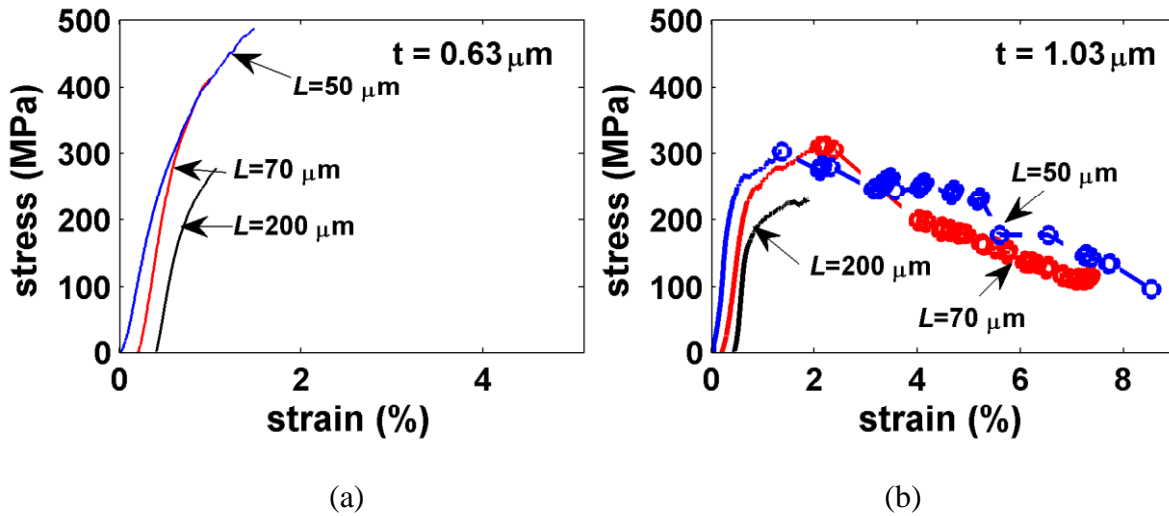


Fig 4.1 Stress versus strain curves up to fracture for some of the thin films, (a)  $t=0.63 \mu\text{m}$ , (b)  $t=1.03 \mu\text{m}$ . Data are offset to make each curve distinguishable

As seen in Fig. 4.1a, the  $t=0.63 \mu\text{m}$  specimens tended to fracture at a small strain of less than 2%. The stress at 0.2% strain is well beyond the elastic proportional limit. For this reason, we adapted a definition for yield stress,  $\sigma_y$ , that is comparable to that used by Espinosa [49]. Here, a

linear fit to the elastic region of the stress vs strain curve and the yield stress was defined as the stress at which the stress vs strain curve deviated from linearity by three times the noise ( $\pm 20$  nm) in the measurements. Table 4.1 summarizes the results.

Table 4.1: Summary of Specimens and Results

$t$ ( $\mu\text{m}$ )	$L$ ( $\mu\text{m}$ )	$N$	yield stress ( $\sigma_y$ ) range (MPa)	Average yield stress $\bar{\sigma}_y$ (MPa)	Elongation ( $\varepsilon_f$ ) range (%)	Avg. elongation ( $\bar{\varepsilon}_f$ ) (%)
0.63	200	9	165-234.5	198.8 $\pm$ 22.96	0.67-1.57	0.98 $\pm$ 0.3
	70	9	219.7-360	296.6 $\pm$ 41.51	0.83-3.13	1.38 $\pm$ 0.69
	50	9	230-358	294 $\pm$ 37.45	0.99-4.82	1.98 $\pm$ 1.46
1.03	200	9	138-164	151.7 $\pm$ 7.61	0.84-3.09	1.62 $\pm$ 0.68
	70	9	191.7-229	216.6 $\pm$ 11.77	1.5-7.4	4.6 $\pm$ 2.08
	50	9	185.1-230	211.4 $\pm$ 15.79	1.4-10.3	4.7 $\pm$ 3.03

We now explore the effect of geometry on yield stress  $\sigma_y$  and elongation  $\varepsilon_f$ . Fig. 4.2a shows  $\sigma_y$  plotted against  $t$ . Note that the filled markers are for  $t=0.63 \mu\text{m}$ , while the unfilled markers are for  $t=1.03 \mu\text{m}$ . For the same  $t$ , the data is slightly offset so that the different  $L$  values can be distinguished. The  $t=0.63 \mu\text{m}$  specimens show a higher average yield stress  $\bar{\sigma}_y$  and a larger scatter in  $\sigma_y$  than the  $t=1.03 \mu\text{m}$  specimens.

Fig. 4.2b shows  $\sigma_y$  plotted against  $L$ . Here for the same  $L$ , the data is slightly offset so that the different  $t$  values can be distinguished. The  $L=200 \mu\text{m}$  specimens show smaller  $\bar{\sigma}_y$  and lesser scatter in  $\sigma_y$  while the  $L=70$  and  $50 \mu\text{m}$  specimens display larger  $\bar{\sigma}_y$  but greater scatter. The shaded bands indicated the range for the  $t=0.63 \mu\text{m}$  and  $t=1.03 \mu\text{m}$  specimens, respectively.

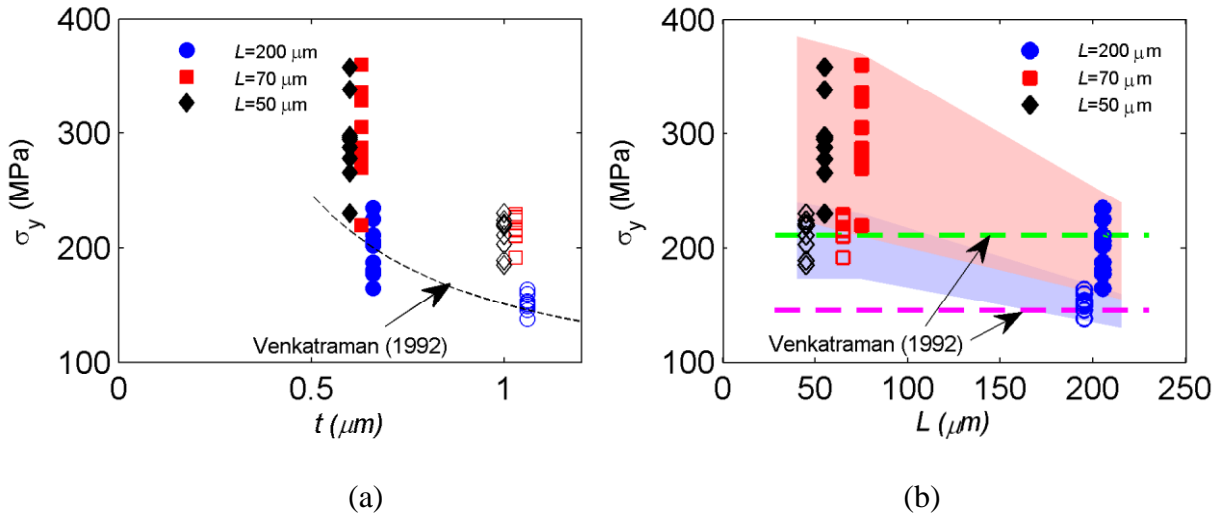


Fig. 4.2 Yield stress ( $\sigma_y$ ) size effect in (a) thickness  $t$  and (b) length  $L$ . The data are slightly offset to distinguish the different thicknesses and lengths. (filled markers are  $t=0.63 \mu\text{m}$  specimens while unfilled markers indicate  $t=1.03 \mu\text{m}$ )

In both Figs. 4.2a and 4.2b, the scatter in  $\sigma_y$  for the  $L=50$  and  $70 \mu\text{m}$  specimens is comparable; this can be attributed to the comparable size between both specimens.

As is evident from both Figs. 4.2a and 4.2b, the strength increases for the thinner samples but the range of the data also becomes larger. The ratio of the standard deviation in yield strength to the average yield strength is 0.06 for  $1 \mu\text{m}$  thick samples, and more than doubles to 0.13 for  $0.6 \mu\text{m}$  thick samples. This is true for all three specimen lengths, as shown in Fig. 4.3.

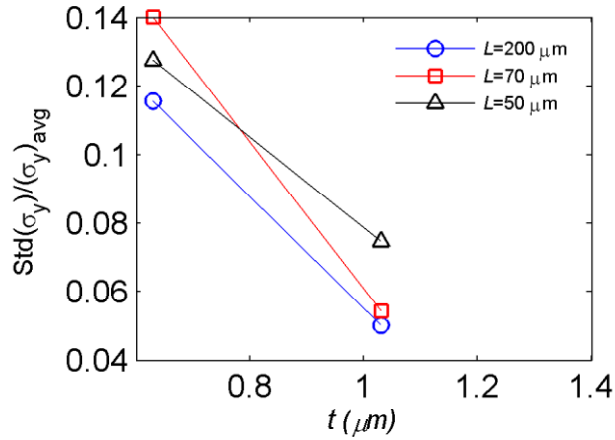


Fig 4.3 the ratio of standard deviation to average of yield stress vs. thickness

It can be noted that the elongation can be greatly increased by placing the film on a strain hardening polymeric substrate [113]. This will greatly increase film ductility by homogenizing the strain. The data here accurately reflect  $\sigma_y$  and give the actual elongation for a freestanding film. Figs. 4.4a and 4.4b show the elongation  $\varepsilon_f$  of the freestanding specimens as a function of  $t$  and  $L$ , respectively. The average elongation  $\bar{\varepsilon}_f$  increases as the thickness of the specimen increases and the scatter of the elongation increases as well. The  $L=50 \mu\text{m}$  specimens have larger  $\bar{\varepsilon}_f$  and larger scatter followed by the  $L=70 \mu\text{m}$  long specimens. The average elongation is summarized in Table 4.1.

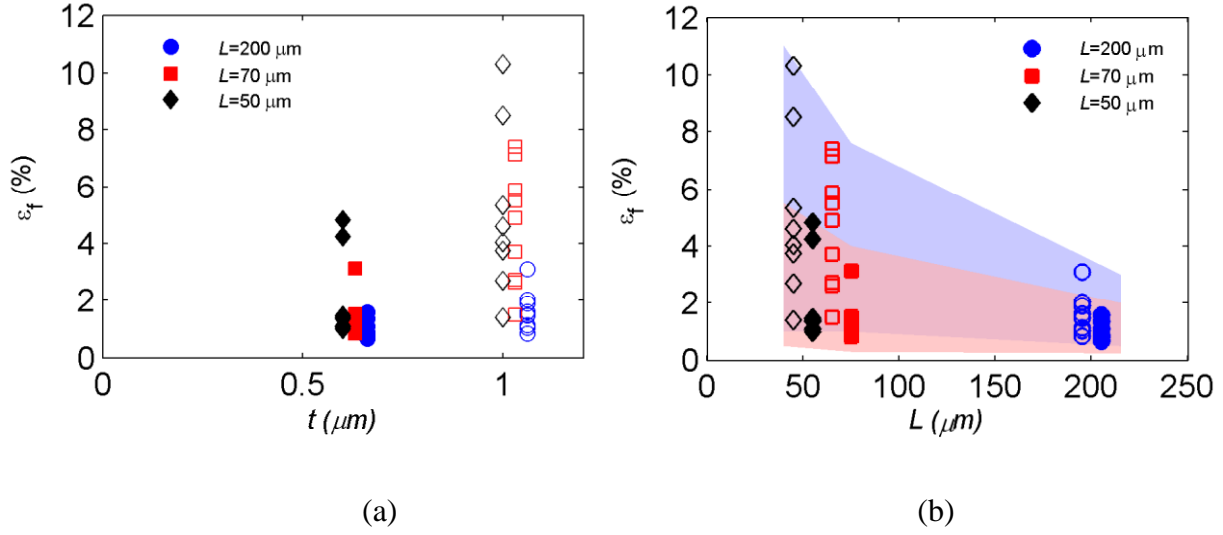


Fig. 4.4 Elongation size effect in (a) thickness (b) length. The data are slightly offset to distinguish the different lengths or thickness. (filled markers are  $t=0.63 \mu\text{m}$  specimens while unfilled markers indicate  $t=1.03 \mu\text{m}$ )

The film resolved shear stress may exert force on threading dislocations, leaving an edge dislocation trail at the substrate/film and/or oxide/film interface (Fig. 24 of ref. [118]). If the work done by the film per unit area is equal or greater than the energies of the dislocations that deposit at the interface, the film strength prediction is

$$\sigma_y = \frac{\sin\phi}{\cos\phi \cos\lambda} \frac{b}{\pi(1-\nu)t} \left[ \frac{\mu_f \mu_o}{\mu_f + \mu_o} \ln \left( \frac{\beta_o t_o}{b} \right) \right]. \quad (4.1)$$

Here  $\sin\phi/\cos\phi \cos\lambda=3.464$  for a  $\langle 111 \rangle$ -oriented fcc film. For the Al film, the Burgers vector  $b=0.286 \text{ nm}$ , the Poisson's ratio  $\nu=0.31$ , and the shear modulus  $\mu_f=24.8 \text{ GPa}$ . The oxide shear modulus  $\mu_o=178.9 \text{ GPa}$ , its thickness is taken to be  $t_o=5 \text{ nm}$ , and the constant  $\beta_o=17.5$ . With these values, Eq. 4.01 reduces to  $\sigma_y=57 \text{ MPa}\cdot\mu\text{m}/t$ .

Venkatraman and Bravman [34] studied strength versus temperature of sputtered Al-0.5% Cu films similar to those in this study using a wafer curvature technique. The film was constrained

by a silicon substrate and an anodic oxide alumina film. Their data indicated that yield stress depends on thickness and grain size according to

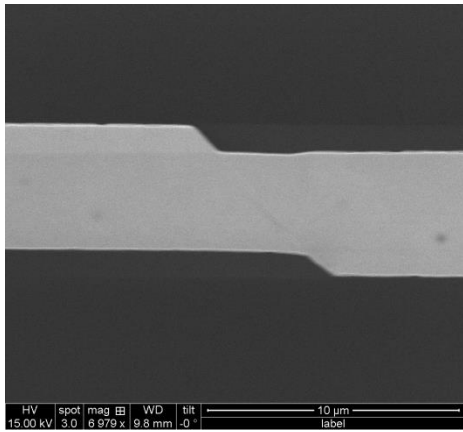
$$\sigma_y = \frac{m_{thick}}{t} + \frac{m_{HP}}{\sqrt{d}} \quad (4.2)$$

Extrapolating their data to 25 °C,  $m_{thick}=95 \text{ MPa}\cdot\mu\text{m}$ . This experimental value is larger roughly by a factor of two than the value predicted by Nix's theory (a version of Eq. (4.1) that accounts for the different substrate modulus) The parameter  $m_{HP}=115 \text{ MPa}\sqrt{\mu\text{m}}$  reflects Hall-Petch hardening, and is added to account for grain size effects For a grain size/thickness combinations of ( $d\approx 3.6 \mu\text{m}/t=0.63 \mu\text{m}$ ) and ( $d \approx 4.8 \mu\text{m}/t =1.03 \mu\text{m}$ ), this results in predictions of  $\sigma_y=211$  and 145 MPa, respectively for the current specimens. The predicted trend is plotted in Fig.4.2a as a dashed line (the  $d$  dependence accounts for only a 6 MPa difference and hence the trend is displayed as a single line). The trend is plotted as horizontal dashed line in Fig. 4.2b because there is no functional dependence on  $L$ . Note that for the shorter values of  $L=50$  and  $70 \mu\text{m}$ ,  $\sigma_y$  is strongly underpredicted, while the range in  $\sigma_y$  is nearly as large as the value predicted in Eq. (4.1).

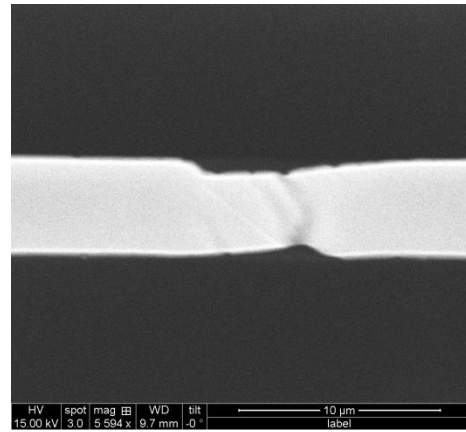
The agreement between the Eq. (4.2) predictions and the  $\bar{\sigma}_y$  results from the  $L=200 \mu\text{m}$  specimens are remarkably good. This attests to the likelihood that the Al film has developed a scale in the present samples which provides an excellent barrier to dislocation motion at the top and bottom of the film. However, there clearly are other important mechanisms that must be involved in order to explain the  $\sigma_y$  dependence on  $L$  as well as the scatter in  $\sigma_y$ . It should be noted, however, that specimen thinning [20], as discussed in the Chapter 1, is not a likely mechanism here. If it were, the very good agreement in strength between Eq. (4.2) and the  $L=200 \mu\text{m}$  data would not be expected.

The 0.63  $\mu\text{m}$  thick specimens tend to exhibit strain hardening until an abrupt fracture event, while the 1.03  $\mu\text{m}$  thick specimens show either a small amount of strain hardening followed by constant stress until fracture or strain softening. The reason behind strain softening was investigated by interrupting some experiments when the strain softening started. Fig.4.5 shows two specimens that showed strain softening. As we can see, necking and slip has occurred in these specimens and the cross sectional area has decreased. The necking and slip happens abruptly, which leads to a burst in strain. The apparent strain softening is attributed to the use of the original cross sectional area to calculate stress rather than using the area after necking.

After the first slip occurs, the materials show strain hardening again until the next slip incidence where a new burst in strain and another drop in stress takes place. Usually, the subsequent slip incidents have less strain burst than the first one. This process continues until fracture happens and a serrated region is observed in some of the stress-strain curves. In some cases the slip happens very quickly and the whole specimen fractures immediately as soon as necking starts. Usually the slip happens at an angle between  $25^{\circ}$ - $50^{\circ}$  with respect to the cross-sectional area plane.



(a)



(b)

Fig. 4.5 Two interrupted experiments where specimens show strain softening (a) 0.63  $\mu\text{m}$  thickness (b) 1.03  $\mu\text{m}$  specimen. The specimens show necking which correlates with the strain softening.

Fig. 4.6 shows some specimens that experience strain hardening until fracture. The specimens either fracture in no specific pattern which might be an indication of a complex fracture process, or sometimes a fracture with an angle with respect to the plane of cross-sectional area which is an indication of the occurrence of slip but the specimen fractures immediately as the slip start.

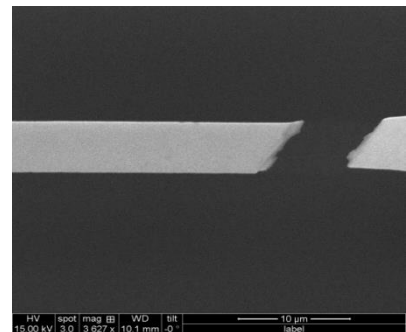
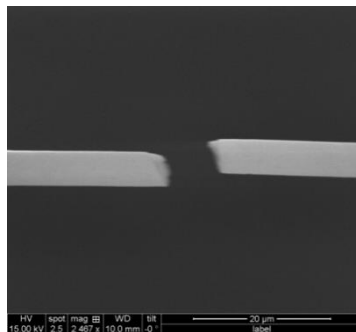
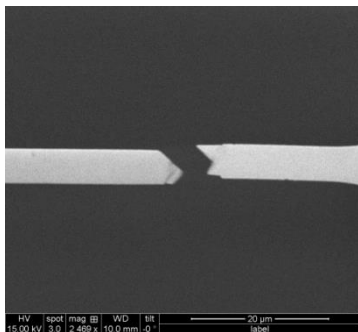


Fig. 4.6 Fracture region for some specimens ( $t = 0.63 \mu\text{m}$ ) that show strain hardening till fracture

In general, the size effect in yield stress should be a function of grain size, specimen thickness and specimen length and can be expressed as

$$\sigma_y = \sigma_o + k_1 d^{-n} + k_2 t^{-m} + k_3 L^{-p} \quad (4.3)$$

The first two terms are the well-known Hall-Petch equation. The exponent  $n$  commonly has the value 0.5. The determination of the exponents and the constants require a large number of experiments at different grain sizes, thicknesses and lengths.

There are two mechanisms that could be linked to the observed strength size effect in thickness and length. The yield stress size effect in thickness can be attributed to the increase in stress required to bow smaller dislocations. The  $t=0.63 \mu\text{m}$  is smaller in thickness, thus the Frank-Read source is expected to be smaller and a larger stress is required to activate this source. The other mechanism which is connected to the length is the grain orientation. The  $200 \mu\text{m}$  long specimens have a larger number of grains, therefore, they have a larger probability of having a weaker grain.

### **4.3 Summary**

The stress and elongation of thin polycrystalline aluminum thin films shows scatter and the scatter increase as the length and thickness of thin films decreases. The thinner and shorter specimens show larger average stress and larger average elongation. The size effect and scatter in yield stress can be linked to the smaller size of dislocations in the  $t=0.63\mu\text{m}$  specimens and to the larger probability of having weaker grain for the long specimens.

## Chapter 5: Conclusions and Future Work

### 5.1 Summary and Conclusions

An existing test platform was evaluated for the use in strength size effect study of polysilicon. A misalignment issue was discovered where the test platform experience small lateral displacement and small rotation. This misalignment issue is attributed to the asynchronous engagement of the grippers where one side of the grippers engages before the other side. The non-simultaneous engagement issue is not severe for the longer tensile bars, but it introduces large error for the smaller ones. Therefore, a new test platform with excellent in-plane sample alignment for all specimen sizes was developed for polysilicon testing.

With this platform, a size range of a factor of 100 has been modeled, designed, fabricated and tested. Test results show increase in polysilicon strength as the specimen size decrease. The average strength has increased from 2.7 to 4.2 GPa.

The prediction of strength size effects based on strength data from only the large tensile bar does not work very well and the strength of two different size tensile bars is required for better estimation of Weibull parameters. In addition to estimating Weibull parameters from two specimens we need to account for the change in threshold strength due to non-uniform stress distribution along the notch ligament. The threshold strength is an estimate of the largest crack size, and we showed that for notched tensile bars, it is not a constant because for the same size flaw, the apparent strength depends on the stress distribution across the crack face.

A new test platform for in-situ on-chip testing of aluminum with excellent alignment and load resolution has been designed. The test platform incorporated high force, large displacement range thermal actuators and pre inserted microgrippers to relieve residual stress in the aluminum specimens.

A combination of thermal resistor and heat sink is adapted to shunt heat to the substrate. Using finite element method, the temperature gradient along aluminum tensile bars is found to be less than 3 °C in air. Young's modulus and stress are determined by performing error analysis to be within 21% and 5% accuracy respectively.

The test platform was used to investigate the yield stress and elongation size effect in aluminum. Aluminum thin film structures over a size range of 6.5 increase in average yield strength from 140 MPa to 300 MPa. Unlike macroscale specimens, these samples also exhibit significant scatter in strength. The ratio of the standard deviation in yield strength to the average yield strength is 0.06 for 1 μm thick samples, and more than doubles to 0.13 for 0.6 μm thick samples.

## **5.2 Future Work**

The future work can be divided into experimental and analytical.

For the experimental part, the aluminum test platform can be used to study different specimens with different sizes and investigate the effect of length, thickness and grain size on the yield stress. Also, the test platform can be used to investigate creep in thin films by applying uniform fixed load on the specimen which was not done before, a sample creep experiment is shown in Appendix I. Other interesting experiments is fatigue loading where the specimen is loaded in

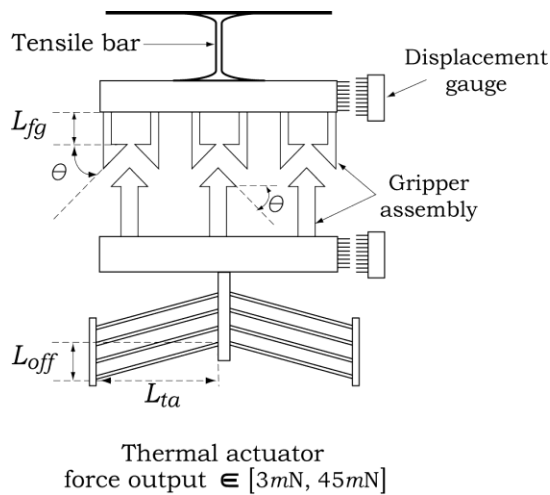
tension then the load is removed and by repeating this cyclic load we can obtain important information on the fatigue of thin

For the analytical part, the Monte Carlo simulation needs to be improved for accurate prediction of strength for notched specimens. Other distributions for the RVEs such as log-normal might be used to investigate the accuracy of prediction; also, other functions for the flaws distribution can be investigated to figure out what is the best combination of RVEs and flaws distribution.

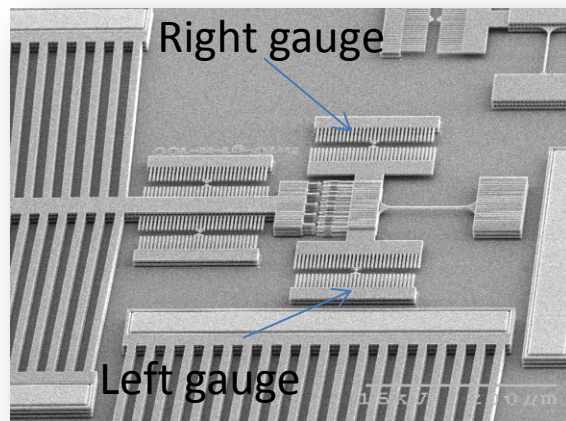
The size effect in aluminum can be investigated by discrete dislocation dynamic or Monte Carlo simulation to come up with model that predict the scatter in the yield stress and the yield stress size effect.

## Appendix A: Hazra's test platform [54]

As shown in Fig. A1, Hazra's design (the gripping design) consists of a freestanding tensile bar connected to the substrate at one end and with a freestanding block attached to female grippers at the other end. Male grippers, which are initially not in contact with the female grippers, are connected to a chevron thermal actuator through the shuttle. An increasing difference in potential is applied through the thermal actuator legs, causing them to heat and inducing a linear movement (through thermal expansion) to the male grippers. After applying enough voltage, the grippers become completely inserted. Now the voltage is reduced and the grippers engage. The loading of the tensile bar occurs by reducing the voltage until fracture. The tensile bar displacement is monitored using the gauges on either side of the crosshead by detecting the relative phase of reference and object gratings. The displacements are transformed into stresses and strains by using a linear finite element model of the test structure.



(a)



(b)

Fig A1 Hazra's design (a) schematic view (b) SEM of fabricated structure (Hazra 2010)

We had originally intended to use the gripping design for our work, so several tests were performed using this design. However, a misalignment issue was discovered during our tests. This issue was critical for the smaller scale tensile bars tested in this project. As seen in Fig. A2, displacement gauges are attached on both sides of the test structure. A series of tests were performed and the axial displacement was measured at each displacement gauge three times. When the results from the two gauges were compared, it was found that one of the gauges always had larger displacements than the other gauge, as seen in Fig. A2. Although Fig. A2 gives results for one of the worst cases, it represents a significant problem, as explained below.

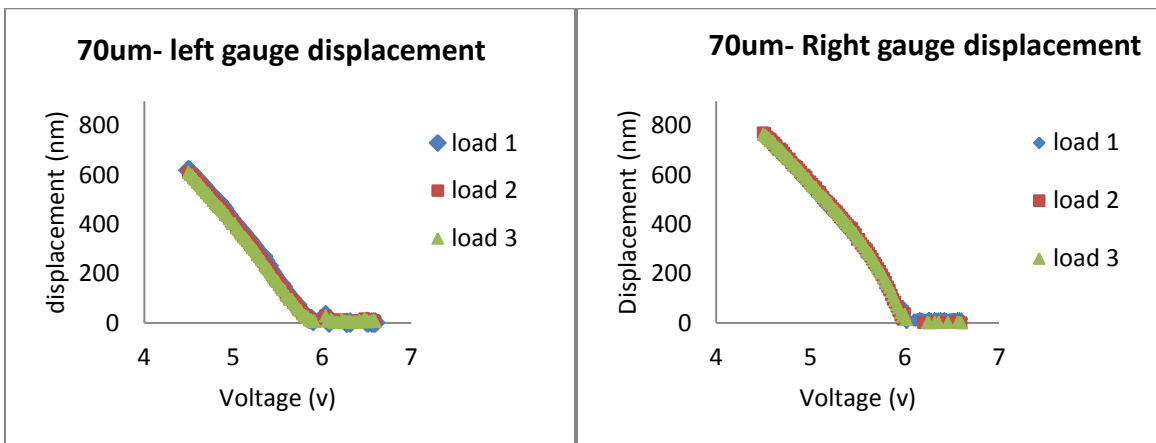


Fig. A2 The axial displacement recorded at both displacement gauges for the same test structure (tests were performed without breaking tensile bar) Note that for the same voltage, the displacement is larger for the right gauge than the left gage.

Upon cooling, gripper engagement does not happen simultaneously and almost always one side engages before the other. The cross-head displacement and lateral displacement and rotation were monitored as shown in Fig A3. We determined that the cross-head experiences rotation and some lateral displacement upon loading as shown in Fig A4. Consequently, the gauge on the side where the grippers engage first, records larger axial displacements.

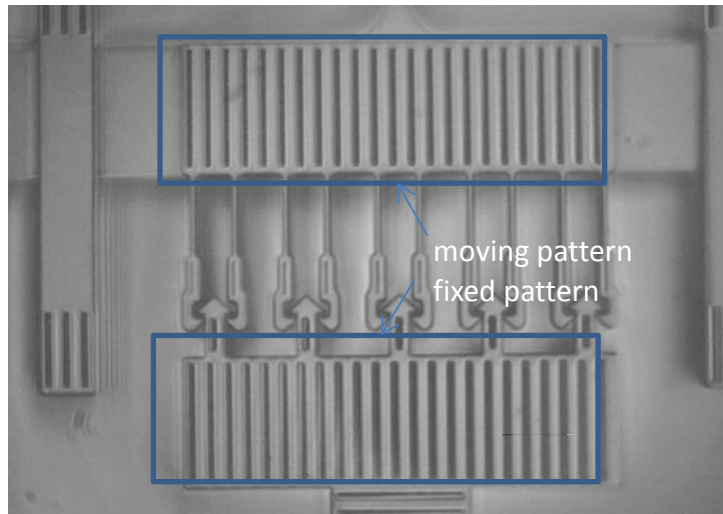


Fig. A3 The cross-head displacement is monitored to quantify misalignment

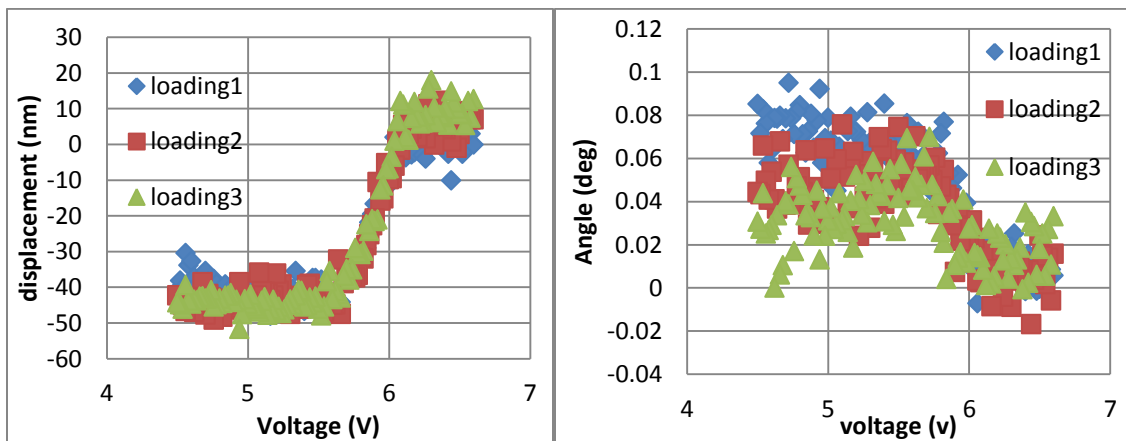


Fig A4 Lateral displacement and rotation of cross-head during loading

Although the rotation of the cross-head is small, it is amplified at the displacement gages by amount of  $L\theta$ , where  $L$  is the distance between the grippers and the displacement gage which is around  $150\ \mu\text{m}$ , and  $\theta$  is the rotation angle. This can give rise to a discrepancy of 30 nm, depending on whether the measurement is made on the left or right side of the crosshead. When the tensile bar is short (e.g.,  $L=7\ \mu\text{m}$ ), this translates into a strength error of up to 0.23 GPa, well beyond the acceptable range. Also, we have

## Appendix B : Displacement results

In this appendix, the displacement values at fracture are given for all the specimens tested in Chapter 2.

Displacement Results for Sp 1 (nm)						
1198.7	1202.6	1219.5	1235.9	1245.8	1252.2	1252.3
1261.18	1264.2	1267.48	1285.3	1287.5	1298.6	1299.68
1305.5	1309.2	1311.68	1143.4	1144.1	1327.9	1161
1168.7	1342.5	1353.2	1188.5	1376.4	1209.3	1387.2
1224.6	1226.1	1227.8	1229.7	1234.2	1238.5	1240.6
1439	1278.6	1283.4	1286.4	1310.8	1313.5	1331.1
1347						

Displacement Results for Sp 2 (nm)						
327.45	343.2	285.04	351.2	358	361	361.1
361.7	361.85	362.8	363.833	366.4	366.43	369
370.83	371.19	375.5	376	317.78	318.77	385.6
324.13	324.77	391	397.3	336.54	402.9	340.33
343.92	409.4	346.8208	349.73	352.6	417.63	418.5
418.6	367.84	436.4	373.2	375.28	376.11	376.25
440.8	443.6	384	389.33	455.7	417.21	

Displacement Results for Sp 3 (nm)						
223.54	233.1	238.2	189.26	242.5	203.68	210.2
264.65	264.9	265.3	269.38	272.2	272.8	220.62
276.64	226.98	226.99	280.14	228	283.4	287.3
235.91	289.8	291.44	292.24	293	293.44	294.2
242.1	242.42	294.84	245.33	297.7	298.61	246.6
299.9	300.6	248.48	301.5	302.04	302.14	250.24
251.16	304.01	304.54	253.91	306.5	254.64	255.22
308.3	309.35	310.8	260.1	260.25	313	261.41
314.2	265.02	267.47	269.2	269.22	270.11	271.51
272	272.2	275	275.65	275.83	331	281.54
289.6	291.65	292.51	295.6	314.87		

Displacement Results for Sp 4 (nm)						
147.52	193.9	194.3	195.1	196.5	154.96	158.65
207.1	207.5	162.14	208.82	169.6	216.7	218.1
218.5	172.24	220.1	220.15	174.51	174.85	224.8
178.92	225.36	180.15	226.7	226.7	227.55	181.77
182.54	229.5	184	231.95	232.56	233	233.1
187.57	188.18	189	235.7	189.38	236.5	190.74
190.83	190.92	191.75	191.96	239.565	195.15	241.8
199.7	246.51	200.6	200.95	201.5	248.2	202.5
250.365	204.13	251.3	252.565	206.3	208.22	208.34
256.76	257.5	257.8	217.11	265	219.33	227.57
230.95	231.3	231.6	250.72			

Displacement Results for Sp 5 (nm)						
98.03	110.6	163.1	164.2	166.4	167.3	121.77
122.21	168.75	122.66	170.54	172.4	173.5	173.5
174.11	175.4	175.5	129.8	177.1	177.51	134.15
181.2	134.91	136.13	182.7	137.13	137.71	184.9
184.9	187.94	188.6	190.3	145.89	146.23	194.2
194.6	148.31	196.3	197.72	199	200.1	154
154.34	204.1	204.3	205.3	159.41	206.1	207.8
161.43	210.1	175.41	177.44			

## Appendix C: Weibull 2 parameter prediction

Fig. C1 shows the W2P and W3P fits using the maximum likelihood method for Specimens 1-4 from Chapter 2. Tables B1 and B2 give the best fit Weibull parameters for W2P and W3P, respectively. Figure C2 shows that using the W2P fit of Sp1, the prediction of Sp2, Sp3 and Sp4 is relatively poor.

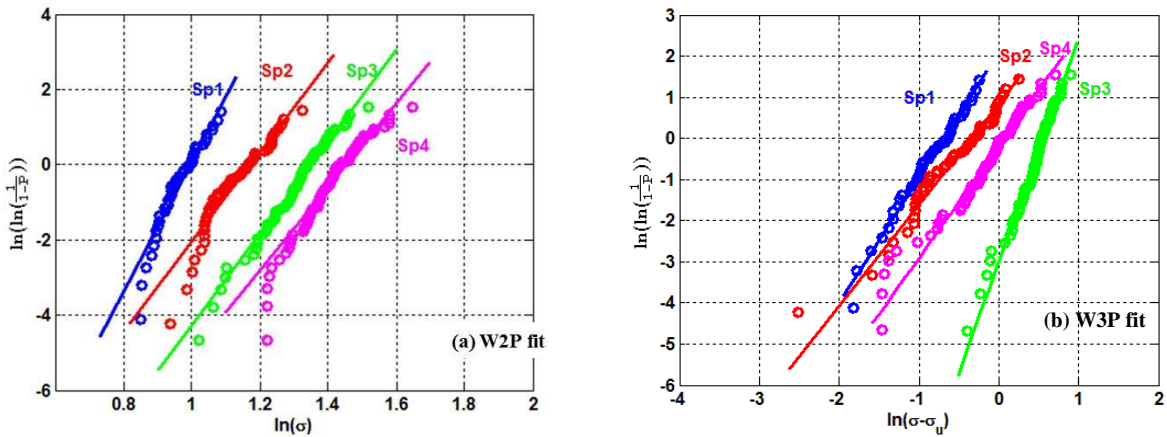


Fig. C1. (a) Best W2P fits to each specimen. (b) Best W3P fits to each specimen by Maximum likelihood method.

Table B1 W2P parameters for each specimen

Specimen	$N$	$m$	$\sigma_\theta$ (GPa)
1	43	17.3	2.71
2	45	11.9	3.23
3	75	12.2	3.86
4	74	11.1	4.28

Table B2 W3P parameters for each specimen

Specimen	$N$	$m$	$\sigma_u$ (GPa)	$\sigma_\theta$ (GPa)	$\sigma_u + \sigma_\theta$ (GPa)
1	43	3.05	2.18	0.50	2.68
2	45	2.46	2.47	0.71	3.18
3	75	12.2	2.10	1.74	3.84
4	74	11.1	3.15	1.07	4.20

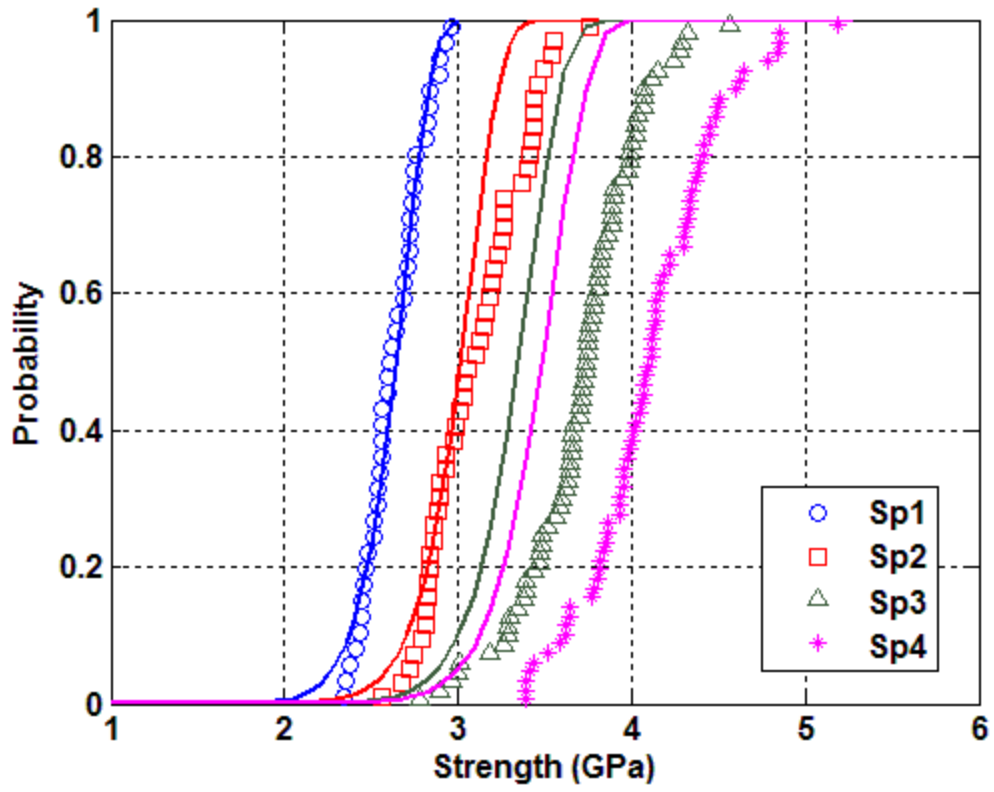


Fig. C2. W2P Strength prediction of Specimens 2-4 using Specimen 1 data.

## Appendix D: Specimen 5 experimental Results

Specimen 5 shows strength that is comparable to Specimen 4.

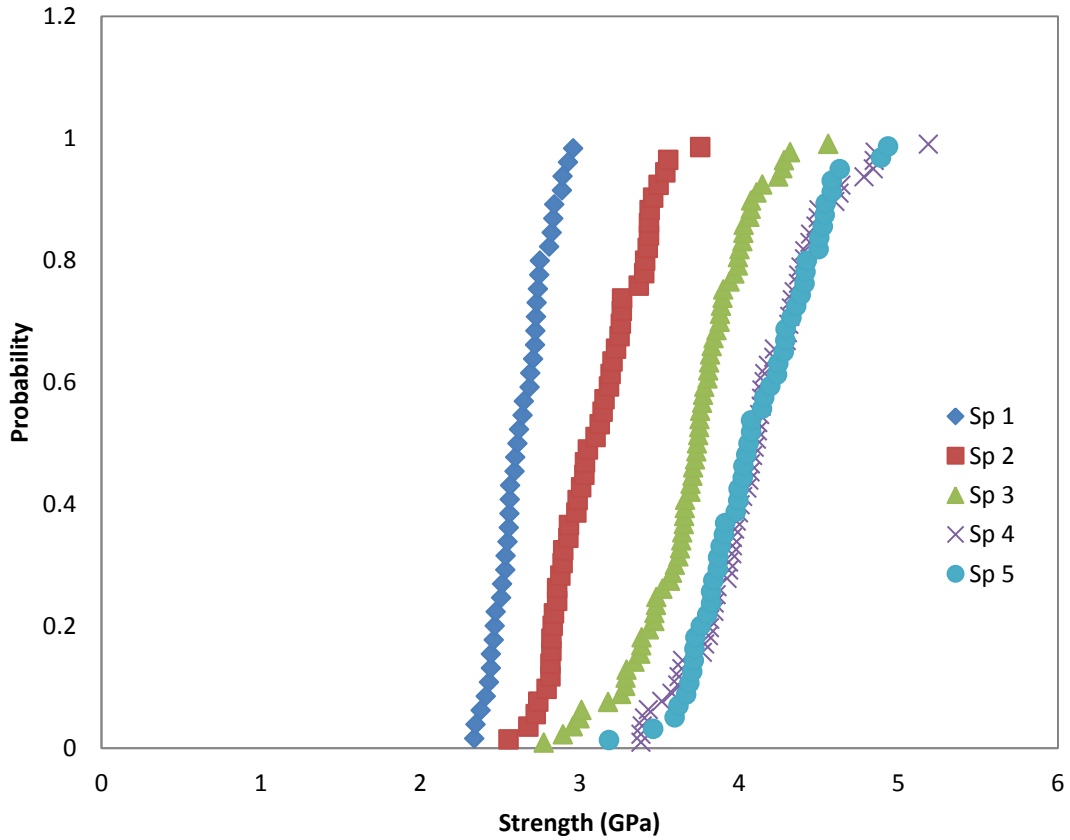


Fig. D1 Strength distribution for all specimens

## Appendix E: Elastically connected design for the AI test platform

The elastically connected design as shown in Fig. E1 has the specimen connected directly with the test platform. This design induces a large residual stress as shown in Fig. E2. The residual stress is measured to be around 100 MPa. The out of plane deflection is measured by interferometry as shown in Fig E3. The out of plane deflection agrees very well with a multi-physics model that was developed in ANSYS to study the structural response as shown in Fig.E3(a). The ANSYS model is shown in Fig E.4.

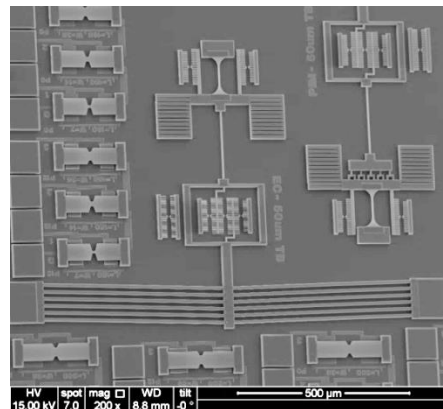


Fig. E1 SEM image of the elastically connected design

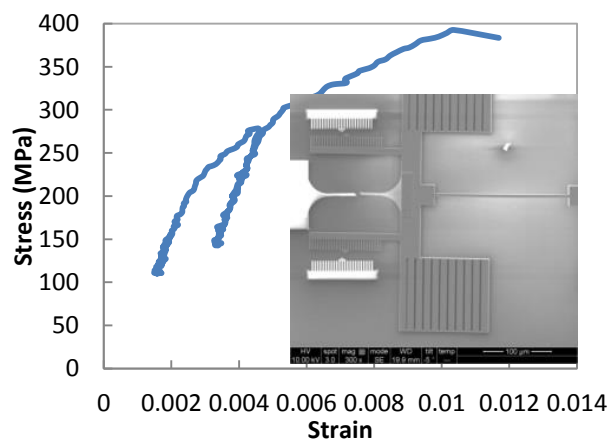
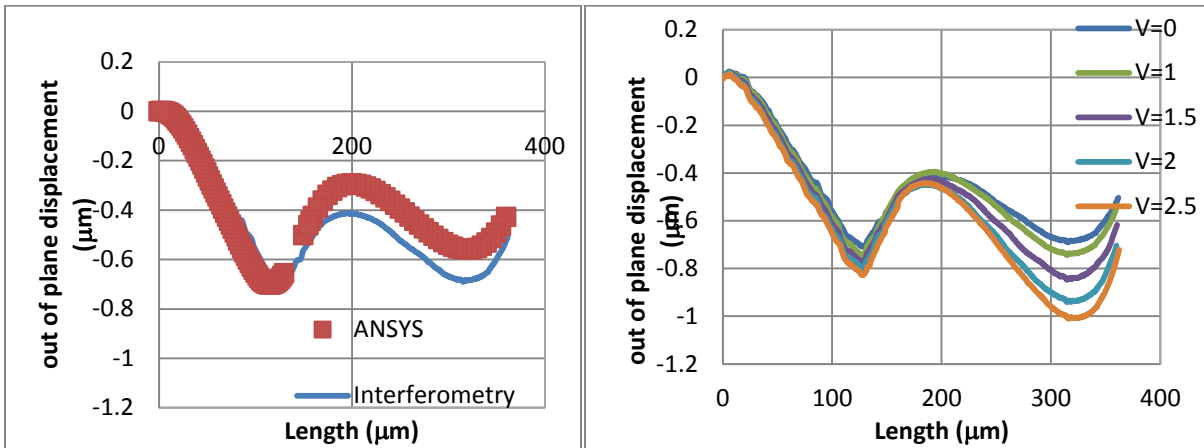


Fig. E2 Stress vs. strain curve for one of the specimens from the elastically connected design. Our measurement start from around 100 MPa due to large residual stress



(a)

(b)

Fig. E3 Out of plane displacement for the specimen and thermal resistor at (a) 0V compared to ANSYS results (b) at different voltages

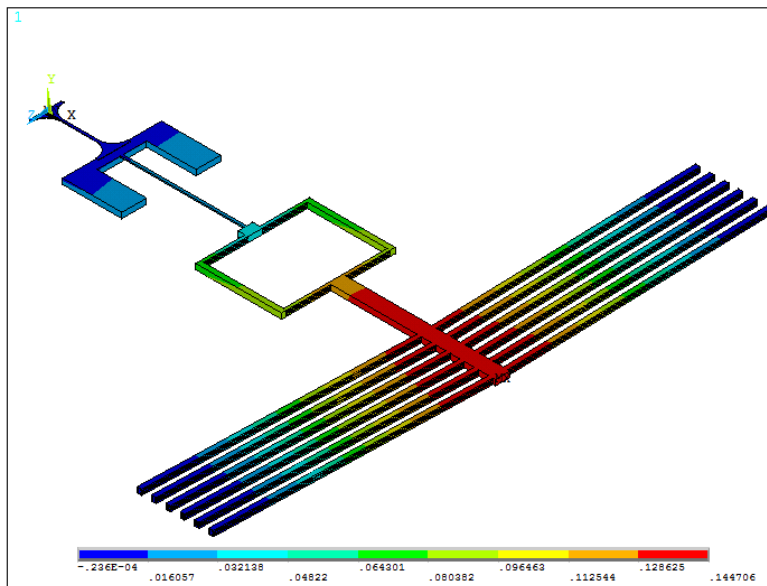


Fig. E4 3D-ANSYS multi-physics model to the test platform

## Appendix F: Finite element analysis of temperature of the aluminum test platform

A 3-D multi-physics (electrical-thermal) finite element model was developed in ANSYS to assess the temperature across the tensile specimen. In this section, we describe the finite element model and the properties that used in the model. Because the contact resistance is not well known, the microgrippers were simply modeled as solid elements. As explained in the main body, the temperature at the cross-head is expected to be somewhat lower than the one found here. The solid model for the test platform, as shown in Fig. F1, consists of the tensile specimen made from aluminum, while the rest of test platform is made from polysilicon. A voltage difference is applied between the thermal actuator legs. The applied voltage difference through the TA legs leads to Joule heating and expansion of the legs. Two important properties are needed for the polysilicon, which are the electrical resistivity and heat conductivity as a function of temperature.

The polysilicon change in resistivity with temperature can be expressed as [119], [120]

$$\rho = 2.9713 \times 10^{-2} T + 20.858 \quad T < 300 \text{ } ^\circ\text{C} \quad (\text{F1a})$$

$$\rho = 6.16 \times 10^{-5} T^2 - 7.2473 \times 10^{-3} T + 26.402 \quad 300 \text{ } ^\circ\text{C} < T < 700 \text{ } ^\circ\text{C} \quad (\text{F1b})$$

$$\rho = 8.624 \times 10^{-2} T - 8.8551 \quad T > 700 \text{ } ^\circ\text{C} \quad (\text{F1c})$$

where  $\rho$  is resistivity in  $\Omega \cdot \mu\text{m}$  unit and  $T$  is temperature in Celsius.

The change in thermal conductivity with temperature for polysilicon is shown in Fig. 4 and can be expressed as [93]

$$\kappa_p = \frac{1}{-2.2 \times 10^{-11} T^3 + 9 \times 10^{-8} T^2 - 1 \times 10^{-5} T + 0.014} \quad , \quad (F2)$$

where  $\kappa_p$ : is thermal conductivity of polysilicon in W/(m.K).

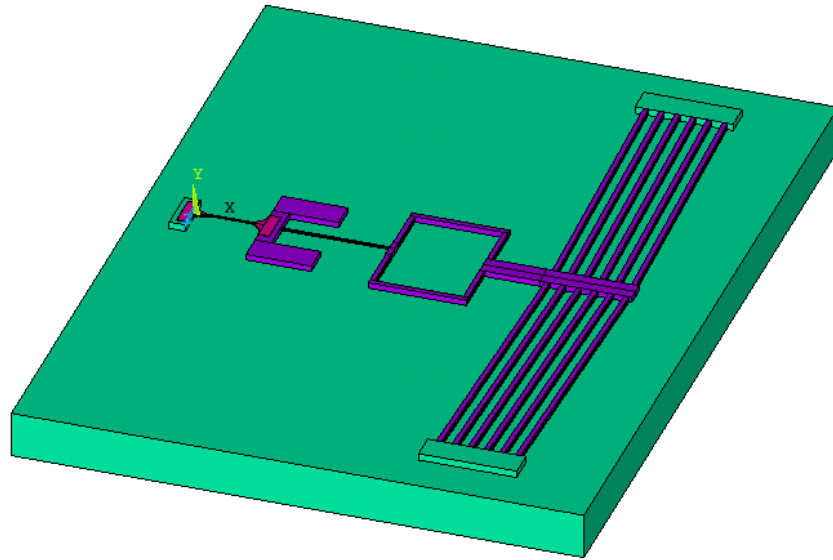


Fig. F5 Test platform modeled in ANSYS

Heat conduction to the substrate is included in the model by introducing an air rectangular volume surrounding the test platform. All sides of the air cube assumed to be insulated except the one that contacts the substrate, which shares the substrate temperature. The air volume is made large enough that any increase in the air volume has no effect on the temperature distribution results.

Two different solid elements were used in the model, Solid227 for polysilicon and Solid90 for aluminum, substrate and air. The Solid227 is a 3D element used in multi-physics analysis that has the capability of modeling the Joule heating in polysilicon, Solid90 element is used for 3D transient or steady-state thermal analysis and was used in our finite element analysis to model heat transfer to the substrate. The total number of elements used in the model was 195063

elements distributed as 24686 element for polysilicon, 1482 element for aluminum, 38224 element for substrate and 130671 element for air.

A fixed temperature boundary condition of 25 °C was applied to the substrate. A voltage of 11 V is applied across the TA legs and the cross-head temperature is extracted from the model and was found as 29 °C, which is 4 °C greater than the substrate temperature. However, the specimens fracture at much lower voltage (3 V - 5 V). Therefore, the cross-head temperature is found to be in the range between 27- 28 °C. (2 -3 °C greater than the substrate temperature).

## **Appendix-G: Uncertainty analysis for stress $\sigma$ , strain $\varepsilon$ and modulus of elasticity $E$**

The error in  $\sigma$ ,  $\varepsilon$  and  $E$  comes from two main sources. These are the uncertainty in the load cell and tensile specimen dimensions and the uncertainty in the measured displacement values. The error estimate is carried out utilizing the partial derivative definition for the variance. For a given function  $f(x_1, x_2, \dots, x_n)$ , let us assume that  $x_1, x_2, \dots, x_n$  are random independent variables with variances  $V_1, V_2, \dots, V_n$  respectively. (The standard deviation is related to the variance as  $S_i = \sqrt{V_i}$ ). The variance of  $f(x_1, x_2, \dots, x_n)$  can be expressed as [121]

$$V_f = \left(\frac{\partial f}{\partial x_1}\right)^2 V_1 + \left(\frac{\partial f}{\partial x_2}\right)^2 V_2 + \dots + \left(\frac{\partial f}{\partial x_n}\right)^2 V_n \quad . \quad (G1)$$

Equation (B1) can be written in compact form as

$$S_f = \sqrt{\sum_{j=1}^i \left(\frac{\partial f}{\partial x_j}\right)^2 S_j^2} \quad , \quad (G2)$$

where  $S_f$  is the standard deviation of the function  $f$  and  $S_j$  is the standard deviation of the variable  $j$ .

### **Uncertainty in Stress**

The engineering stress can be calculated as

$$\sigma = \frac{F}{A} = \frac{k_{LC} \delta_{LC}}{w_{TS} t_{TS}} \quad , \quad (G3)$$

where  $k_{LC}$  is the stiffness of the load cell spring,  $\delta_{LC}$  is the displacement of the load cell,  $w_{TS}$  is the width of the tensile specimen,  $t_{TS}$  is the thickness of tensile specimen. Equation G3 can be rewritten by substitution for the spring's stiffness

$$\sigma = \frac{E_{LC} t_{LC} w_{LC}^3 \delta_{LC}}{w_{TS} t_{TS} l_{LC}^3} , \quad (G4)$$

where  $E_{LC}$  is the modulus of elasticity of the spring material (polysilicon),  $t_{LC}$  is spring thickness,  $w_{LC}$  is spring width and  $l_{LC}$  is spring length. The variance of stress can be calculated as

$$V_{\sigma} = \left( \frac{\partial \sigma}{\partial E_{LC}} \right)^2 V_{E_{LC}} + \left( \frac{\partial \sigma}{\partial t_{LC}} \right)^2 V_{t_{LC}} + \left( \frac{\partial \sigma}{\partial w_{LC}} \right)^2 V_{w_{LC}} + \left( \frac{\partial \sigma}{\partial \delta_{LC}} \right)^2 V_{\delta_{LC}} + \left( \frac{\partial \sigma}{\partial w_{TS}} \right)^2 V_{w_{TS}} \\ + \left( \frac{\partial \sigma}{\partial t_{TS}} \right)^2 V_{t_{TS}} + \left( \frac{\partial \sigma}{\partial l_{LC}} \right)^2 V_{l_{LC}} , \quad (G5)$$

where

$$\frac{\partial \sigma}{\partial E_{LC}} = \frac{t_{LC} w_{LC}^3 \delta_{LC}}{w_{TS} t_{TS} l_{LC}^3} , \quad \frac{\partial \sigma}{\partial t_{LC}} = \frac{E_{LC} w_{LC}^3 \delta_{LC}}{w_{TS} t_{TS} l_{LC}^3} , \quad \frac{\partial \sigma}{\partial w_{LC}} = \frac{3 E_{LC} t_{LC} w_{LC}^2 \delta_{LC}}{w_{TS} t_{TS} l_{LC}^3} , \quad \frac{\partial \sigma}{\partial \delta_{LC}} = \frac{E_{LC} t_{LC} w_{LC}^3}{w_{TS} t_{TS} l_{LC}^3} , \\ \frac{\partial \sigma}{\partial w_{TS}} = - \frac{E_{LC} t_{LC} w_{LC}^3 \delta_{LC}}{w_{TS}^2 t_{TS} l_{LC}^3} , \quad \frac{\partial \sigma}{\partial t_{TS}} = - \frac{E_{LC} t_{LC} w_{LC}^3 \delta_{LC}}{w_{TS} t_{TS}^2 l_{LC}^3} , \text{ and } \frac{\partial \sigma}{\partial l_{LC}} = - \frac{3 E_{LC} t_{LC} w_{LC}^3 \delta_{LC}}{w_{TS} t_{TS} l_{LC}^4} . \quad (G6)$$

The design (nominal) values are used to estimate the partial derivative values, and are listed in Table G1. The estimated standard deviation values are also listed and are described next.

Table G1. Values of parameters used to estimate uncertainty in stress

Parameter	Value	Standard deviation	Units
$E_{LC}$	164000	3200	MPa
$t_{LC}$	7	0.0124	$\mu\text{m}$
$w_{LC}$	9	0.05	$\mu\text{m}$
$l_{LC}$	90	0.05	$\mu\text{m}$
$w_{TS}$	4.4	0.05	$\mu\text{m}$
$t_{TS}$	0.63	0.03	$\mu\text{m}$
$\delta_{LC}$	Variable	0.007	$\mu\text{m}$

The test platform is made from polysilicon with  $E_{LC}=164000$  MPa and standard deviation 3200 MPa [9]. The total load spring thickness is from the combined Poly1, 2, 3 and 4 layers. The

standard deviation for the polysilicon layers can be obtained from SUMMiT V design manual [122]. The standard deviation in thickness is 2.3 nm for Poly1, 3.4 nm for Poly2, 9.9 nm for Poly3 and 6.3 nm for Poly4. Therefore, the standard deviation in thickness is 0.0124  $\mu\text{m}$ . The standard deviation of the width and length of load springs is 0.05  $\mu\text{m}$ . The deflection measurement  $\delta_{LC}$  is within  $\pm 20$  nm accuracy (3 sigma), thus, the standard deviation is 7 nm. The standard deviations for the thickness and width of the tensile specimen are estimated to be 0.03 and 0.05  $\mu\text{m}$  respectively.

Table B2. The contribution of each parameter to the stress variance

Partial derivative	Value	Units	Contribution to stress variance (squared and multiplied by $V_i$ )
$\partial\sigma/\partial E_{LC}$	$0.0025\delta_{LC}$	--	$65.3\delta_{LC}^2$
$\partial\sigma/\partial t_{LC}$	$59.16\delta_{LC}$	MPa/ $\mu\text{m}$	$0.538\delta_{LC}^2$
$\partial\sigma/\partial w_{LC}$	$138.05\delta_{LC}$	MPa/ $\mu\text{m}$	$47.64\delta_{LC}^2$
$\partial\sigma/\partial\delta_{LC}$	414.14	MPa/ $\mu\text{m}$	8.4
$\partial\sigma/\partial w_{TS}$	$-94.12\delta_{LC}$	MPa/ $\mu\text{m}$	$22.148\delta_{LC}^2$
$\partial\sigma/\partial t_{TS}$	$-657.36\delta_{LC}$	MPa/ $\mu\text{m}$	$388.919\delta_{LC}^2$
$\partial\sigma/\partial l_{LC}$	$-13.8\delta_{LC}$	MPa/ $\mu\text{m}$	$0.476\delta_{LC}^2$

The nominal values were substituted in equations G6 and a summary of their respective contributions is listed in Table G2. Note that many of the partials in equations (G6) depend on  $\delta_{LC}$ . Therefore, in general, the error will vary with displacement or strain. Substituting back into equation (G5), the variance of stress can be obtained as function of spring deflection  $\delta_{LC}$ , which can be related to the nominal value of the stress by the equation (G4). The uncertainty in stress is the standard deviation of stress ( $\sigma \pm S_\sigma$ ) and the error is the standard deviation divided by the nominal value (error =  $S_\sigma/\sigma$ ). At low stress values (near zero), the uncertainty in stress is dominated by uncertainty in  $\delta_{LC}$  and the error approaches infinity. As seen in Fig. G1, the

contribution of measurement uncertainty falls as the load cell deflection  $\delta_{LC}$  increases and the uncertainty in the tensile specimen thickness becomes the major source of error. The contributions of  $t_{LC}$ , and  $l_{LC}$  to the error are small. Table G2 shows the contribution of all parameters as function of load spring deflections, while Fig. G1 shows the contribution of load spring width, deflection, Young's modulus and the tensile specimen width and thickness to the total stress uncertainty at different stress levels.

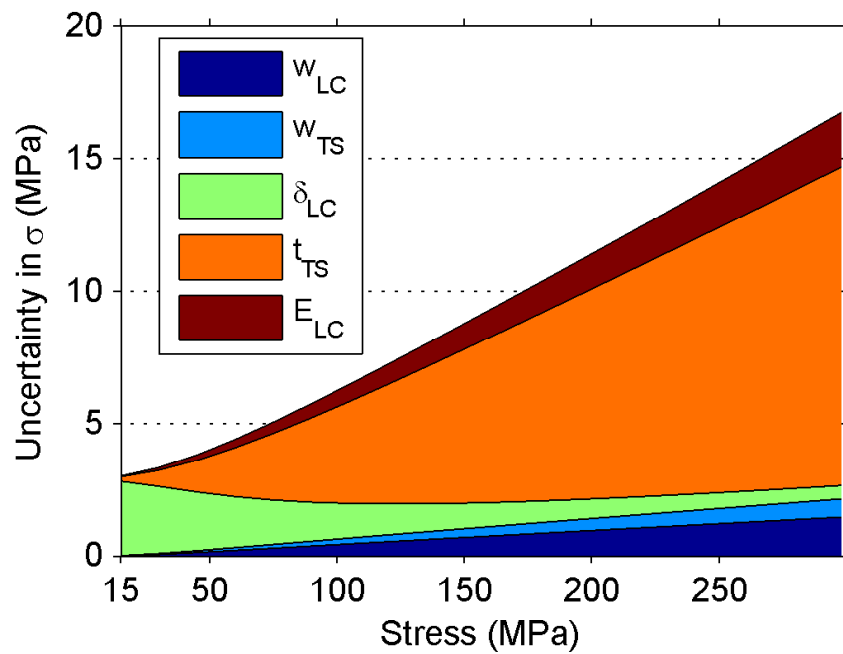


Fig. G1 Contributions of (i) load cell width, deflection and Young's modulus and (ii) tensile specimen width and thickness to the total uncertainty in stress

An important parameter is how the error changes with increased stress. Fig. G2 shows the change in total error as function of load cell deflection. The total error decreases with increasing stress until it flattens out at 5% error at 100 MPa. Therefore,  $\sigma_y$  is expected to be accurate within 5% error.

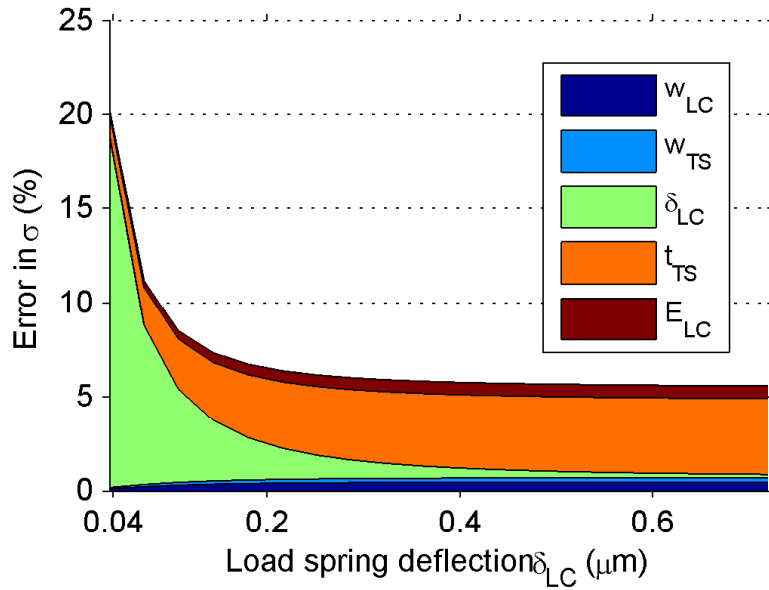


Fig G2 Contributions to total error in stress as function of load cell deflection

### Uncertainty in Strain

Strain can be expressed as

$$\varepsilon = \frac{\delta_{TS}}{L_{TS}} \quad , \quad (G6)$$

where  $\delta_{TS}$  is the deflection of the tensile specimen and  $L_{TS}$  is the length of the tensile specimen.

The deflection measurement has standard deviation of 7 nm. Assuming a uniform etching to the tensile specimen, then the gauge length of tensile specimen remains the same and the only change happens to the tensile specimen is the increase in fillet radius, therefore, the standard deviation in the length of tensile specimens can be assumed to be zero. Thus, the strain variance can be expressed as

$$V_{\varepsilon} = \left( \frac{\partial \varepsilon}{\partial \delta_{TS}} \right)^2 V_{\delta_{TS}} \quad , \quad (G7)$$

where

$$\frac{\partial \varepsilon}{\partial \delta_{TS}} = \frac{1}{L_{TS}} .$$

Substituting the nominal value of the length ( $L_{TS} = 50 \mu\text{m}$ ) in equation (G7) results in a variance of  $1.96 \cdot 10^{-8}$  or standard deviation of  $S_E = 0.00014$ , therefore the error in strain ( $S_\varepsilon/\varepsilon$ ) is expected to be large at low values of strain and the error diminishes towards zero as the strain increases. For example at  $\varepsilon = 0.01$  (1%), the strain error is already  $< 2\%$ .

### Uncertainty in Young's modulus

In a similar manner, Young's modulus of tensile specimen and the variance of Young's modulus can be expressed as

$$E = \frac{\sigma}{\varepsilon} \quad (\text{G8})$$

$$V_E = \left(\frac{1}{\varepsilon}\right)^2 V_\sigma + \left(-\frac{\sigma}{\varepsilon^2}\right)^2 V_\varepsilon \quad (\text{G9})$$

In a previous study, Young's modulus was found to be 74.4 GPa [91]. Therefore, the nominal stress values and nominal strain values that produce Young's modulus of 74.4 GPa was substituted in equation (B9). Fig. G3 shows the uncertainty in Young's modulus as function in percentage of strain.

The linear part of the stress-strain curve spans over a range of  $\sim 0.003$  as shown in Fig. 9. The Young's modulus was estimated within the strain region  $\varepsilon = 0.0002 - 0.003$ . If strain values less than 0.0002 included in the determination of Young's modulus, then the error approaches infinity and unreliable result is obtained.

The average uncertainty in Young's modulus can be calculated as

$$\bar{S}_E = \sqrt{\frac{\int_{\varepsilon_1}^{\varepsilon_2} S_E^2 d\varepsilon}{(\varepsilon_2 - \varepsilon_1)}} \quad (\text{B10})$$

Numerical integration of equation (B10) was performed where the variables of integration are taken from Fig. B3 over the strain range  $\varepsilon = 0.02\text{-}0.3\%$  and the uncertainty in Young's modulus was found to be  $\bar{S}_E = 15.6 \text{ GPa}$ .

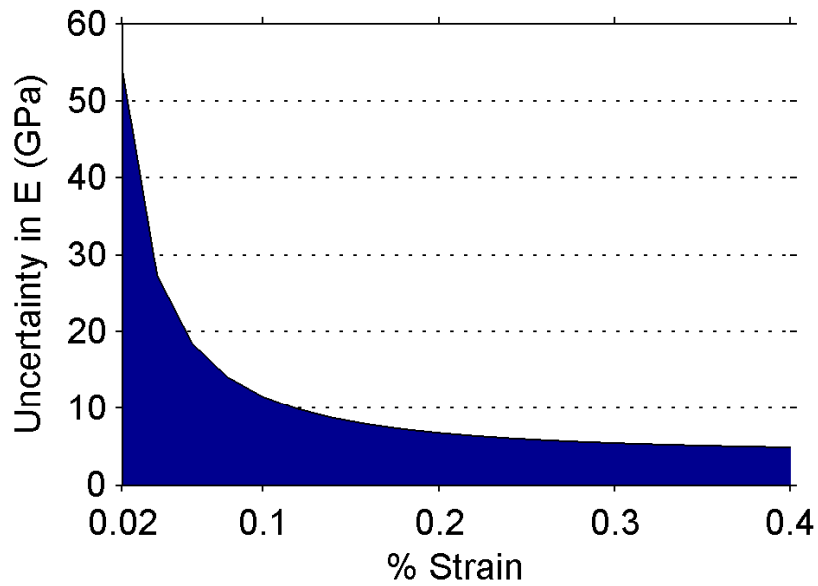
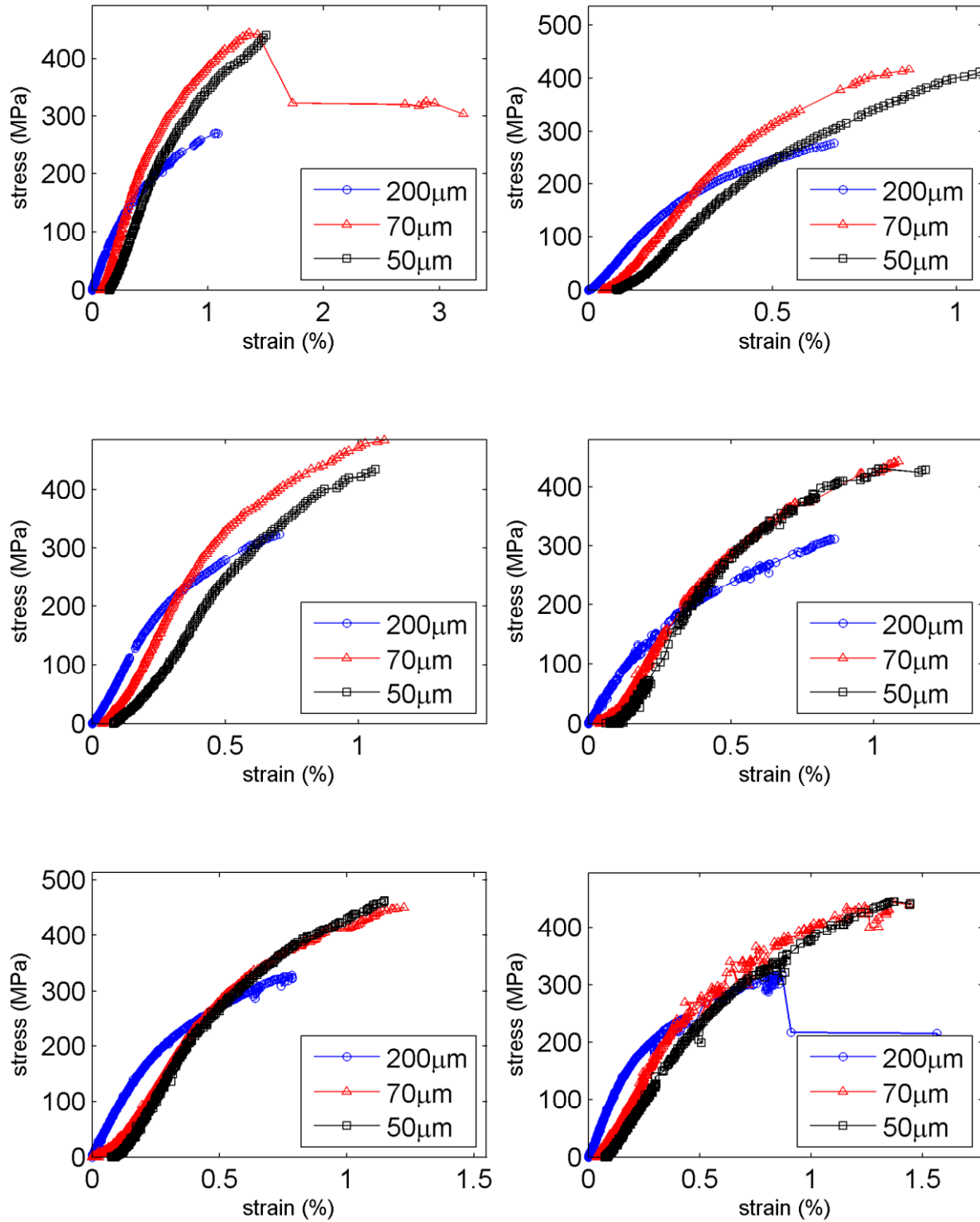


Fig G3 Uncertainty in Young's modulus as function of strain percentage

# Appendix H: Stress vs strain curves for different specimens

Fig H-1 Stress –strain curves for  $t = 0.63 \mu\text{m}$  specimens



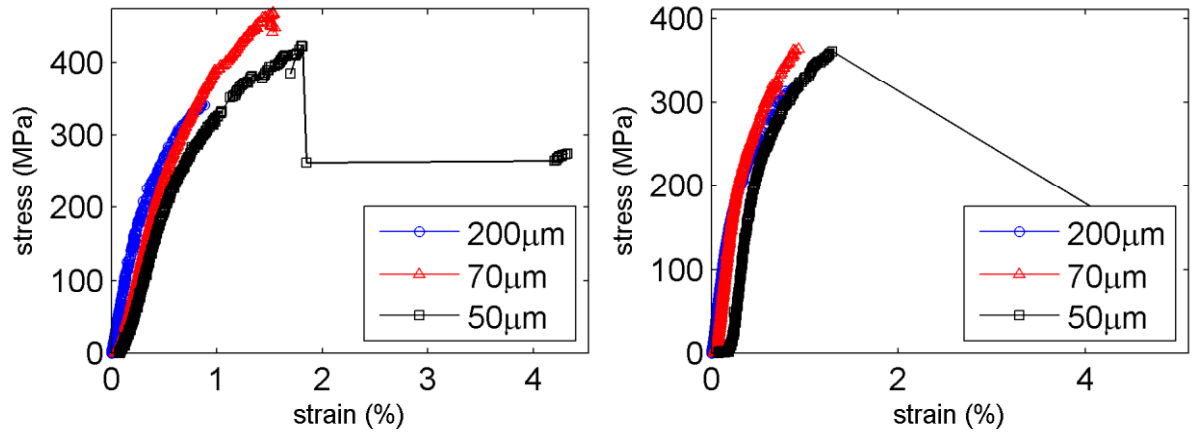
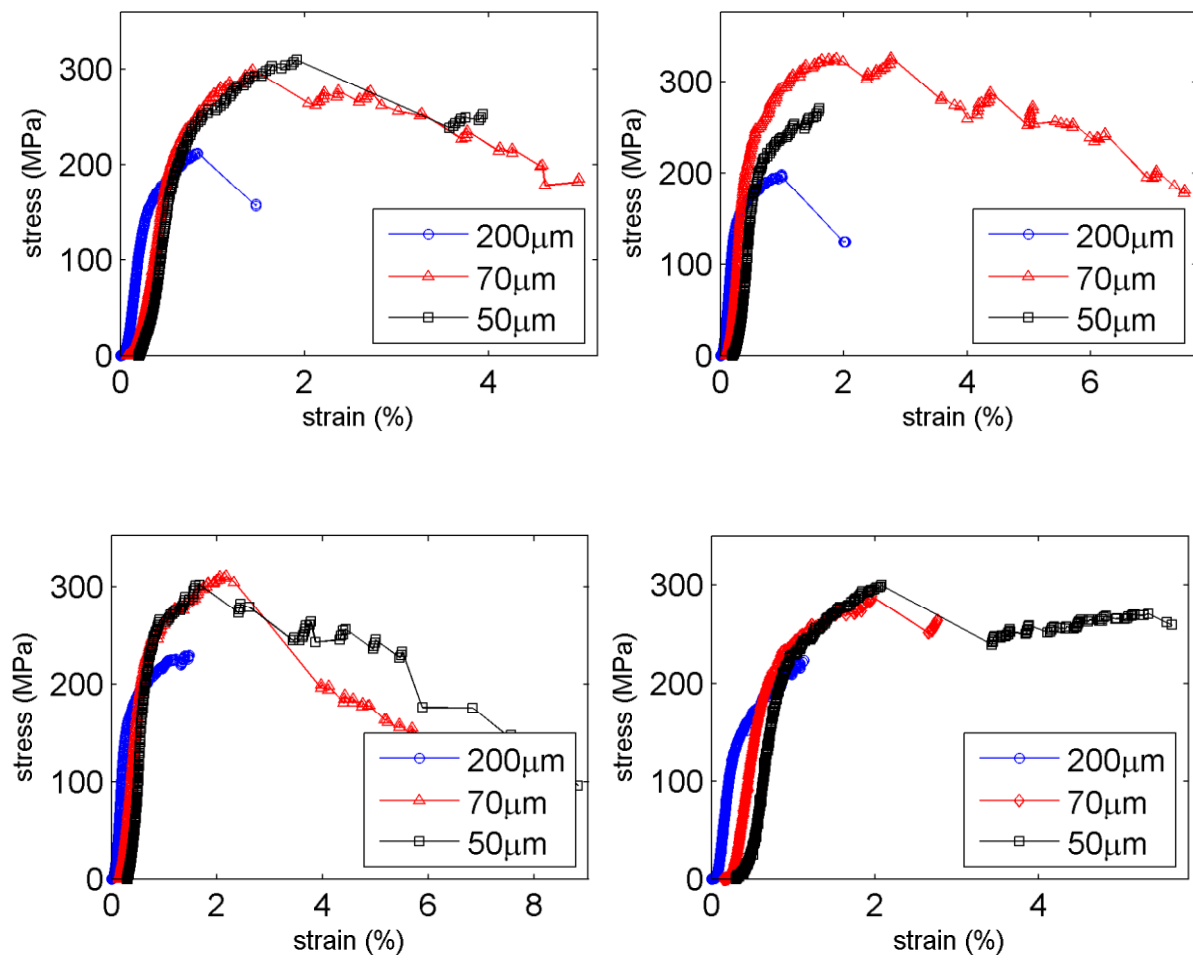
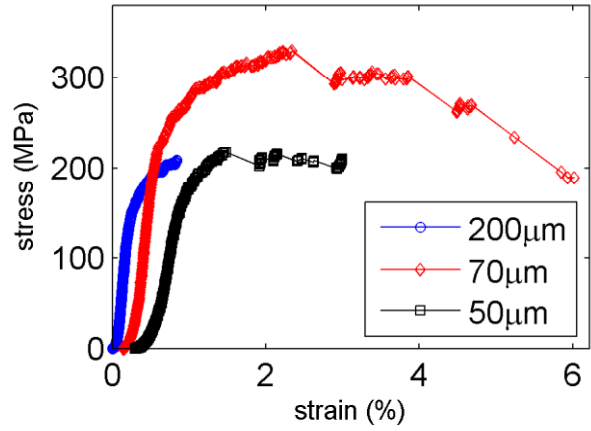
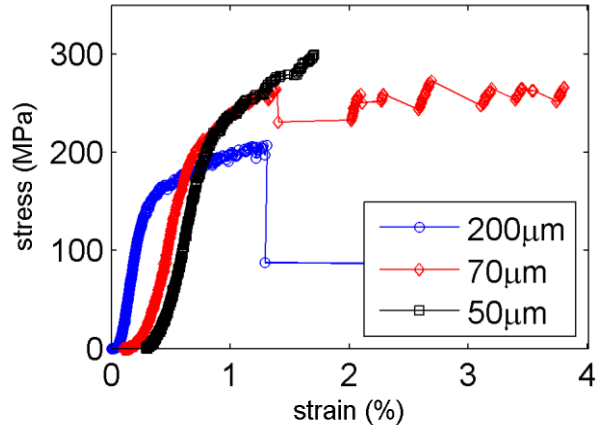
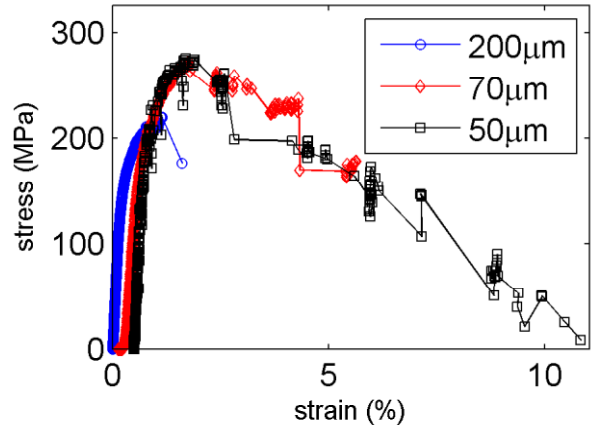
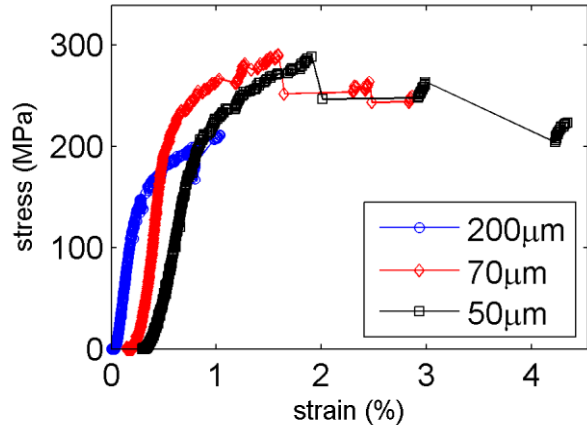


Fig H-2 Stress –strain curves for  $t = 1.03 \mu m$  specimens





## Appendix I: Preliminary Creep Experiments

Preliminary creep tests were performed on the probe station. Fig. II shows the aluminum tensile bar displacement and the force displacement recorded at the load cell. The experiment was performed in air at 157 °C. The high noise observed in the measurement may be associated to the air convection current generated by the large heat. For better results, the specimens should be tested on vacuum chamber like the one that used in [101], [123]

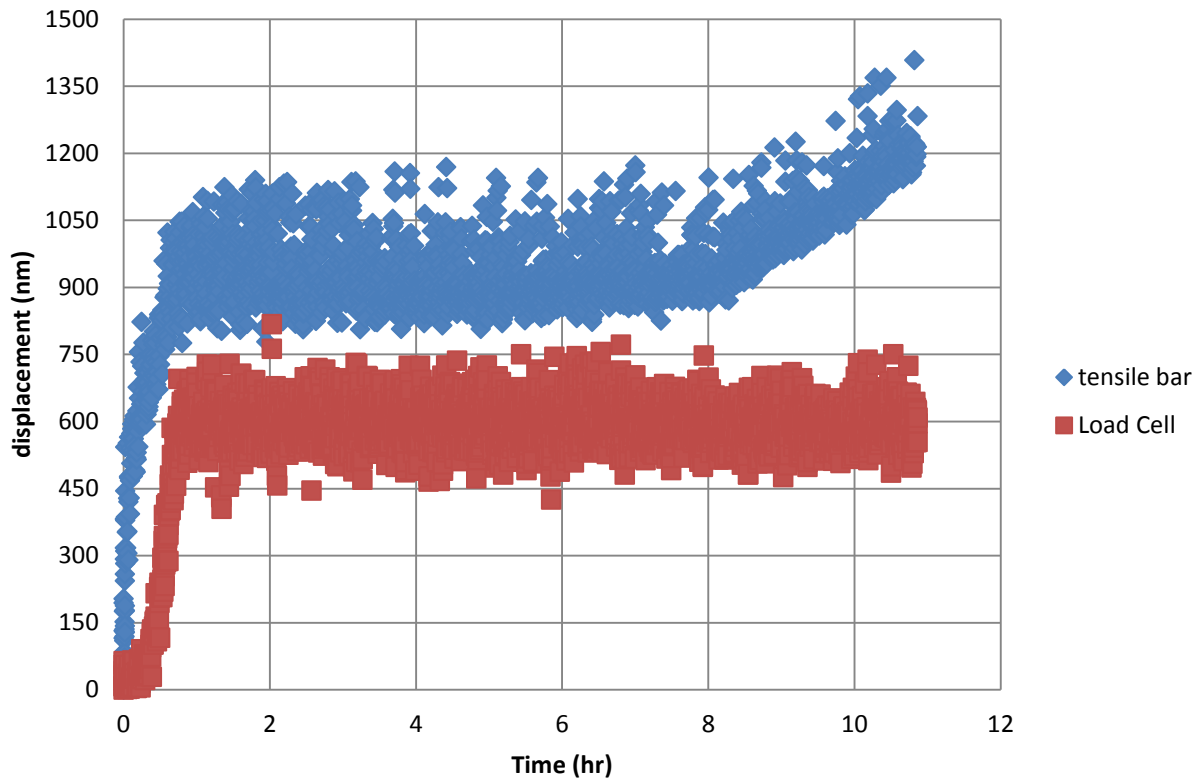


Fig II Creep experiment at 157 °C

## Appendix J: Monte Carlo Simulation

In this Appendix, we are going to attempt to demonstrate an approach for describing and predicting the strength of brittle materials. The approach is based on the idea of the weakest link that Weibull has developed; however, we will go in a different direction. Weibull assumed that failure can happen anywhere along the surface area but in fact that is not completely true. In reality, failure can only happen at the locations where we have severe flaws. Therefore, instead of using a chain with an infinite number of links (infinite number of flaws), we should use a chain with specific number of links (or links with finite volumes) and each link contains only one flaw that could cause the failure of the whole structure.

Thus, a Monte Carlo approach has been developed for the treatment of strength distribution of brittle materials. The approach relies on generating random representative volume elements (RVEs) and assigns a flaw size to each element. The relation between flaw size and (RVEs) is assumed to be described by a power law function. Linear fracture mechanics treatment was utilized to develop our Monte Carlo scheme. The Monte Carlo approach then used to fit  $S_p 1$  (the 70  $\mu\text{m}$  long) experimental data and the curve fit was used to predict specimen size effect. Finally, the effect of the number of specimens on the accuracy of strength distribution is discussed. A small number of specimens gives a poor representation of strength distribution of brittle materials and a large number of specimens should be tested to get reliable and accurate results. The Monte Carlo simulation can easily be used to predict the minimum number of specimens that should be tested to obtain a reliable and accurate strength distribution curve.

There are some unconventional approaches that were used to study the strength distribution of brittle materials such as the fuse network model [124], [125] where a network of electrical

resistances are considered to be analogous to a mechanical structure with flaw. This approach has yet to be validated experimentally. Another approach which surprisingly is not more widely used in spite of its simplicity and widespread applicability is the Monte Carlo simulation. The Monte Carlo simulation has been used to hypothesize a deviation from the Weibull distribution for a small number of samples by generating virtual strength data from a pre-assumed Weibull function [72]. Another interesting use of the Monte Carlo simulation to study brittle materials size effect was reported by Nurhuda et al. [126]. They assumed a Poisson distribution of flaw sizes in glass plates under uniform pressure and tested the effect of the flaw size using four different distributions (uniform, normal, log-normal and Weibull distributions). They found that the log-normal produced a better curve fit to their experimental data. Yankelevsky [127] used a similar approach and shows that the fracture location can be predicted as well.

In the next sections, we will explain in detail our new Monte Carlo simulation that can be used for any brittle material; then we will utilize it for our specific case in predicting size effect of polysilicon.

## **J.1 Model Derivation for Uniform Specimens**

Let us assume a uniform tensile bar with length  $L$  and cross sectional area  $A$  is experiencing a uniform tensile stress as is shown in Fig. J.1 (a). The tensile bar can be divided into a chain of small RVEs as shown in Fig. J.1 (b). Each RVE has a length  $l_i$  and cross sectional area  $A$ . The RVE notion was introduced by Bazant et al. [128], [129] and it can be defined as the smallest volume element whose failure will lead to the failure of the whole structure. The representative volume element is analogous to the chain link in the Weibull theory. We will assume that the

RVEs volumes are not constant and the volume of each RVE depends on the flaw size. Small RVEs have small size flaws and big RVEs have large size flaws.

For a uniform tensile bar with  $N$  number of RVEs and each RVE has length of  $l$ , the total length can be expressed as

$$L = \sum_{i=1}^N l_i \quad (J.1)$$

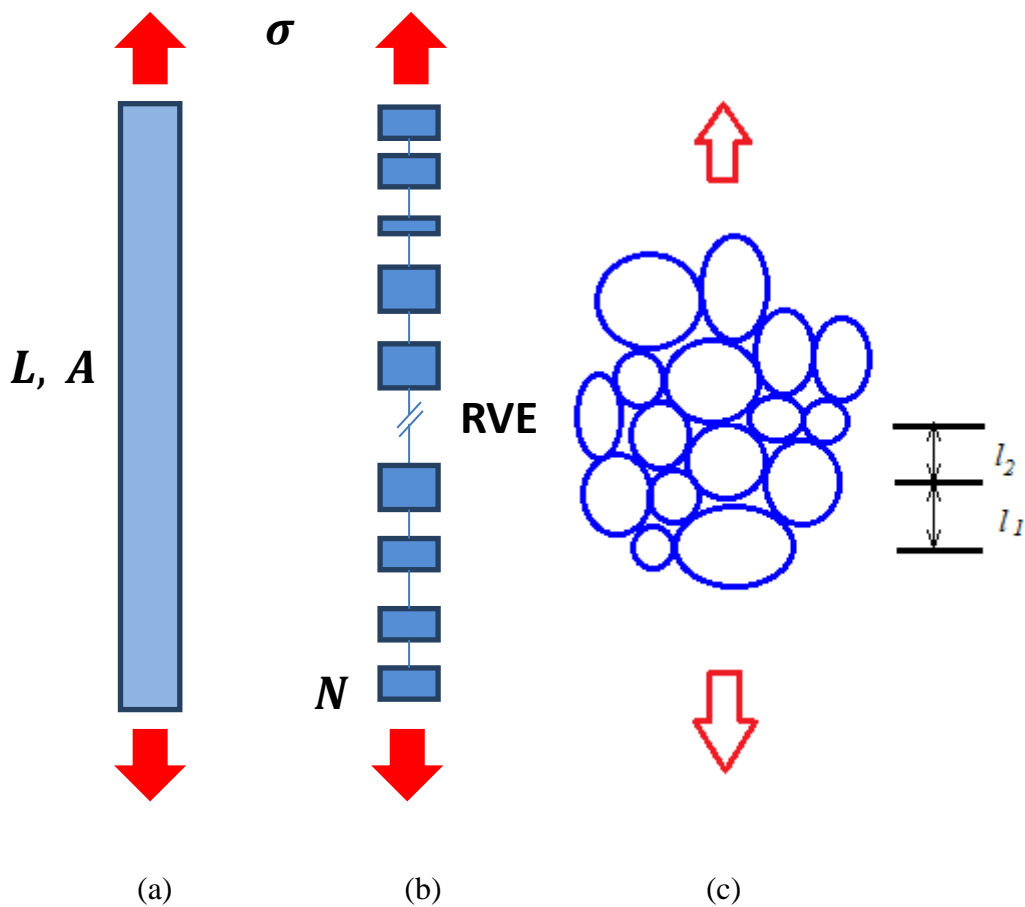


Fig. J.1 The construction of RVEs (a) Uniform tensile bar loading (b) Representative volume elements (RVEs) (c) The choice of the length of RVEs ( $l_i$ )

Each RVE will be assumed to have the same number of grains and the length of the RVE ( $l_i$ ) is the average grains diameters ( $l_i \sim O(d)$ ) as shown in Fig J.1c. Thus, if the grain size has a certain

probability distribution  $f(\psi)$ , whether this distribution is discrete or continuous, the length of the RVE is expected to follow the Gaussian distribution based on the Central Limit Theorem.

The length of the RVE, ( $l_i$ ) does not go to zero and does not go to infinity, the length is rather confined between two limits  $l_{min}$  and  $l_{max}$ . This limit is related to the limit of the grain diameter as  $l_{min} \sim d_{min}$  and  $l_{max} \sim d_{max}$ . Therefore, the distribution of  $l_i$  can be expressed as

$$f(l) = \frac{1}{\lambda\sqrt{2\pi}} \text{Exp}\left(-\frac{(l-l_o)^2}{2\lambda^2}\right) \quad l_{min} \leq l \leq l_{max} \quad (\text{J. 2})$$

The fracture of brittle materials is caused by crack like flaws. Therefore, we can assume that each RVE contains flaw in a form of a crack. These cracks have different sizes and different orientations as shown in Fig J.2. The orientation of the crack can take any value from  $-\pi/2 \leq \theta \leq \pi/2$ . But from symmetry (crack oriented at angle  $\theta$  is similar to crack oriented at angle  $-\theta$ ), the orientations of crack can be assumed to be from 0 to  $\pi/2$  and all orientations are equally likely, thus the probability density function for the orientation can be expressed as

$$f(\theta) = \frac{2}{\pi} \quad 0 \leq \theta \leq \pi/2 \quad (\text{J. 3})$$

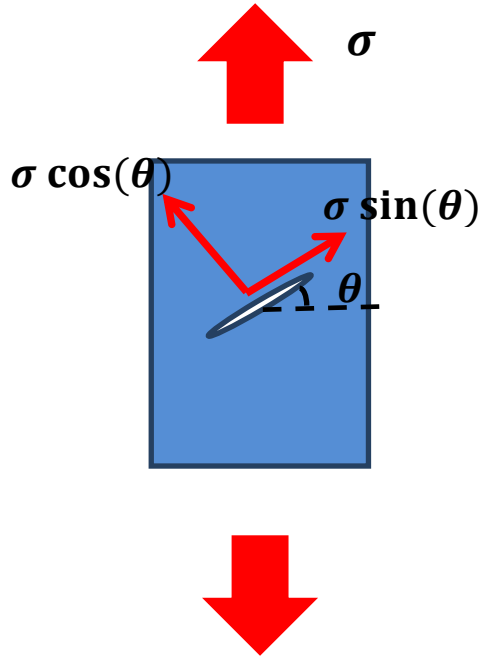


Fig J.2 Crack orientation in RVE

The stress on the crack face can be resolved to two components, a perpendicular component which has the value of  $\sigma \cos(\theta)$  and a parallel component which has the value  $\sigma \sin(\theta)$ . The perpendicular component of stress is the load that causes fracture while the parallel component has no role in fracture. From linear fracture mechanics (LFM), failure happens when the stress intensity factor of a certain crack length reaches a critical value  $K_{Ic}$  [130]. Thus,

$$K_{Ic} = Y\sigma\cos(\theta)\sqrt{\pi a} \quad (J.4)$$

Where,  $Y$  is the shape factor which depend on the crack shape

$Y = 1$  for long interior crack,  $Y = 1.122$  for surface crack,  $Y = 0.713$  for penny shaped crack

Each RVE has a specific flaw size. The change in crack size with the length of the RVE is not known. But, we have already assumed that larger RVEs have larger crack size, while smaller RVEs have smaller crack size. Therefore, the crack size distribution should be a monotonic

increasing function with respect to the RVE length. For simplicity, we will assume the distribution of flaw size to be a power law function which can be expressed as

$$a = c \left( \frac{l}{l_o} \right)^m \quad (J.5)$$

Where  $l_o$  is the mean length of the RVEs and  $c$  is the crack length of the mean RVE.

Substituting equation (J.5) into (J.4) and rearranging the parameters we get a simple equation that relates the strength to the length of RVE.

$$\sigma \cos(\theta) = \frac{G}{l^n} \quad (J.6)$$

Where  $G$  and  $n$  are constants, have the values of  $G = \frac{K_{Ic}}{Y\sqrt{\pi c/l_o}}$  and  $n = m/2$

For the average length of the RVE  $l_o$ , the fracture strength is  $\sigma_o$ . Thus, equation (J.6) can be expressed in a simple form as

$$\frac{\sigma \cos(\theta)}{\sigma_o} = \left( \frac{l_o}{l} \right)^n \quad (J.7)$$

Equation (J.7) describes how the strength changes with the length of the RVEs. For simplicity we will assume all cracks are perpendicular to the loading direction which represents the most severe case. Thus,  $\theta = 0$  and equation J.7 can be rewritten as

$$\frac{\sigma}{\sigma_o} = \left( \frac{l_o}{l} \right)^n \quad (J.8)$$

Based on Equations (J.1), and (J.8) combined with the suggested normal distribution for the  $l_i$  and the uniform distribution for  $\theta$ , we can establish a Monte Carlo approach that enables us to numerically fit the strength distribution data and determine the material constants  $\sigma_o, c$  and  $n$ .

Knowing these constants at a certain length scale we can use these values to determine the strength distribution at other length scales (these are material constants and do not depend on size). To determine these materials constants, we have to perform what we call, “computer experiments”. The computer experiments rely on generating a virtual tensile bar by generating random RVEs sampled from the Gaussian distribution until we populate the whole length of the tensile bar. We then break the virtual tensile bar by identifying the weakest RVE and the corresponding strength can be identified. The approach can be summarized in the following steps

- 1) Values for the material constants  $\sigma_o$  and  $n$  are assumed.  $\sigma_o$ : is the reference value of strength at reference length of  $l_o$ . In our calculations we chose the reference strength to be at the mean RVE length.
- 2) RVEs are randomly generated (random values are taken from the Gaussian distribution) with length of the order of grains size until the total length of the tensile bar is generated. (The maximum and minimum grain size should be known from the fabrication process; therefore, we generate random volumes with length  $l_i$  until the summation of all lengths equal to the required length. Eq. J.1)
- 3) A random value for the orientation of the crack is taken from the uniform distribution (Eq. J.3)
- 4) The weakest RVE then identified (the largest volume) and the strength value is calculated by equation (J.8)
- 5) Randomly generate another tensile bar and test it by repeating steps 2 to 4
- 6) This process is repeated until we get a sufficient strength statistical data
- 7) The strength data is sorted in ascending order and the rank probability for each value is calculated by the equation

$$P_i = \frac{i - 0.5}{n} \quad (J.9)$$

- 8) Strength vs. probability plot is constructed and the curve from the Monte Carlo simulation is compared with the actual test results obtained from lab tests. (Basically, a numerical curve fitting is performed where the results from the Monte Carlo simulation are fitted to an actual test results from the lab)
- 9) If the Monte Carlo simulation results does not fit the data, different values for  $\sigma_o$  and  $n$  are chosen and steps 2-8 are repeated until the Monte Carlo simulation fit the actual experimental data.

Fig J.3 summarizes the Monte Carlo simulation steps

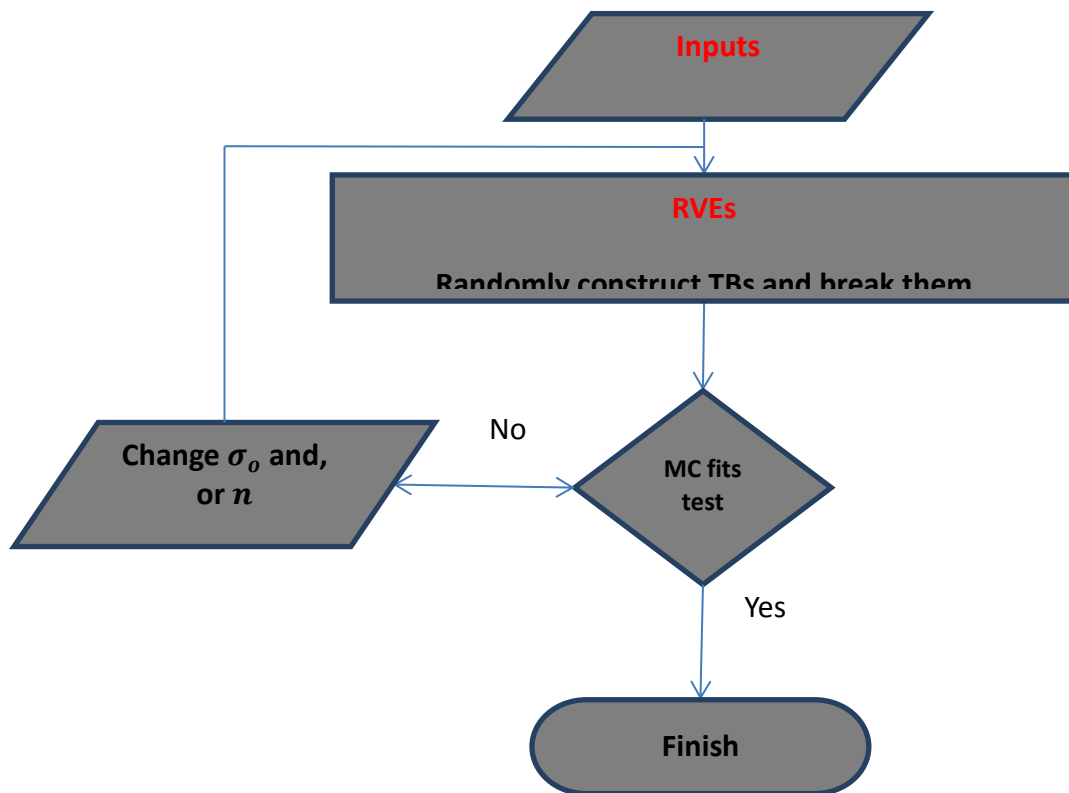


Fig J.3 Monte Carlo Approach

The constants  $\sigma_o$  and  $n$  that are established from the above steps do not depend on size. Therefore, to study size effect we use the same materials constants at the required size scale. Basically, we populate a tensile bar at the required size scale, use the materials constants with equation (J.8) to estimate strength value, and repeat the process until we gather sufficient strength data, then we construct the strength probability curve.

The above approach was used to fit our experimental data and estimate the material constants for Specimen 1 (70  $\mu m$  tensile bars). We have used 1000 virtual tensile bars for the numerical curve fit. The materials constants were used to predict the strength distribution for Specimen 2 (7  $\mu m$  tensile bars).

The grain sizes for the SUMMiT IV process are in the range of 0.2-0.6  $\mu m$ , with average grain size of 0.4  $\mu m$  [17]. A Gaussian distribution was constructed for  $l_i$  between 0.2-0.6. Then the computer experimentation steps were performed on Specimen 1 until a satisfactory agreement was established between computer results and actual test data as shown in Fig. J.4. The material constants were  $l_o = 0.4 \mu m$ ,  $\sigma_o = 4.7 \text{ GPa}$  and  $n = 1.85$ . These materials constants were used to predict the strength distribution for Specimen 2 and the prediction agrees very well with the actual experimental results as shown in Fig. J.5.

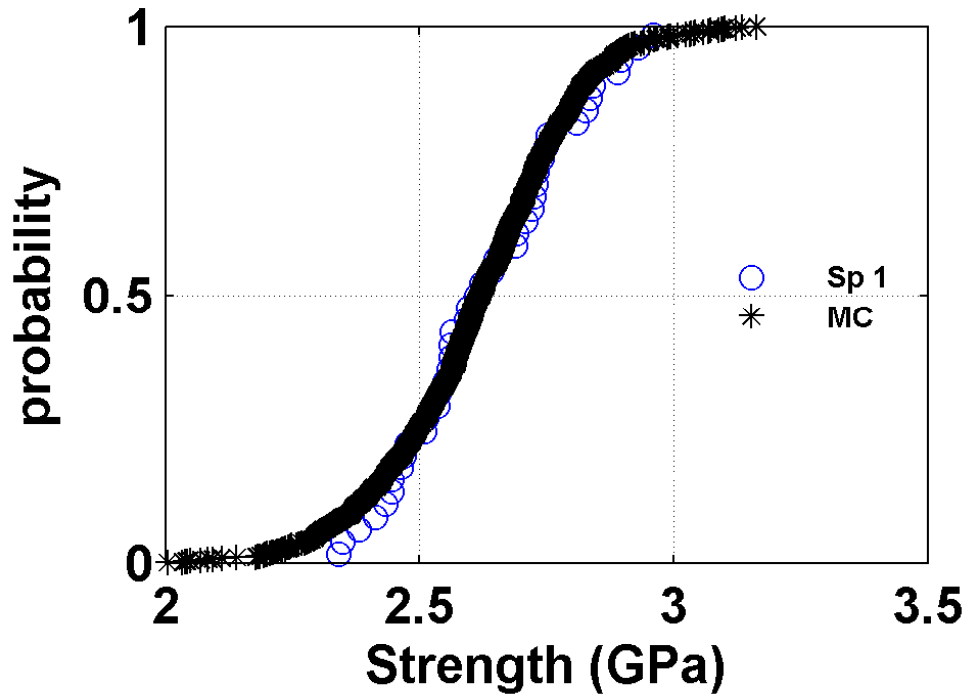


Fig. J.4 Fitting specimen 1 experimental results with 1000 data points from MC simulation

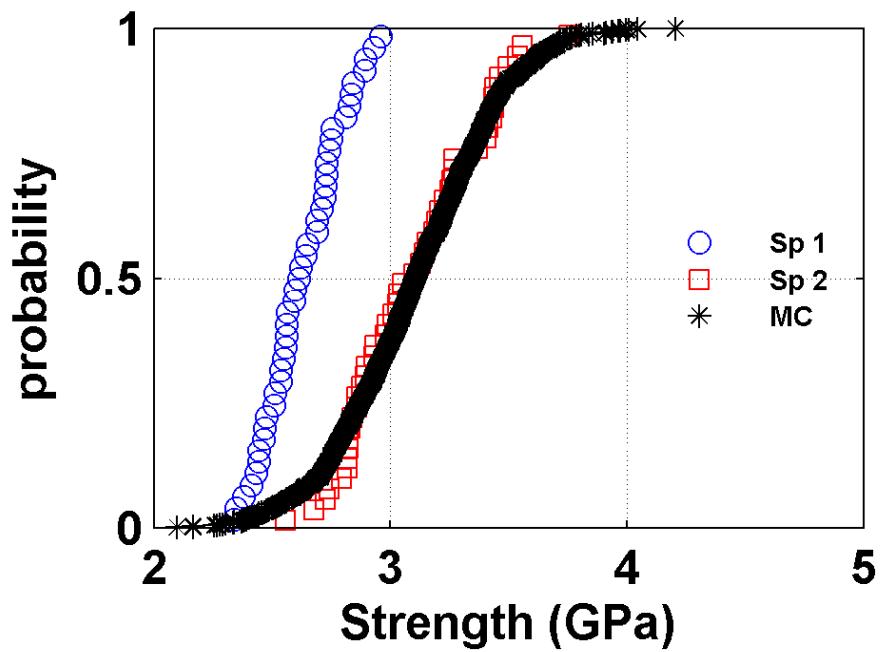


Fig J.5 Predicting Specimens 2 strength distribution by 1000 data points from MC simulation

## J.2 Model Derivation for DEN Specimens

Similarly, to derive our approach for DEN specimens, the notched region is divided to RVEs as shown in Fig J.6. For simplicity, we will assume that the crack flaws are located on the sidewall area and the cracks are perpendicular to the loading direction. Therefore, the stress decreases rapidly along the crack faces and if the crack faces are small compared to the width, then the stress can be assumed to decrease linearly along the crack face as shown in Fig J.4 b. This linearity can be quantified by finite element analysis.

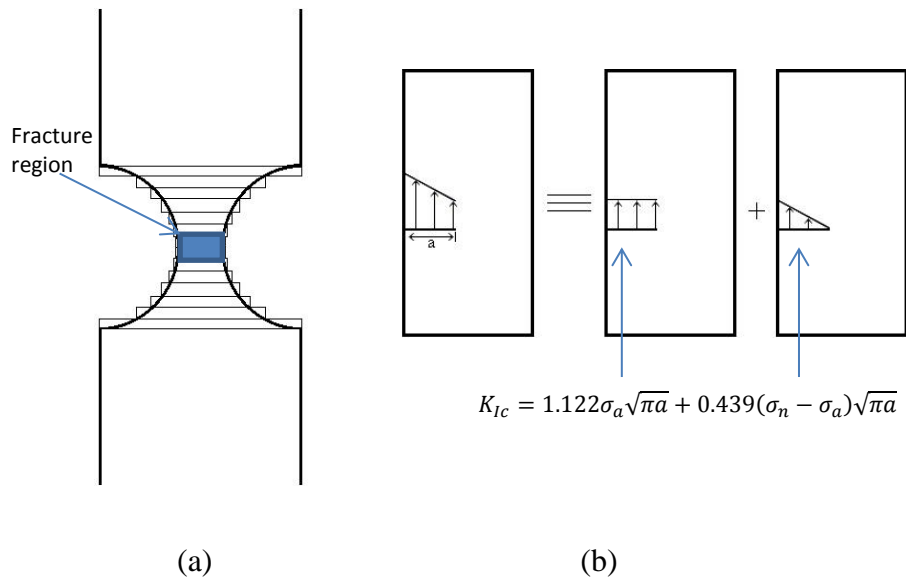


Fig. J.6 DEN specimens (a) RVE (b) LFM modeling to the problem

The fracture happens when the stress intensity factor reaches a critical value and from LFM, the stress intensity factor can be expressed as [130]

$$K_{Ic} = 1.122\sigma_a\sqrt{\pi a} + 0.439(\sigma_n - \sigma_a)\sqrt{\pi a} \quad (\text{J.10})$$

Or in other form

$$K_{Ic} = \sigma_n \left( 0.439 + 0.683 \frac{\sigma_a}{\sigma_n} \right) \sqrt{\pi a} \quad (J. 11)$$

Where  $\sigma_a$  is the uniform part of the stress and  $\sigma_n$  is the total stress at the notch root

The ratio  $\sigma_a/\sigma_n$  across the crack length can be obtained from linear finite element and it can be shown that it behaves linearly and expressed as

$$\frac{\sigma_a}{\sigma_n} = 1 + slope * a \quad (J. 12)$$

Substituting back into equation (J.11) we get

$$K_{Ic} = \sigma_n (1.122 + 0.683 * slope * a) \sqrt{\pi a} \quad (J. 13)$$

The DEN specimens fail at the same stress intensity factor as the uniform ones. Thus from equations (J.4) and (J.13), the fracture stress for DEN specimens can be estimated from the fracture stress of uniform specimens as

$$\sigma_n = \frac{1.122\sigma}{1.122 + 0.683 * slope * c * (l/l_o)^{2n}} \quad (J. 14)$$

Equation (J.14) in conjunction with the knowing materials constants and the random Gaussian distribution for  $l_i$  are the basis of our strength prediction approach for DEN specimens. The steps for predicting strength distribution for DEN specimens can be summarized as

- 1) RVEs for DEN specimens are constructed from the Gaussian distribution
- 2) Equation (J.8) is used to determine  $\sigma$
- 3) Equation (J.14) is used to determine the stress at the notch root
- 4) Repeat steps 1-3 until sufficient statistics data is gathered

These steps were used to predict the strength distribution for specimens 3-5 as shown in Fig J.6

The Monte Carlo approach seems to do a relatively good job at predicting the strength of DEN specimens, especially specimen 5. However, Weibull function does a better job at predicting strength for specimens 4 and 5. The inaccuracy of Monte Carlo approach can be related to many factors such as the assumption of power law distribution to the flaws which might not hold true at small scale specimens.

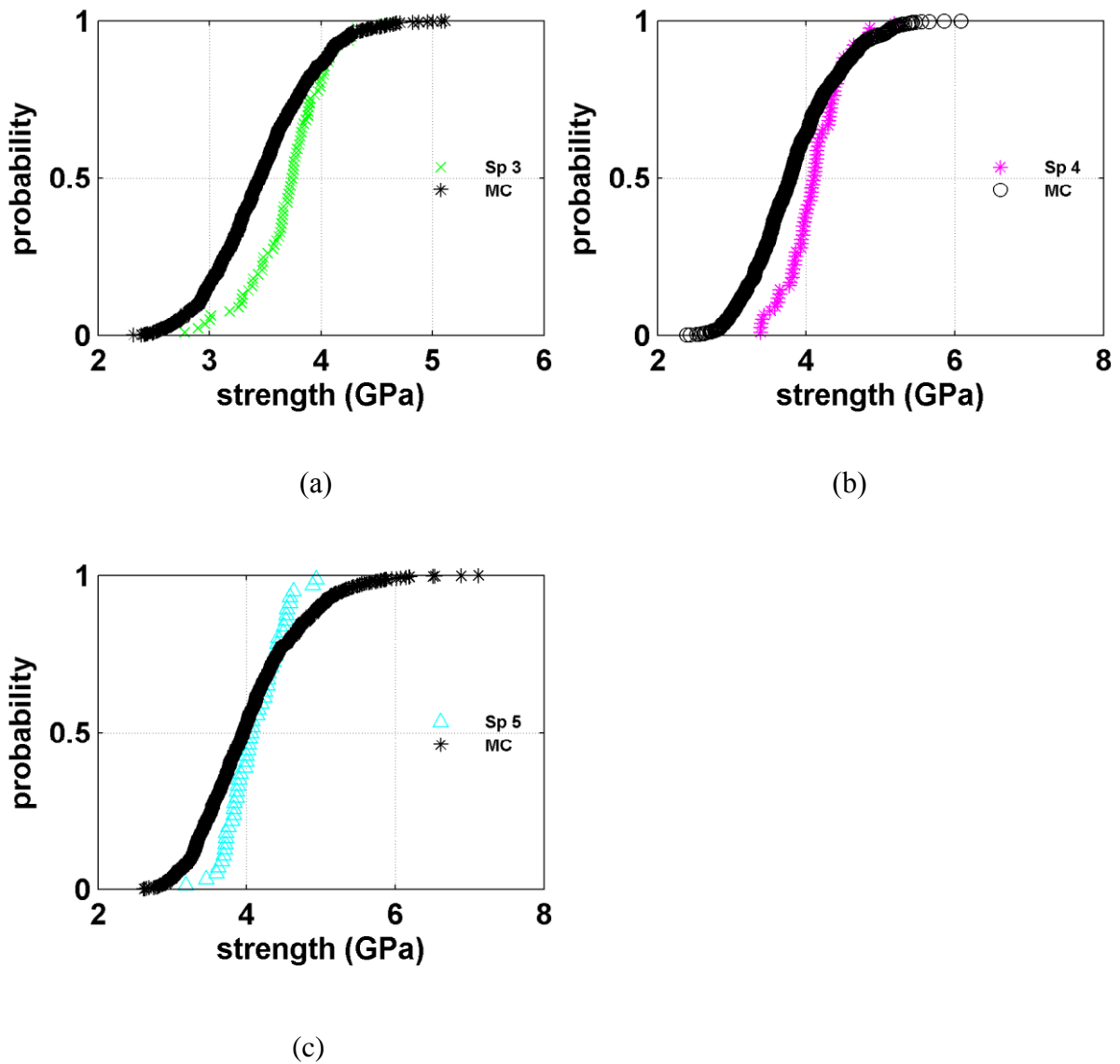


Fig J.6 strength distribution prediction for DEN specimens. (a) Specimen 3 (b) Specimens 4 (c) Specimen 5. The prediction is based on 1000 data points from MC

### J.3 Specimens Number Effect and the Convergence to Unique Curve

The stochastic nature of the fracture in brittle materials requires a large number of tests to get a reliable strength distribution. In this section we will address one of the most important issues that can only be explained and tackled by the Monte Carlo simulation; that being, the number of specimens that should be tested in the physical experiments in the lab.

The power of the Monte Carlo approach lies on the ability to determine the number of minimum physical experiments needed to be performed to get a *unique strength curve*. By a, "*unique curve*," we mean a curve that does not change even if more specimens were tested. To help clarify this concept we will study the effect of the number of specimens on the strength distribution of a hypothetical tensile bar with length  $20 \mu m$  and has material constants of  $\sigma_0 = 3.9 \text{ GPa}$ ,  $n = 1.82$

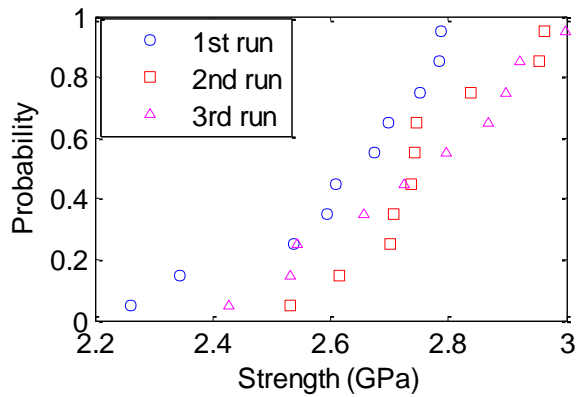
Fig. J.7 (a) shows the results of three different tests of ten virtual specimens from the Monte Carlo simulation. We noticed that there is a big difference between the three curves even though the three curves were generated by using the same material constants; and if the strength data was fitted with Weibull function, different Weibull parameters would be obtained for each curve. Also, the strength distribution is not unique i.e. if we run our Monte Carlo scheme multiple times, we would get different results each time.

Therefore, we can say that using a small number of specimens raises the question of whether the strength distribution is a good representation of the size we are studying or not. Thus, if three different investigators performed physical experimental tests on ten specimens with the same

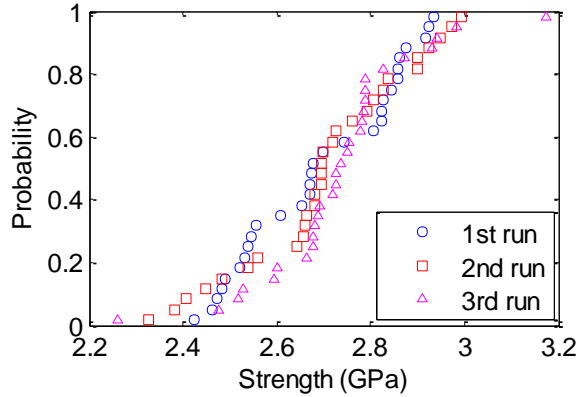
size and from the same material and fabrication process, their strength distribution results most likely would not be the same, even though they are testing the same material.

The strength distribution starts to converge to a specific shape and will have less variability as the number of specimens increase. Fig J.7 (b) shows the Monte Carlo simulation of three different tests of thirty virtual specimens. The strength distribution has less variability between the three runs, but the difference between the three experiments is still significant especially at the low tail region of the plot. Fitting the strength data with Weibull distribution would give a better estimate to the Weibull parameters except for the value of the threshold strength where the variability in strength at the lower tail is still significant. The strength distribution in this case is still not unique considering that when the Monte Carlo scheme is tested multiple times we get a different strength distribution each time. Therefore, once again, if there are three independent investigators and if they performed real physical tests on thirty specimens, each one would most likely have slightly different strength distribution results.

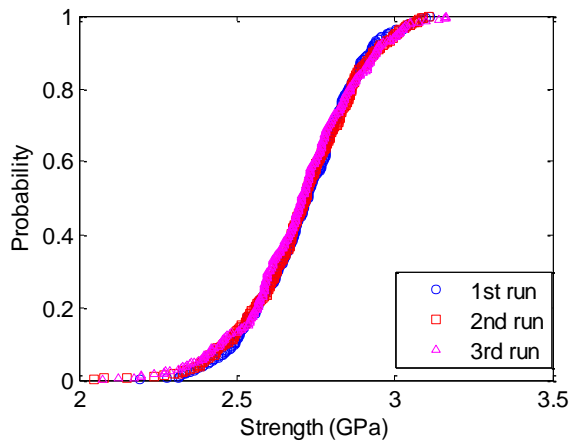
Fig J.7 (c) shows the strength distribution results of 350 virtual specimens at three different runs to our Monte Carlo scheme. It's clear that the three runs almost lie on the top of each other. Here the strength data converges to a unique curve. Even if we were to run the Monte Carlo simulation many more times, the curves would look almost the same. Therefore, we can say that 350 tests should be sufficient to represent the strength of the tensile bar accurately.



(a)



(b)



(c)

Fig J.7 Monte Carlo simulation of hypothetical specimens with length of  $20\mu m$  (a) 10 virtual specimens (b) 30 virtual specimen (c) 350 virtual specimen.

The big advantage to performing a large number of tests is that the low probability tail is characterized and determined more accurately. The low probability tail is important in the design because it is the region where the strength values are the smallest. Fig. J.7 (a, b, c) shows how the low probability tail is well characterized as the number of specimens increase. We have noticed that in increasing the number of specimens greater than 350 will not change the stress

distribution in general, but it might have some effects on slightly extending the low probability tail to smaller strength values.

The Monte Carlo simulation is a simple and cheap approach that can be used to figure out the smallest number of specimens needed to be physically tested in the lab. The simulation can be run multiple times as the number of specimens is increased each time until the strength curve does not change anymore, or it might be used as an approach to estimate uncertainty in the strength distribution.

## Appendix H Analytical Solution for Off Axis Loading of Tensile Bar

In this section, we will discuss a tensile bar under off-axis loading which induce a bending moment. This case is similar to the case of the thin aluminum layer deposited on the top of the poly4 layer. The tensile bar is assumed to be under a moment and axially loaded. For axially loaded beam the vertical deflection governing equation is

$$EI \frac{d^4 y}{dx^4} - P \frac{d^2 y}{dx^2} = 0$$

The general solution of this equation is

$$y = C_1 + C_2 x + C_3 * \text{Exp}(-\eta x) + C_4 * \text{Exp}(\eta x)$$

Where  $\eta^2 = P/EI$

The constants values are determined from the appropriate boundary. The constants are determined for two different boundary conditions, displacement controlled load and force controlled load.

### H.1 Displacement controlled load

The boundary conditions are

$$x = 0, y = 0 \quad x = 0, dy/dx = 0 \quad x = L, y = \delta \quad x = L, dy/dx = 0$$

Applying the above boundary conditions we will get 4 equations in 4 unknowns and these equations where solved for the unknown constants as

$$C_1 = - \left( \frac{R_1 + R_2}{R_1} \right) \frac{\delta}{\zeta}$$

$$C_2 = \eta \left( \frac{R_2 - R_1}{R_1} \right) \frac{\delta}{\zeta}$$

$$C_3 = \frac{R_2}{R_1} \left( \frac{\delta}{\zeta} \right)$$

$$C_4 = \frac{\delta}{\zeta}$$

Where

$$R_1 = 1 - \text{Exp}(-\eta L)$$

$$R_2 = 1 - \text{Exp}(\eta L)$$

$$\zeta = \eta \left( \frac{R_2 - R_1}{R_1} \right) L - 2 \left( \frac{R_2 + R_1}{R_1} \right)$$

The solution of the deflection was solved for different values of axial deflections and Fig.H1 shows the results.

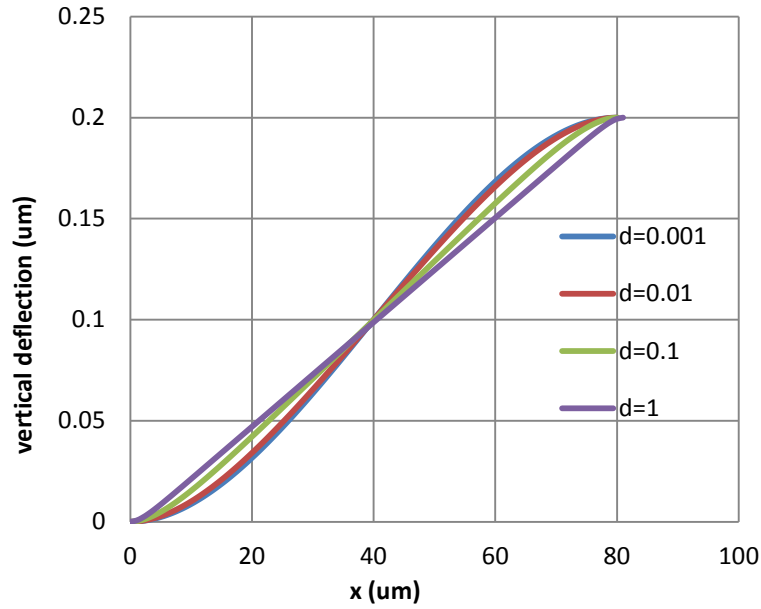


Fig. H1 Tensile bar deflection at different specified axial displacement

The distribution of the moment can be determined from the relation

$$EI \frac{d^2y}{dx^2} = \text{Moment distribution}$$

The moment diagram was plotted for different cases as shown in Figs.H1-3

As the axial deflection increases the moment in the middle region of TB goes to zero

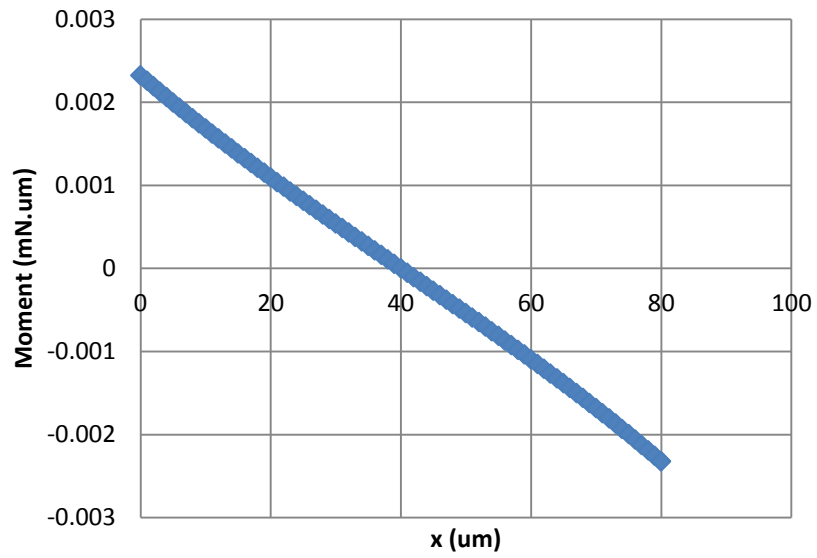


Fig. H2 Bending moment at  $d=0.001 \mu\text{m}$

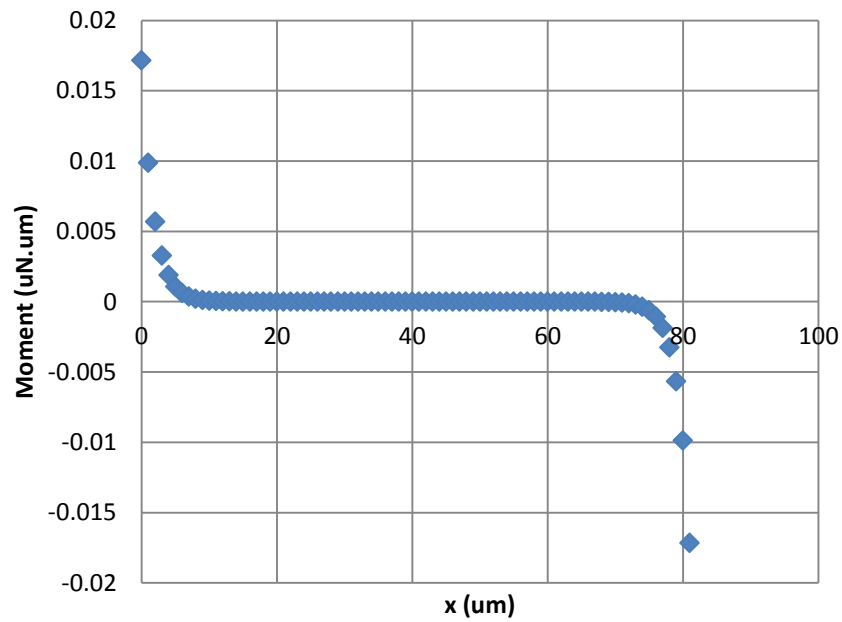


Fig. H3 Bending moment at  $d=1 \mu\text{m}$

### Force controlled load

For force controlled load, the boundary conditions are

$$x = 0, y = 0$$

$$x = 0, dy/dx = 0$$

$$x = L, d^3y/dx^3 - \eta dy/dx = 0 \quad (\text{shear force is zero})$$

$$x = L, \quad EId^2y/dx^2 = M \quad (\text{The moment at the cross head section})$$

Applying the above boundary conditions we will get

$$C_1 = \frac{-2M}{P(\text{Exp}(-\eta L) + \text{Exp}(\eta L))}$$

$$C_2 = 0$$

$$C_3 = \frac{M}{P(\text{Exp}(-\eta L) + \text{Exp}(\eta L))}$$

$$C_4 = \frac{M}{P(\text{Exp}(-\eta L) + \text{Exp}(\eta L))}$$

ANSYS finite element model was created for the tensile bar to compare analytical to finite element results. Different eccentric force was applied in the finite element model and different beam lengths have been tested. The deflection and moment distribution along the tensile bar was extracted from the finite element model and compared with the analytical solution. Both solutions agree very well as shown in Fig.8.

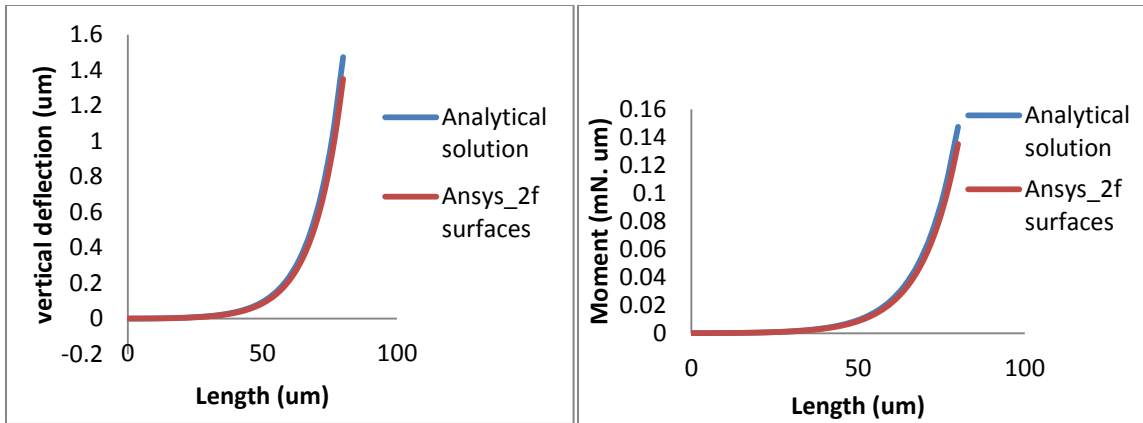


Fig. H4 deflection and moment diagram at  $P=0.1$  mN for 70 um TB

The solution suggested that, the bending moment is small at the region of the tensile bar that connected to the substrate and reaches its highest value at the cross-head section. This implied that most of gauge section of the tensile bar is under axial stress. Therefore, the fillet region should be designed such that the stresses in this region less than the stresses at the gauge section of the tensile bar to ensure that failure only happen at the gauge section.

## References

- [1] T.-R. Hsu, *MEMS & Microsystems: Design, Manufacture, and Nanoscale Engineering*. John Wiley & Sons, 2008, p. 550.
- [2] V. Labhasetwar and D. L. Leslie-Pelecky, *Biomedical Applications of Nanotechnology*. Hoboken, New Jersey, USA: John Wiley & Sons, 2007, p. 272.
- [3] S. X. P. Su, H. S. Yang, and A. M. Agogino, "A resonant accelerometer with two-stage microleverage mechanisms fabricated by SOI-MEMS technology," *IEEE Sens. J.*, vol. 5, no. 6, pp. 1214–1223, Dec. 2005.
- [4] C. Acar and A. Shkel, *MEMS Vibratory Gyroscopes: Structural Approaches to Improve Robustness*. Springer Science & Business Media, 2008, p. 272.
- [5] P. Scheeper and B. Nordstrand, "A new measurement microphone based on MEMS technology," *J. Microelectromechanical Syst.*, vol. 12, no. 6, pp. 880–891, 2003.
- [6] P. F. Van Kessel, L. J. Hornbeck, R. E. Meier, and M. R. Douglass, "A MEMS-based projection display," *Proc. IEEE*, vol. 86, no. 8, pp. 1687–1704, 1998.
- [7] K. Y. Ma, P. Chirarattananon, S. B. Fuller, and R. J. Wood, "Controlled flight of a biologically inspired, insect-scale robot.," *Science*, vol. 340, no. 6132, pp. 603–7, May 2013.
- [8] M. S. Baker, M. P. de Boer, N. F. Smith, L. K. Warne, and M. B. Sinclair, "Integrated measurement-modeling approaches for evaluating residual stress using micromachined fixed-fixed beams," *J. Microelectromechanical Syst.*, vol. 11, no. 6, pp. 743–753, Dec. 2002.
- [9] B. D. Jensen, M. P. de Boer, N. D. Masters, F. Bitsie, and D. a. LaVan, "Interferometry of actuated microcantilevers to determine material properties and test structure nonidealities in MEMS," *J. Microelectromechanical Syst.*, vol. 10, no. 3, pp. 336–346, 2001.
- [10] J. J. Sniegowski and M. P. De Boer, "IC-C OMPATIBLE P OLYSILICON S URFACE M ICROMACHINING," no. 1, pp. 299–333, 2000.
- [11] T. Tsuchiya, O. Tabata, J. Sakata, Y. Taga, and K. Siga, "Specimen size effect on tensile strength of surface micromachined polycrystalline silicon thin films," pp. 529–534, 1997.
- [12] S. Greek, F. Ericson, S. Johansson, M. Fürtsch, and A. Rump, "Mechanical characterization of thick polysilicon films: Young's modulus and fracture strength evaluated with microstructures," *J. Micromechanics Microengineering*, vol. 9, no. 3, pp. 245–251, Sep. 1999.

- [13] J. Ding, Y. Meng, and S. Wen, "Scale dependence of tensile strength of micromachined polysilicon MEMS structures due to microstructural and dimensional constraints," *Chinese Sci. Bull.*, vol. 46, no. 16, pp. 1392–1397, Aug. 2001.
- [14] W. N. Sharpe, B. Yuan, and R. L. Edwards, "A new technique for measuring the mechanical properties of thin films," *J. Microelectromechanical Syst.*, vol. 6, no. 3, pp. 193–199, 1997.
- [15] I. Chasiotis and W. G. Knauss, "The mechanical strength of polysilicon films: Part 2. Size effects associated with elliptical and circular perforations," *J. Mech. Phys. Solids*, vol. 51, no. 8, pp. 1551–1572, Aug. 2003.
- [16] J. Bagdahn, W. N. Sharpe, and O. Jadaan, "Fracture strength of polysilicon at stress concentrations," *J. Microelectromechanical Syst.*, vol. 12, no. 3, pp. 302–312, Jun. 2003.
- [17] B. L. Boyce, J. M. Grazier, T. E. Buchheit, and M. J. Shaw, "Strength Distributions in Polycrystalline Silicon MEMS," *J. Microelectromechanical Syst.*, vol. 16, no. 2, pp. 179–190, Apr. 2007.
- [18] B. L. Boyce, "A Sequential Tensile Method for Rapid Characterization of Extreme-value Behavior in Microfabricated Materials," *Exp. Mech.*, vol. 50, no. 7, pp. 993–997, Sep. 2009.
- [19] E. D. Reedy, B. L. Boyce, J. W. Foulk, R. V. Field, M. P. de Boer, and S. S. Hazra, "Predicting Fracture in Micrometer-Scale Polycrystalline Silicon MEMS Structures," *J. Microelectromechanical Syst.*, vol. 20, no. 4, pp. 922–932, Aug. 2011.
- [20] H.-J. Lee, P. Zhang, and J. C. Bravman, "Tensile failure by grain thinning in micromachined aluminum thin films," *J. Appl. Phys.*, vol. 93, no. 3, p. 1443, 2003.
- [21] M. Coulombier, A. Boé, C. Brugger, J. P. Raskin, and T. Pardoën, "Imperfection-sensitive ductility of aluminium thin films," *Scr. Mater.*, vol. 62, no. 10, pp. 742–745, 2010.
- [22] M. E. Saleh, J. L. Beuth, and M. P. de Boer, "Validated Prediction of the Strength Size Effect in Polycrystalline Silicon Using the Three-Parameter Weibull Function," *J. Am. Ceram. Soc.*, vol. 97, no. 12, pp. 3982–3990, Dec. 2014.
- [23] W. Weibull, "A statistical theory of the strength of materials," *R. Swedish Inst. Eng. Res.*, vol. 151, pp. 1–45, 1939.
- [24] W. Weibull, "A statistical distribution function of wide applicability," *J. Appl. Mech.*, vol. 18, pp. 293–297, 1951.
- [25] J. J. Sniegowski and M. P. de Boer, "IC-COMPATIBLE POLYSILICON SURFACE MICROMACHINING," *Annu. Rev. Mater. Sci.*, vol. 30, no. 1, pp. 299–333, 2000.

- [26] R. W. Hertzberg, R. P. Vinci, and J. L. Hertzberg, *Deformation and Fracture Mechanics of Engineering Materials*, 5th ed. John Wiley & Sons, 2012.
- [27] H. Van Swygenhoven, P. M. Derlet, and a. G. Frøseth, “Nucleation and propagation of dislocations in nanocrystalline fcc metals,” *Acta Mater.*, vol. 54, no. 7, pp. 1975–1983, Apr. 2006.
- [28] a. G. Frøseth, P. M. Derlet, and H. Van Swygenhoven, “Dislocations emitted from nanocrystalline grain boundaries: nucleation and splitting distance,” *Acta Mater.*, vol. 52, no. 20, pp. 5863–5870, Dec. 2004.
- [29] J. Schiotz, F. D. Di Tolla, and K. W. Jacobsen, “Softening of nanocrystalline metals at very small grain sizes,” vol. 391, no. February, pp. 561–563, 1998.
- [30] G. Schoeck, “Frank Read sources in semiconductors,” *Acta Mater.*, vol. 55, no. 6, pp. 2043–2047, 2007.
- [31] D. Hull and D. J. Bacon, *Introduction to Dislocations*. 2001, p. 155.
- [32] E. O. Hall, “The Deformation and Ageing of Mild Steel: III Discussion of Results,” *Proc. Phys. Soc.*, vol. 747, no. B64, 1951.
- [33] N. J. Petch, “The cleavage strength of polycrystals,” *J. Iron Steel Inst.*, vol. 174, p. 1953, 1953.
- [34] R. Venkatraman and J. C. Bravman, “Separation of film thickness and grain boundary strengthening effects in Al thin films on Si,” *J. Mater. Res.*, vol. 7, no. 08, pp. 2040–2048, Jan. 1992.
- [35] J. R. Greer and W. D. Nix, “Nanoscale gold pillars strengthened through dislocation starvation,” *Phys. Rev. B*, vol. 73, no. 24, p. 245410, Jun. 2006.
- [36] J. R. Greer, W. C. Oliver, and W. D. Nix, “Size dependence of mechanical properties of gold at the micron scale in the absence of strain gradients,” *Acta Mater.*, vol. 53, no. 6, pp. 1821–1830, Apr. 2005.
- [37] W. C. Oliver and G. M. Pharr, “An improved technique for determining hardness and elastic modulus using load and displacement sensing indentation experiments,” *Journal of Materials Research*, vol. 7, no. 06, pp. 1564–1583, 1992.
- [38] J. J. Vlassak and W. D. Nix, “A new bulge test technique for the determination of Young’s modulus and Poisson’s ratio of thin-films,” *J. Mater. Res.*, vol. 7, no. 12, pp. 3242–3249, 1992.
- [39] G. Schiltges, D. Gsell, and J. Dual, “Torsional tests on microstructures: two methods to determine shear-moduli,” *Microsyst. Technol.*, vol. 5, no. 1, pp. 22–29, Oct. 1998.

- [40] H.-K. Liu, C. H. Pan, and P.-P. Liu, "Dimension effect on mechanical behavior of silicon micro-cantilever beams," *Measurement*, vol. 41, no. 8, pp. 885–895, Oct. 2008.
- [41] M. F. Ashby, "The deformation of plastically non-homogeneous materials," *Philos. Mag.*, vol. 21, no. 170, pp. 399–424, Feb. 1970.
- [42] M. D. Uchic, D. M. Dimiduk, J. N. Florando, and W. D. Nix, "Sample dimensions influence strength and crystal plasticity.," *Science*, vol. 305, no. 5686, pp. 986–989, 2004.
- [43] H. D. Espinosa, B. C. Prorok, and M. Fischer, "A methodology for determining mechanical properties of freestanding thin films and MEMS materials," *J. Mech. Phys. Solids*, vol. 51, no. 1, pp. 47–67, 2003.
- [44] R. Cragun and L. Howell, "Linear thermomechanical microactuators," *Proc. ASME IMECE MEMS, Nashville, TN*, pp. 181–188.
- [45] L. Que, J.-S. Park, and Y. B. Gianchandani, "Bent-beam electrothermal actuators-Part I: Single beam and cascaded devices," *J. Microelectromechanical Syst.*, vol. 10, no. 2, pp. 247–254, Jun. 2001.
- [46] D. T. Read and J. W. Dally, "A new method for measuring the strength and ductility of thin- films," *Mater. Res.*, vol. 8, no. 7, pp. 1542–1549, 1993.
- [47] W. N. Sharpe, K. T. Turner, and R. L. Edwards, "Tensile testing of polysilicon," *Exp. Mech.*, vol. 39, no. 3, pp. 162–170, Sep. 1999.
- [48] H. Espinosa, B. Prorok, and M. Fischer, "A methodology for determining mechanical properties of freestanding thin films and MEMS materials," *J. Mech. Phys. ....*, vol. 51, pp. 47–67, 2003.
- [49] H. Espinosa, B. C. Prorok, and B. Peng, "Plasticity size effects in free-standing submicron polycrystalline FCC films subjected to pure tension," *J. Mech. Phys. Solids*, vol. 52, no. 3, pp. 667–689, Mar. 2004.
- [50] M. D. Uchic and D. M. Dimiduk, "A methodology to investigate size scale effects in crystalline plasticity using uniaxial compression testing," *Mater. Sci. Eng. A*, vol. 400–401, pp. 268–278, Jul. 2005.
- [51] M. Uchic, D. Dimiduk, J. Florando, and W. Nix, "Sample dimensions influence strength and crystal plasticity," *Science (80-. )*, vol. 637, 2004.
- [52] Y. Zhu, A. Corigliano, and H. D. Espinosa, "A thermal actuator for nanoscale in situ microscopy testing: design and characterization," *J. Micromechanics Microengineering*, vol. 16, no. 2, pp. 242–253, Feb. 2006.

- [53] S. Gravier, M. Coulombier, A. Safi, N. André, A. Boé, J. Raskin, S. Member, and T. Pardoën, “New On-Chip Nanomechanical Testing Laboratory - Applications to Aluminum and Polysilicon Thin Films,” vol. 18, no. 3, pp. 555–569, 2009.
- [54] S. S. Hazra, “HIGH THROUGHPUT, ON-CHIP, IN-SITU INVESTIGATIONS OF STRUCTURAL PROPERTIES OF POLYCRYSTALLINE SILICON FOR MICROELECTROMECHANICAL SYSTEMS,” *PhD Diss.*, 2010.
- [55] M. E. Saleh, J. L. Beuth, and M. P. de Boer, “Validated Prediction of the Strength Size Effect in Polycrystalline Silicon Using the Three-Parameter Weibull Function,” *J. Am. Ceram. Soc.*, vol. 97, no. 12, pp. 3982–3990, Dec. 2014.
- [56] K. H.-L. Chau and R. E. Sulouff, “Technology for the high-volume manufacturing of integrated surface-micromachined accelerometer products,” *Microelectronics Journal*, vol. 29, no. 9, pp. 579–586, 1998.
- [57] J. Wu, G. K. Feeder, and L. R. Carley, “A low-noise low-offset capacitive sensing amplifier for a 50- $\mu\text{g}/\sqrt{\text{Hz}}$  monolithic CMOS MEMS accelerometer,” *IEEE J. Solid-State Circuits*, vol. 39, no. 5, pp. 722–730, 2004.
- [58] J. A. Geen, S. J. Sherman, J. F. Chang, and S. R. Lewis, “Single-chip surface micromachined integrated gyroscope with 50/h allan deviation,” in *IEEE Journal of Solid-State Circuits*, 2002, vol. 37, no. 12, pp. 1860–1866.
- [59] N. A. Hall, M. Okandan, R. Littrell, B. Bicen, and F. L. Degertekin, “Micromachined optical microphone structures with low thermal-mechanical noise levels,” *J. Acoust. Soc. Am.*, vol. 122, no. 4, pp. 2031–2037, 2007.
- [60] I. Chasiotis, S. W. Cho, and K. Jonnalagadda, “Fracture Toughness and Subcritical Crack Growth in Polycrystalline Silicon,” *J. Appl. Mech.*, vol. 73, no. 5, p. 714, 2006.
- [61] J. J. Mecholsky, R. W. Rice, and S. W. Freiman, “Prediction of Fracture Energy and Flaw Size in Glasses from Measurements of Mirror Size,” *J. Am. Ceram. Soc.*, vol. 57, no. 10, pp. 440–443, 1974.
- [62] S. Greek, F. Ericson, S. Johansson, and J.-Å. Schweitz, “In situ tensile strength measurement and Weibull analysis of thick film and thin film micromachined polysilicon structures,” *Thin Solid Films*, vol. 292, no. 1–2, pp. 247–254, Jan. 1997.
- [63] a. McCarty and I. Chasiotis, “Description of brittle failure of non-uniform MEMS geometries,” *Thin Solid Films*, vol. 515, no. 6, pp. 3267–3276, Feb. 2007.
- [64] N. N. Nemeth, L. J. Evans, O. M. Jadaan, W. N. Sharpe, G. M. Beheim, and M. a. Trapp, “Fabrication and probabilistic fracture strength prediction of high-aspect-ratio single crystal silicon carbide microspecimens with stress concentration,” *Thin Solid Films*, vol. 515, no. 6, pp. 3283–3290, Feb. 2007.

- [65] B. Peng, C. Li, N. Moldovan, H. D. Espinosa, X. Xiao, O. Auciello, and J. a. Carlisle, “Fracture size effect in ultrananocrystalline diamond: Applicability of Weibull theory,” *J. Mater. Res.*, vol. 22, no. 04, pp. 913–925, Mar. 2011.
- [66] a. M. Fitzgerald, D. M. Pierce, B. M. Huigens, and C. D. White, “A General Methodology to Predict the Reliability of Single-Crystal Silicon MEMS Devices,” *J. Microelectromechanical Syst.*, vol. 18, no. 4, pp. 962–970, Aug. 2009.
- [67] M. S. Gaither, R. S. Gates, R. Kirkpatrick, R. F. Cook, and F. W. Delrio, “Etching process effects on surface structure, fracture strength, and reliability of single-crystal silicon theta-like specimens,” *J. Microelectromechanical Syst.*, vol. 22, no. 3, pp. 589–602, 2013.
- [68] A. Jaytilaka and K. Trustrum, “Statistical approach to brittle fracture,” *J. Mater. Sci.*, vol. 12, pp. 1426–1430, 1977.
- [69] R. Danzer, P. Supancic, J. Pascual, and T. Lube, “Fracture statistics of ceramics – Weibull statistics and deviations from Weibull statistics,” *Eng. Fract. Mech.*, vol. 74, no. 18, pp. 2919–2932, Dec. 2007.
- [70] A. Zimmermann, E. R. Fuller, and J. Rödel, “Residual Stress Distributions in Ceramics,” *J. Am. Ceram. Soc.*, vol. 82, no. 11, pp. 3155–3160, Dec. 2004.
- [71] S. W. Cho, K. Jonnalagadda, and I. Chasiotis, “Mode I and mixed mode fracture of polysilicon for MEMS,” *Fatigue Fract. Eng. Mater. Struct.*, vol. 30, no. 1, pp. 21–31, Jan. 2007.
- [72] R. Danzer, T. Lube, and P. Supancic, “Monte Carlo Simulations of Strength Distributions of Brittle Materials - Type of Distribution , Specimen and Sample Size Monte Carlo Simulations of Strength Distributions of Brittle Materials - Type of Distribution , Specimen and Sample Size,” vol. 107346, no. 2, 2001.
- [73] S. S. Hazra, M. S. Baker, J. L. Beuth, and M. P. De Boer, “Compact on-chip microtensile tester with prehensile grip mechanism,” *J. Microelectromechanical Syst.*, vol. 20, no. 4, pp. 1043–1053, 2011.
- [74] S. S. Hazra, M. S. Baker, J. L. Beuth, and M. P. de Boer, “Demonstration of an in situ on-chip tensile tester,” *J. Micromechanics Microengineering*, vol. 19, no. 8, p. 082001, Aug. 2009.
- [75] R. D. Wingo, “Maximum Likelihood Estimation of the Parameters of the Weibull Distribution by Modified Quasilinearization,” no. 2, pp. 89–93, 1972.
- [76] N. P. Archer, “Likelihood Estimation With Weibull Models,” no. 1, 1980.

- [77] D. Cousineau, "Fitting the three-parameter weibull distribution: review and evaluation of existing and new methods," *IEEE Trans. Dielectr. Electr. Insul.*, vol. 16, no. 1, pp. 281–288, Feb. 2009.
- [78] R. H. Doremus, "Fracture statistics: A comparison of the normal, Weibull, and Type I extreme value distributions," *J. Appl. Phys.*, vol. 54, no. 1, p. 193, 1983.
- [79] K. Chen, A. A. Ayón, S. Member, X. Zhang, and S. M. Spearing, "Effect of Process Parameters on the Surface Morphology and Mechanical Performance of Silicon Structures After Deep Reactive Ion Etching ( DRIE )," vol. 11, no. 3, pp. 264–275, 2002.
- [80] N. Smirnov, "Table for Estimating the Goodness of Fit of Empirical Distributions," *Ann. Math. Stat.*, vol. 19, no. 2, pp. 279–281, Jun. 1948.
- [81] L. Breiman, *Statistics: With a View Toward Applications*. Boston, MA : Houghton Mifflin, 1973.
- [82] T. W. Anderson, "On the Distribution of the Two-Sample Cramer-von Mises Criterion," *Ann. Math. Stat.*, vol. 33, no. 3, pp. 1148–1159, Sep. 1962.
- [83] A. Brueckner-Foit, P. Huelsmeier, M. Sckuhr, and H. Riesch-Oppermann, "Limitations of the Weibull Theory in Stress Fields with Pronounced Stress Gradients," *Proc. ASME Turbo Expo*, 2000.
- [84] H. Riesch-Oppermann, M. Härtelt, and O. Kraft, "STAU – a review of the Karlsruhe weakest link finite element postprocessor with extensive capabilities," *Int. J. Mater. Res.*, vol. 99, no. 10, pp. 1055–1065, Oct. 2008.
- [85] I. Melikayeva, H. Riesch-Oppermann, V. B. Govorukha, and O. Kraft, "A generalized Weibull approach to interface failure in bi-material ceramic joints," *Arch. Appl. Mech.*, vol. 81, no. 11, pp. 1585–1596, Jan. 2011.
- [86] G. Glinka and G. Shen, "Universal Features of Weight Functions For Cracks in Mode I," vol. 40, no. 6, pp. 1135–1146, 1991.
- [87] G. Shen and G. Glinka, "Determination of weight functions from reference stress intensity factors," *Theor. Appl. Fract. Mech.*, vol. 15, no. 3, pp. 237–245, Aug. 1991.
- [88] H. Kahn, R. Ballarini, J. J. Bellante, and A. H. Heuer, "Fatigue Failure in Polysilicon Not Due to Simple Stress Corrosion Cracking," vol. 298, no. November, pp. 1215–1219, 2002.
- [89] K. Abbas, S. Alaie, and Z. C. Leseman, "Design and characterization of a low temperature gradient and large displacement thermal actuators for in situ mechanical testing of nanoscale materials," *J. Micromechanics Microengineering*, vol. 22, no. 12, p. 125027, 2012.

- [90] J. Sniegowski and M. De Boer, "IC-compatible polysilicon surface micromachining," *Annu. Rev. Mater. Sci.*, no. 1, pp. 299–333, 2000.
- [91] M. P. de Boer, A. D. Corwin, P. G. Kotula, M. S. Baker, J. R. Michael, G. Subhash, and M. J. Shaw, "On-chip laboratory suite for testing of free-standing metal film mechanical properties, Part II – Experiments," *Acta Mater.*, vol. 56, no. 14, pp. 3313–3326, Aug. 2008.
- [92] P. J. Clews and S. S. Mani, "Selective etchant for oxide sacrificial material in semiconductor device fabrication." US Patent #6,893,578, 17-May-2005.
- [93] M. Baker, J. Walraven, T. Headley, and R. Plass, *Final Report: Compliant Thermo-mechanical MEMS Actuators, LDRD# 52553*, no. December. Tech. rep., Sandia National Laboratories, United States. Dept. of Energy, 2004.
- [94] C. Y. Yu, P. L. Sun, P. W. Kao, and C. P. Chang, "Mechanical properties of submicron-grained aluminum," *Scr. Mater.*, vol. 52, no. 5, pp. 359–363, Mar. 2005.
- [95] M. A. Haque and M. T. A. Saif, "Deformation mechanisms in free-standing nanoscale thin films: a quantitative in situ transmission electron microscope study.," *Proc. Natl. Acad. Sci. U. S. A.*, vol. 101, no. 17, pp. 6335–40, Apr. 2004.
- [96] ASTM Standard E112, "Standard Test Methods for Determining Average Grain Size," *ASTM Int.*, vol. 03.01, 2012.
- [97] M. B. Sinclair, M. P. de Boer, and A. D. Corwin, "Long-working-distance incoherent-light interference microscope.," *Appl. Opt.*, vol. 44, no. 36, pp. 7714–7721, 2005.
- [98] L. A. Giannuzzi and F. A. Stevie, "A review of focused ion beam milling techniques for TEM specimen preparation," *Micron*, vol. 30, no. 3, pp. 197–204, Jun. 1999.
- [99] F. A. McClintock and A. S. Argon, *Mechanical behavior of materials*. Addison-Wesley Pub. Co., 1966, p. 770.
- [100] G. Dieter and D. Bacon, "Mechanical Metallurgy," *McGrawHill Shoppenhangers Road Maidenhead Berksh. SL2 2QL UK* 1988, 1988.
- [101] E. Soylemez, R. A. Plass, W. R. Ashurst, and M. P. de Boer, "Probing microelectromechanical systems in an environmentally controlled chamber using long working distance interferometry.," *Rev. Sci. Instrum.*, vol. 84, no. 7, p. 075006, Jul. 2013.
- [102] H. Huang and F. Spaepen, "Tensile testing of free-standing Cu, Ag and Al thin films and Ag/Cu multilayers," *Acta Mater.*, vol. 48, no. 12, pp. 3261–3269, Jul. 2000.
- [103] D. T. Read, Y. Cheng, R. R. Keller, and J. D. Mccolskey, "Tensile properties of free-standing aluminum thin films," *Scr. Mater.*, vol. 45, no. 5, pp. 583–589, 2001.

- [104] M. Hommel and O. Kraft, “Deformation Behavior of Thin Copper Films on Deformable Substrates,” vol. 49, pp. 3935–3947, 2001.
- [105] R. D. Emery and G. L. Povirk, “Tensile behavior of free-standing gold films. Part I. Coarse-grained films,” *Acta Mater.*, vol. 51, no. 7, pp. 2067–2078, Apr. 2003.
- [106] R. D. Emery and G. L. Povirk, “Tensile behavior of free-standing gold films. Part II. Fine-grained films,” *Acta Mater.*, vol. 51, no. 7, pp. 2079–2087, Apr. 2003.
- [107] D. Y. W. Yu and F. Spaepen, “The yield strength of thin copper films on Kapton,” *J. Appl. Phys.*, vol. 95, no. 6, p. 2991, 2004.
- [108] Y. Choi and S. Suresh, “Size effects on the mechanical properties of thin polycrystalline metal films on substrates,” *Acta Mater.*, vol. 50, no. 7, pp. 1881–1893, Apr. 2002.
- [109] G. Dehm and B. Inkson, “Plasticity and interfacial dislocation mechanisms in epitaxial and polycrystalline Al films constrained by substrates,” *Mater. Sci. Technol.*, vol. 18, no. 2, pp. 113–117, 2002.
- [110] P. a. Gruber, J. Böhm, F. Onuseit, A. Wanner, R. Spolenak, and E. Arzt, “Size effects on yield strength and strain hardening for ultra-thin Cu films with and without passivation: A study by synchrotron and bulge test techniques,” *Acta Mater.*, vol. 56, no. 10, pp. 2318–2335, Jun. 2008.
- [111] Y. Xiang and J. J. Vlassak, “Bauschinger and size effects in thin-film plasticity,” *Acta Mater.*, vol. 54, no. 20, pp. 5449–5460, Dec. 2006.
- [112] O. Kraft, M. Hommel, and E. Arzt, “X-ray diffraction as a tool to study the mechanical behaviour of thin films,” *Mater. Sci. Eng. A*, vol. 288, no. 2, pp. 209–216, Sep. 2000.
- [113] T. Li, Z. Y. Huang, Z. C. Xi, S. P. Lacour, S. Wagner, and Z. Suo, “Delocalizing strain in a thin metal film on a polymer substrate,” *Mech. Mater.*, vol. 37, no. 2–3, pp. 261–273, Feb. 2005.
- [114] D. Kiener, W. Grosinger, G. Dehm, and R. Pippan, “A further step towards an understanding of size-dependent crystal plasticity: In situ tension experiments of miniaturized single-crystal copper samples,” *Acta Mater.*, vol. 56, no. 3, pp. 580–592, Feb. 2008.
- [115] H. Bei, S. Shim, G. M. Pharr, and E. P. George, “Effects of pre-strain on the compressive stress–strain response of Mo-alloy single-crystal micropillars,” *Acta Mater.*, vol. 56, no. 17, pp. 4762–4770, Oct. 2008.
- [116] M. D. Uchic, P. A. Shade, and D. M. Dimiduk, “Micro-compression Testing of fcc Metals : a selected overview of experiments and simulations,” no. March, 2009.

- [117] P. Sudharshan Phani, K. E. Johanns, E. P. George, and G. M. Pharr, “A simple stochastic model for yielding in specimens with limited number of dislocations,” *Acta Mater.*, vol. 61, no. 7, pp. 2489–2499, Apr. 2013.
- [118] W. Nix, “Mechanical properties of thin films,” *Metall. Mater. Trans. A*, vol. 20, pp. 2217–2245, 1989.
- [119] L. J. van der Pauw, “A method of measuring the resistivity and Hall coefficient on lamellae of arbitrary shape,” *Philips Tech. Rev.*, vol. 20, pp. 220–224, 1958.
- [120] M. G. Buehler, “Bridge and van der Pauw Sheet Resistors for Characterizing the Line Width of Conducting Layers,” *Journal of The Electrochemical Society*, vol. 125, no. 4, p. 650, 1978.
- [121] J. W. Wittwer, T. Gomm, and L. L. Howell, “Surface micromachined force gauges: uncertainty and reliability,” *J. Micromechanics Microengineering*, vol. 12, no. 1, pp. 13–20, Jan. 2002.
- [122] “SUMMiT V, Five Level Surface Micromachining Technology Design Manual,” *Sandia Natl. Lab.*, 2012.
- [123] R. M. Pocratsky and M. P. de Boer, “Determination of thin film coefficient of thermal expansion and residual strain from freestanding fixed–fixed beams,” *J. Vac. Sci. Technol. B, Nanotechnol. Microelectron. Mater. Process. Meas. Phenom.*, vol. 32, no. 6, p. 062001, Nov. 2014.
- [124] P. M. Duxbury, P. L. Leath, and P. D. Beale, “Breakdown properties,” *Phys. Rev. B*, vol. 36, no. 1, pp. 367–380, 1987.
- [125] C. Manzato, A. Shekhawat, P. K. V. V. Nukala, M. J. Alava, J. P. Sethna, and S. Zapperi, “Fracture Strength of Disordered Media: Universality, Interactions, and Tail Asymptotics,” *Phys. Rev. Lett.*, vol. 108, no. 6, p. 065504, Feb. 2012.
- [126] I. Nurhuda, N. T. K. Lam, E. F. Gad, and I. Calderone, “International Journal of Solids and Structures Estimation of strengths in large annealed glass panels,” *Int. J. Solids Struct.*, vol. 47, no. 18–19, pp. 2591–2599, 2010.
- [127] D. Z. Yankelevsky, “Strength prediction of annealed glass plates – A new model,” *Eng. Struct.*, vol. 79, pp. 244–255, Nov. 2014.
- [128] Z. P. Bazant and S.-D. Pang, “Mechanics-based statistics of failure risk of quasibrittle structures and size effect on safety factors,” *Proc. Natl. Acad. Sci. U. S. A.*, vol. 103, no. 25, pp. 9434–9, Jun. 2006.

- [129] S.-D. Pang, Z. P. Bažant, and J.-L. Le, “Statistics of strength of ceramics: finite weakest-link model and necessity of zero threshold,” *Int. J. Fract.*, vol. 154, no. 1–2, pp. 131–145, Feb. 2009.
- [130] H. Tada, P. C. Paris, and G. R. Irwin, *Stress Analysis of Cracks Handbook*, Third. ASME Press, 2000.